Stony Brook University

Uncertainty Quantification For Physical and Numerical Diffusion Models In Inertial Confinement Fusion Simulations

A Dissertation Presented

by

Verinder S. Rana

to

The Graduate School

In Partial Fulfillment of the

Requirements

for the Degree of

Doctor of Philosophy

in

Applied Mathematics and Statistics

Stony Brook University

December 2016

Stony Brook University

The Graduate School

Verinder S. Rana

We, the dissertation committee for the above candidate for the
Doctor of Philosophy degree, hereby recommend
acceptance of this dissertation.

James Glimm - Dissertation Advisor

Distinguished Professor, Department of Applied Mathematics and Statistics

Xiangmin Jiao - Chairperson of Defense

Associate Professor, Department of Applied Mathematics and Statistics

Roman Samulyak - Member

Professor, Department of Applied Mathematics and Statistics

Predrag Krstic - Outside Member

Professor, Institute for Advanced Computational Science

This dissertation is accepted by the Graduate School.

Charles Taber

ean of the Graduate School

Abstract of the Dissertation

Uncertainty Quantification For Physical and Numerical Diffusion Models In Inertial Confinement Fusion Simulations

by

Verinder S. Rana

Doctor of Philosophy

in

Applied Mathematics and Statistics

Stony Brook University

2016

This thesis concerns simulations of Inertial Confinement Fusion. Inertial confinement is carried out in a large scale facility at National Ignition Facility. The experiments have failed to reproduce design calculations, and so uncertainty quantification of calculations is an important asset. Uncertainties can be classified as aleatoric or epistemic. This thesis is concerned with aleatoric uncertainty quantification. Among the many uncertain aspects that affect the simulations, we have narrowed our study of possible uncertainties. The first source of uncertainty we present is the amount of pre-heating of the fuel done by hot electrons. The second source of uncertainty we consider is the effect of the algorithmic and physical transport diffusion and their effect on the hot spot thermodynamics. Physical transport mechanisms play an important role for the entire duration of the ICF capsule, so modeling them correctly becomes extremely vital. In addition, codes that simulate material mixing introduce numerical (algorithmically) generated transport across the material interfaces. This adds another layer of uncertainty in the solution through the artificially added diffusion. The third source of uncertainty we consider is physical model uncertainty. The fourth source of uncertainty we

focus on a single localized surface perturbation (a divot) which creates a perturbation to the solution that can potentially enter the hot spot to diminish the thermonuclear environment. Jets of ablator material are hypothesized to enter the hot spot and cool the core, contributing to the observed lower reactions than predicted levels.

A plasma transport package, Transport for Inertial Confinement Fusion (TICF) has been implemented into the Radiation Hydrodynamics code FLASH, from the University of Chicago. TICF has thermal, viscous and mass diffusion models that span the entire ICF implosion regime. We introduced a Quantum Molecular Dynamics calibrated thermal conduction model due to Hu for thermal transport. The numerical approximation uncertainties are introduced by the choice of a hydrodynamic solver for a particular flow. Solvers tend to be diffusive at material interfaces and the Front Tracking (FT) algorithm, which is an already available software code in the form of an API, helps to ameliorate such effects. The FT algorithm has also been implemented in FLASH and we use this to study the effect that divots can have on the hot spot properties.

To my family and friends

Table of Contents

Acknowledgments

I want to thank my advisor Professor James Glimm. His advice, encouragement and dedication to science has been very invaluable during my studies. His motivation for research will forever motivate me to strive for the best. I am honored to have been his student and learned a great deal from him.

I also want to thank Professor Roman Samulyak, Professor Xiangmin Jiao and Professor Krstic for being on my dissertation committee. I would like to thank Dr. David Sharp and Dr. Baolian Cheng.

I also want to thank all my fellow group members and colleagues throughout these years who have helped me when I got stuck and provided fresh perspectives on my work. I would like to especially thank Hyunkyung Lim and Jeremy Melvin who I have worked most closely with and learned from.

Lastly, I want to thank my family, whose support has always kept me grounded and who have always been there for me.

Chapter 1

Introduction

1.1 Background

Inertial confinement fusion is an experimental program to enable fusion reactions in capsules that contain Deuterium and Tritium (DT) isotopes. The DT isotopes in the fusion reaction compresses to a point where self-sustainable reactions are generated thereby producing a positive net energy gain [21]. The DT thermonuclear reaction produces a 3.5 MeV alpha particle ${}^4_2\mathrm{He}$ and a 14 MeV neutron:

$$D + T \rightarrow {}^4_2\mathrm{He} + n \tag{1.1}$$

The National Ignition Campaign was the experimental effort to find an optimal ICF design target such that net gain can be achieved [20]. The facility where the ICF experiments are carried out is known as the National Ignition Facility [20]. ICF shots fall within two categories called low-foot and high-foot shots [26]. The most notable difference between the two categories are in the number of shock waves that are used to acquire net gain. Both of the approaches did not produce successful experiments given that the initial conditions, which are the initial as designed manufactured conditions, are optimal for the problem.

In parallel with the experiments, computational scientists are designing numerical meth-

ods and using computationally plausible meshes to match simulations to experiments. Much of the computational work is done using HYDRA [22] which is a Lagrangean based hydrodynamic code, which is from Lawrence Livermore National Laboratory. HYDRA is a full physics capability code for the high energy density physics (HEDP) regime. In spite of being able to have optimal initial conditions, the HYDRA code cannot replicate experiments.

1.2 Motivation

In ICF simulations, the effect of algorithmic and physical transport uncertainties have to be estimated for. The algorithmic uncertainties are associated with truncation errors which occur via the discretization which are used to solve the exact equations. Physical transport uncertainties are the uncertainties in the diffusion models, whose exact values are not available for the HEDP regimes. Then there are uncertainties associated with the physical degradation of the capsule itself. For example, the 'pre-mix' of the ablator material into the hot spot and where its originating from. In this section we briefly provide support for the mentioned cases.

1.2.1 Algorithmic Transport

Eulerian codes are sensitive to the computational mesh especially in regard to artificial diffusion across a material interface. A subproblem for the ICF community is to determine the early time ablative and the late time Rayleigh-Taylor Instability [30] (RTI) bubble growth rate α_b of the mixing zone which is used to compute the bubble penetration $h_b(t)$ from the light to the heavy fluid. It follows the Sharp-Wheeler law [31],

$$h_b(t) = \alpha_b \cdot A \cdot g \cdot t^2 \tag{1.2}$$

Similarly, the penetration of the heavy fluid into the light fluid is known as the spike, given by,

$$h_s(t) = -\alpha_s \cdot A \cdot g \cdot t^2 \tag{1.3}$$

where g is the acceleration and A is the Atwood number given by

$$A = \frac{\rho_2 - \rho_1}{\rho_2 + \rho_1} \tag{1.4}$$

where ρ_i, $i = 1, 2$ represents two fluids of different densities.

The total penetration $h(t)$ in the RTI mixing zone can be defined by

$$h(t) = h_b(t) - h_s(t) \tag{1.5}$$

and we can further define the penetration h_t in terms of a total $\alpha = \alpha_b + \alpha_s$,

$$h(t) = \alpha \cdot A \cdot g \cdot t^2 \tag{1.6}$$

The rate of growth of the mixing zone can then can be computed in the following manner

$$\dot{h} = \frac{dh}{dt} = 2 \cdot \alpha \cdot A \cdot g \cdot t \tag{1.7}$$

The immediate benefits of front tracking are two-fold. Firstly, since there is no mixing of materials at a tracked interface, no non-physical diffusion is introduced. Secondly, as the front has a subgrid resolution, it provides a detail below the actual resolution of the underlying grid, it can perform better at coarser resolutions.

Lim and Iwerks [19], obtain excellent agreement of α with experiment. They show that the experimental and the computational estimates for α span $0.042 < \alpha < 0.07$. This verification and validation study of RT mixing used a compressible hydro code, making the importance of large eddy simulations (LES) a necessity, along with sub grid scaling terms to compensate for the under resolved scales. The Schmidt number of the simulations vary from one to five hundred sixty. They concluded that front tracking is an important algorithm that

has capability to keep sharp and distinct interface between two fluids.

Thanks to the work contributed by Kaman et al [16], the value of α has been shown not to depend on initial conditions, for the Smeeton-Youngs experiment validated and verified with respect to these experiments. Their goal was achieved by recreating initial conditions for the RTI and hypothesizing that possibility of pre existing or hidden long wavelengths which might be embedded in the initial data will effect α. The methodology of recreating initial data from experiment is based on Fourier transforms. They found that the Front Tracking compressible code was able to match the α for several different experiments. In addition to matching simulation α with experiment, they concluded that the possibility of long wavelength present in initial conditions does not impact α by more than $\pm 5\%$.

1.2.2 Physical Transport

Transport processes enhance and impact the hydrodynamical instabilities. We refer to molecular dynamics (MD) calibrated transport models. We include mass, viscous and thermal transport models which will be described in more detail in a later section. The transport package is a comprehensive plasma transport interface that has been included in the FLASH code. The package is available to download from www.ams.sunysb.edu/ticf.

ICF flow is mostly dominated by radiation, thermal and mass diffusion. Viscous diffusion does not have a significant effect on the thermodynamic properties of the hot spot. Physical transport models can potentially influence the modeling of the hydrodynamics instabilities that occur in ICF simulations. Since the ICF regime covers the strongly coupled regime to the weakly coupled regime, the simulations must use an accurate diffusion model that is sensitive to large variations in the deforming thermodynamic conditions.

1.2.3 Degradation Sources

The NIC experimental campaign identified four possible sources that could be responsible for the degradation of the thermonuclear condition during the implosion on the NIF facility

[7]. The sources are:

- Pre heating of the fuel which is done by 'hot' electrons. Laser-plasma instabilities that occur in the holhraum emit electrons that have higher thermal velocities. We study this type of uncertainty in our 1D post-shot simulations.

- The presence of the ablator material into the hot spot. Since simulations are not able to correctly capture the right amount of mix, they pre-add ≈ 1 μg of ablator material into the hot spot. However, it is not entirely certain how the origination of such mixing occurs and what are the potential sources that may cause.

- The capsule support tent which seeds a single large low-mode perturbation on the capsule. Experimental diagnostics using in-flight radiographs have confirmed that the capsule support tent decreases the neutron yield by a factor of two, bringing simulations closer to experiment.

- The large low-mode perturbation effect on the fuel shape due to the asymmetry in the radiation drive also gives a factor of two reduction in the neutron yield, also reducing the discrepancy of simulation to experiment.

1.3 Outline

Chapter 2 presents our simulation model. The simulation methods employ FLASH, which is a University of Chicago HEDP code. We will discuss the Front Tracking API (FTAPI) and our transport package TICF. In addition, we provide present background on the key plasma parameters which are used to determine which plasma regimes which arise within the ICF implosion process.

Chapter 3 presents a 1D post shot simulation of shot N120321. This is study is designed to capture the effect of the 'hot' electrons on the adiabat of the cold shell as the capsule

compresses. To model this effect we add energy to the DT ice region just before the shock crosses this interface.

In chapter 4, we present two simulations related to modeling mix correctly in ICF. They are:

- 1D simulations from the HYDRA code to quantify the dimensionless transport coefficients on the various stages of the simulation. The Schmidt and Prandtl number are determined from the thermal, mass and viscous diffusion models.

- 2D simulations in FLASH with and without front tracking and mass diffusion models to quantify the impact on the various stages of the different instabilities. The Buoyancy-Drag model is used to predict 3D mix from 1D simulations, which is then compared to the 2D simulations and examined for a performance cliff where mix of ablator material into the hot spot can occur.

Chapter 5 presents 1D uncertainty quantification simulation studies. The 1D study varies the thermal and concentration diffusion coefficients by up/down factor of two to capture the range of the thermodynamic variables at the time of maximum neutron production. The simulations begin at the time of the Richtmyer-Meshkov instability [27, 24] and are carried to the time of maximum neutron production (bang time).

In Chapter 6 we carry out 2D perturbed simulations that represent a pure CH divot, which is a localized surface perturbation. The simulations present an uncertainty quantification study as the algorithmic and physical transport models are varied. The divot is initialized at the beginning of the RTI, which is the start of the stagnation phase. Finally, in Chapter 7 we summarize the results we found and discuss possible areas where the work could be extended.

Chapter 2

ICF with FLASH, FrontTracking and TICF

2.1 FLASH Numerical Model

We use FLASH [12], version 4.0 to simulate the ICF pellet. FLASH is a publicly available multiphysics multiscale simulation code that is used to study high energy density physics. It is written in FORTRAN90 with a modular structure. FLASH is designed for large multi-core computers and uses the Message-Passing Interface library for inter-process communication. FLASH is also equipped with a Adaptive Mesh Refinement (AMR) package but we do not take advantage of this feature. Instead we rely on Front Tracking which an adaptive method in the spirit of ALE (arbitrary Lagrangean Eulerian) codes, but not otherwise mesh refining.

2.1.1 Multigroup Radiation Model

The radiative transfer equation represents the conservation of photons. In FLASH, the radiative transfer equation is

$$\frac{1}{c}\frac{\partial I}{\partial t} + \Omega \cdot \nabla I + \rho\kappa I = \eta \tag{2.1}$$

where $I\left(\vec{x},\hat{\Omega},\nu,t\right)$ is the radiation intensity of photon frequency ν at a position $\vec{x}$ traveling along the unit direction $\hat{\Omega}$, c is the speed of light, ρ is the mass density, $\kappa\left(\vec{x},\nu,t\right)$ is the opacity in $\frac{cm^2}{g}$, $\eta\left(\vec{x},\nu,t\right)$ is the emissivity. Rewriting this equation as,

$$\frac{1}{c}\frac{\partial I}{\partial t}+\Omega\cdot\nabla I=\eta-\rho\kappa I \tag{2.2}$$

shows us that the right hand side is the total energy emission. The total energy emission is emission minus absorption. Consider a infinite range of photon frequencies $0<\nu<\infty$. We can partition that range into a finite number of subsets, called photon groups. A group is formed by the photons whose frequencies belong to a certain frequency range. The groups are defined by an upper and lower boundary $\nu_a^g<\nu_b^g$. Group g is the set of photons whose frequencies belong to $\nu_a^g<\nu<\nu_b^g$

Kirchoff's law states that emissivity is equal to absorption. Kirchoff law can be written as

$$\eta\left(\vec{x},\nu,t\right)=\kappa\left(\vec{x},\nu,t\right)\cdot I_s\left(\vec{x},\hat{\Omega},\nu,t\right) \tag{2.3}$$

where I_s is spectral intensity source term. This law only holds when the source term is equal to Plancks function,

$$I_p\left(T,\nu\right)=\frac{2\nu^3}{c^2}\cdot\left(e^{\frac{h\nu}{kT}}-1\right)^{-1} \tag{2.4}$$

We use sixty radiation groups, twenty-five groups from 30 eV to 1 keV, twenty-five groups from 1 kev to 5 kev and ten groups from 10 kev to 50 keV.

2.1.2 Radiation Hydrodynamics Equations

Under these assumptions, the mathematical model describing the evolution are equations of radiation hydrodynamics. FLASH solves a coupled system of hydrodynamic, radiation, and

thermal relaxation equations. The hydrodynamics equations

$$\begin{aligned}
\frac{\partial \rho}{\partial t} + \nabla \cdot (\rho \mathbf{u}) &= 0 \ , \\
\frac{\partial \rho \mathbf{u}}{\partial t} + \nabla \cdot (\rho \mathbf{u}\mathbf{u}) + \nabla P_{tot} &= 0 \ , \\
\frac{\partial \rho e_{tot}}{\partial t} + \nabla \cdot (\rho e_{tot} \mathbf{u} + P_{tot} \mathbf{u}) &= \nabla \cdot q \ , \\
\frac{\partial \rho e_{ion}}{\partial t} + \nabla \cdot (\rho e_{ion} \mathbf{u} + P_{ion} \mathbf{u}) &= \rho \frac{c_{v,ele}}{\tau_{ei}} \left(T_{ion} - T_{ele} \right) \ , \\
\frac{\partial \rho e_{ele}}{\partial t} + \nabla \cdot (\rho e_{ele} \mathbf{u} + P_{ele} \mathbf{u}) &= \rho \frac{c_{v,ele}}{\tau_{ei}} \left(T_{ele} - T_{ion} \right) - \nabla \cdot q_{ele} \ , \\
\frac{\partial \rho e_{rad}}{\partial t} + \nabla \cdot (\rho e_{rad} \mathbf{u} + P_{rad} \mathbf{u}) &= \nabla \cdot q_{rad}
\end{aligned} \tag{2.5}$$

are solved in FLASH, where ρ is the fluid density, u the fluid velocity and $e_{tot} = e_{ion} + e_{ele} + e_{rad} + \frac{1}{2} u \cdot u$ is the total internal energy, the total internal energy, written as the sum of internal energy of the ions, electrons and radiation and the kinetic energy. The total pressure $P_{tot} = P_{ion} + P_{ele} + P_{rad}$ is a sum of ion, electron and radiation pressures, with the cold pressure included in P_{ele}. T_{ele} and T_{ion} represent the electron and ion temperature respectively. The electron specific heat is given by $c_{v,ele}$. q denotes the total heat flux and includes contribution from the electron thermal conduction $q_{ele} = -K_{ele} \nabla T_{ele}$ and the radiation heat conduction $q_{rad} = \sum_{g=1}^{N_g} q_g$ with each energy group g contributing q_g to the total radiation flux. The total heat flux is then $q = q_{rad} + q_{ele}$. K_{ele} is the Lee-More electron thermal conductivity.

2.1.2.1 Riemann Solver

After discretization, we are left with piecewise constant data, separated by discontinuities at the cell boundaries, whose equation of motion is in the form of a differential conservation law. This configuration is known as the Riemann problem. Analytical solutions to the Riemann problem involve characteristic curves and present discontinuities. In classical fluid dynamics, such solutions are obtained by some combination of shock and rarefaction waves; but they can be written down explicitly. This is at the base of the approach used by most

simulation software to solve the Euler equations. This portion of the software is called a Riemann solver.

Split solvers first follow the domain along some coordinate axis, considering a sweep of cells together, which reduces the problem to one dimension. The process is then repeated on for each dimension until the solution is found for each cell. FLASH contains several Riemann solvers, implemented in their hydrodynamics unit. These solvers feature several improvements with respect to the simple procedure sketched above.

An example among all: the Piecewise Parabolic Method (PPM) - that we broadly use in this work - assumes the data to be piecewise constant and approximates them with parabolic functions. So, it is considering more than two cells at the time, and allows the introduction of several additional mechanisms (i.e. slope limiters) that control and eliminate possible unphysical waves. The PPM features second-order accuracy, and it is considered one of the most reliable methods.

2.1.3 Equation Of State

Although the FLASH code is completed with internal EOS solvers for the materials used in the simulation, we use an ideal equation of state with a temperature dependent gamma $\gamma = \gamma(T)$. The overall goal is to set $\gamma(T) = 5/3$ in the hot spot and $\gamma(T) = 7/4$ in the cold fuel with a smooth transition between them. The value of $7/4$ for the cold shell was chosen from calibration to the Sesame EOS [13, 28, 29]). The exact value for $\gamma(T)$ is

$$\begin{aligned} \gamma(T) &= A - B \cdot \mathrm{erf}[C \cdot (T - D)] \\ A &= \frac{7/4 + 5/3}{2} \approx 1.7083 \\ B &= \frac{7/4 - 5/3}{2} \approx 0.0417 \\ C &= 15 \qquad D = 0.5 \end{aligned} \tag{2.6}$$

with T in keV. A and B set the range of $\gamma(T)$ values. C controls the speed of the transition of $\gamma(T)$ and D sets the midpoint of the transition. These parameters were chosen to give agreement with HYDRA and to maintain a γ of approximately 5/3 in any region where the temperature is larger than 1 keV.

2.2 FrontTracking API

Front tracking [6] is a numerical method which actively tracks the movement of surfaces of discontinuity, ensuring that numerical diffusion does not occur across surfaces. It is therefore an ideal method for modeling the mixing of two or more immiscible fluids separated by a contact discontinuity, as occurs in Rayleigh-Taylor instability. With front tracking, our aim is to attain a superior resolution of interfaces between fluids, and maintain this resolution throughout the simulation. This algorithm benefits the solver by minimizing numerical mass diffusion associated with steep concentration or thermal gradients. Results are satisfactory of tracked solutions versus untracked solutions from coarse to ultra fine grids. The numerical smearing is decreased by preventing the fluids from across the interface from interacting numerically and mixing. The front then partitions the fluids according to their distinct physical characteristics.

In the Front Tracking code, the surfaces of discontinuity are represented by a lower dimensional dynamic grid, known as the interface, which separates fluids into two distinct components. In three-dimensional computations, this interface consists of one or more two-dimensional surfaces discretized by triangles. After a problem has been initialized, a typical Front Tracking time step proceeds in the following chronological order :

1. Normal propagation of the interface.

2. Tangential propagation of the interface.

3. Untangling of the interface.

4. Parallel communication of the interface.

5. Construction of the (finite difference) computational grid.

6. Construction of gridline-interface crossings.

7. Dimensionally split sweep of the interior solver.

8. Sweep close-to-interface grid points.

9. Parallel subdomain communication.

10. Output of time step data.

11. Commencement of a new time step or termination of the run.

The propagation of interface points takes place in a dimensionally-split manner, in a local coordinate system defined by the normal direction to the The 1D tracking for our 1D post shot calibrated simulation was enabled using Front Tracking. Previous convergence analysis studies have been done. Appendix A gives 2D passively tracked and untracked RT interface study with FLASH. An in depth study was carried out using the FTAPI to study the hydrodynamic instabilities in ICF[23].

2.3 Transport ICF (TICF)

Molecular transport is a necessary feature of plasma simulation codes. We develop a transport package that has the capability to model the wide range of regimes that occurs in the ICF implosion. The package is written in Python and is easily portable to codes written in other languages. The package is called TICF and is available for download from www.ams.sunysb.edu/TICF. The package consists of thermal, mass and viscous transport models. The thermal transport is based on the model due to Hu[14, 15]. The mass and viscous diffusion models which we use are calibrated using quantum molecular dynamics simulation and will be described in future section.

2.3.1 Quantum Molecular Dynamics (QMD) and Transport Models

Precise multi-material, multi-temperature equation-of-state (EOS) models are needed for ICF simulations. Being in a HEDP regime, the temperatures are expressed in kilo-electronVolt (keV) whereas the pressures are in giga-bars (GB). Plasma transport theory is crucial in determining conductivity, viscosity and diffusivity for such regime. Because experiments to determine such quantities are difficult and the data is sparse, simulations are used. It is a known fact that presently there are no good approximations for such transport coefficients plasmas that fall under the strongly coupled regime [9]. For weakly coupled plasmas, plasma transport theories are well approximated. The most common thermal models for hot, diffusive plasmas are Spitzer [32] or Lee-More [18]. When the plasma is on the boundary of weak and strong, it is in the regime known a warm-dense matter. Liquid metal and warm-dense matter have complicated physical structures and approximating plasma transport coefficients in this regime becomes computationally difficult.

In this thesis we explore thermal, mass and viscous models calibrated using QMD. The choice for such models allows for the flexibility of modeling the entire ICF regime. At the beginning of the experiment, the capsule is cold and very dense, which can be described as a strongly coupled plasma. As the shock waves heat the capsule, the capsule undergoes regime change. During bang time, the capsule is in the weakly coupled regime. QMD theory, under the Born-Oppenheimer approximation, treats the electrons using quantum and classical mechanics, which makes QMD an effective method to predict EOS properties [8]. To make QMD simulations computationally feasible, a density functional theory approach is taken (DFT).

2.3.2 Dimensionless Transport Coefficients

To characterize the ICF flow regime we discuss related dimensionless Schmidt and Prandtl numbers. We have computed the Prandtl and the Schmidt numbers using our TICF package which will be discussed in the next chapter. Since numerical methods can give rise to numerical diffusion in simulations, they have to be controlled. The mixing rate for the Rayleigh-Taylor and Richtmyer-Meshkov instabilities are dependent on the dimensionless transport coefficients and initial conditions. Therefore our goal is to accurately model mix by estimating the true value of the mixing rate.

Mixing between two fluids can result in molecular mixing or stirring. Pure molecular mixing occurs when the constituents are mixed on a molecular scale, where the regime of atomic physics is relevant. Pure stirring occurs with no transport across a separating interface between the constituents, which is then is stretched. In increase in the interfacial area does not imply molecular mix. Atomic and molecular mix between DT-CH would require scales of a few atoms where as typical fluid dynamics simulations have larger scales. Due to the very small and fine scale structure in ICF flows, diffusion is necessary to model on these scales. The Schmidt number, which will be defined in the next section, influences the mixing rate.

Numerically, the Front Tracking API (FTAPI) achieves desirable results for flows with large Schmidt and Prandtl numbers. The algorithm works on a mesh which can provide up to a refined resolution of the momentum equation. Therefore simulations that allow tracking of the interface between fluids are more accurate in determining the mixing growth rate as opposed to untracked simulations. Untracked Eulerian conservative codes give rise to numerical, mass and thermal diffusion during the hyperbolic step. Due to hyperbolic transport, which is associated with a non zero velocity field, the untracked codes compound error in the numerical solutions that are averaged over grid cells.

Many untracked codes require that the equations of momentum, energy, species and continuity be resolved in order to achieve a precise simulation. In order to achieve this goal,

the untracked simulation codes must use an over resolved mesh beyond the point required for the momentum equation to be over resolved. Subgrid models can be used to quantify and control mass and thermal diffusion errors, however, they cannot cure the effects of numerical diffusion since subgrid models only add diffusion. In order to accurately model the atomic scale mixing, the FTAPI is extremely beneficial. The FTAPI reduces numerical diffusion in the species, continuity, and energy equations, even for coarse grids.

2.3.2.1 Schmidt Number

The Schmidt number gives the ratio of kinematic viscosity to mass diffusivity. This ratio is a measure of the relative influences of kinematic viscosity and mass diffusion in a mixing fluid. It is defined as

$$Sc = \frac{\nu}{D} \tag{2.7}$$

where ν is the kinematic viscosity and D is the mass diffusivity. In our ICF application, the Schmidt number is a function of concentration. For pure CH ablator material the Sc is less than 0.3 which suggests that the FTAPI is not useful. For a 10% DT concentration we notice that the Sc number has a peak with a value of 1.2, suggesting a role for Front Tracking.

2.3.2.2 Prandtl Number

The Prandtl number gives the ratio of kinematic viscosity to thermal diffusivity. The Prandtl number in a plasma is dependent on ionization levels, nuclear charge, and temperature. It is defined as

$$Pr = \frac{\nu}{\alpha} \tag{2.8}$$

where ν is the kinematic viscosity and α is the thermal diffusivity. The Prandtl number is also concentration dependent but is not as sensitive as to the Schmidt number. As the concentration of CH increases the value of the $Pr \sim \mathcal{O}(10^{-4})$. This indicates a highly heat diffusive plasma and no benefit from tracking.

2.3.3 Plasma Frequency and Debye Shielding

Consider a quasi neutral plasma with an equal number of electrons, with mass m_e and charge $-e$, and ions, with m_i and charge $+e$. We can treat the ions and electrons as an ideal gas $P_{i,e} \cdot V = n_{i,e} \cdot R \cdot T_{i,e}$ where $T_{i,e}$ is the temperature of the ions or electrons measured in Kelvin. Quasi neutrality requires that $n_i \approx n_e = n$. We can now define the plasma frequency

$$\omega_p = \sqrt{\frac{4 \cdot \pi \cdot n \cdot Z \cdot q_{ele}^2}{m}} \tag{2.9}$$

where n_i, n_e and n are the number density of the ions, electrons and the combination of the two. q_{ele} is the charge of the particle and m is the mass of the particle and Z is the ionization level. In plasma physics, the plasma frequency defines the fundamental time-scale.

The plasma frequency, also called the critical frequency, is the frequency of oscillation that occurs in a plasma disturbed from local electrical neutrality as it relaxes toward equilibrium. For example, in an ICF implosion there are multiple shock waves that drive the dynamics. This will result in a separation of positive and negative charges in the plasma and therefore will give rise to an electrostatic force that will cause the electrons to travel back to the ions. As they move towards equilibrium they will first overshoot which will cause the force to reverse directions, creating a harmonic motion of the electrons about the ions. The motion is about the ions because the electrons are much lighter than the ions. The frequency of this oscillation depends on basic fundamental constants of the electron together with the density of free electrons in the plasma.

The free electrons are suspended in the background and cloud around the ions. The

screening length associated with the 'cloud' from the ion is given by the Debye length defined as [18],

$$\lambda_D = \frac{1}{\sqrt{\left(\frac{4\cdot\pi\cdot q_{ele}^2\cdot n_e}{k_B\cdot\sqrt{T_{ele}^2+T_f^2}}\right)+\frac{\left(4\cdot\pi\cdot n_i\cdot Z^2\cdot q_{ele}^2\right)}{k_B\cdot T_{ion}}}} \tag{2.10}$$

where T_f is the Fermi temperature and k_B is the Boltzmann constant. The ionization level Z governs the charge of the ion which is $Z \cdot q_{ele}$, where q_{ele} is the charge of the electron. The Debye sphere gives an average approximation of the n_{ele} that are in the cloud and is given by

$$N_D = \frac{4}{3} \cdot \pi \cdot n \cdot \lambda_D^3 \tag{2.11}$$

When $N_D >> 1$, the charge screening is well described by classical plasma physics theory. However, in an ICF capsule, the plasma is very complicated as it is switching from ideal to non ideal plasma and vice versa.

2.3.3.1 Yukawa OCP and the Coloumbic OCP

Charge screening plays an important role when the ingredients in an ICF reaction are concentration dependent. We will carry out analysis in a later section that shows this is the case. To incorporate the screening effects into our transport package we investigated the influence of pair potential during different regimes in an ICF implosion.

For the Yukawa one component plasma model description, the interaction for two particles separated by a distance r is

$$v\left(r\right) = \frac{Z^2 \cdot q_{ele}^2 \cdot \exp\frac{-r}{\lambda_s}}{4 \cdot \pi\epsilon_0} \tag{2.12}$$

where ϵ_0 is the electron permitivvity constant and Z is the ionization level. More will be discussed in a future section on Z. The electron screening length λ_s is a modification of the Debye screening length. However, λ_s captures the effect of screening for non ideal plasmas

as λ_D is meant for ideal plasmas. λ_s will be defined below.

The Coloumbic one component plasma is the limit as $\lambda_s \to \infty$. It is defined as

$$v\left(r\right) = \frac{Z^2 \cdot q_{ele}^2}{4 \cdot \pi \epsilon_0} \tag{2.13}$$

This is the case when there is no electron screening effect. Screening is synonymous with shielding and therefore we can describe the shielding effect as follows, the high energy electrons that are penetrating to the nucleus of the atom observe low energy electrons that shields them from the nucleus. As a result, the high energy electrons see a smaller nuclear charge.

In the ICF regime, the plasma starts off as being non ideal and eventually transitioning into a pure OCP. To characterize this transition, we make the use of two parameters Γ and κ. We define κ to be the electronic screening parameter,

$$\kappa = \frac{a}{\lambda_s} = a \cdot \frac{\sqrt{4 \cdot \pi \cdot Z \cdot n_{ion} \cdot q_{ele}^2}}{\sqrt{\left(k_B \cdot T_{ele}\right)^2 + \left(\frac{2}{3} \cdot E_f\right)^2}} \ , \tag{2.14}$$

where T_{ele}, T_{Fermi} are the electron and Fermi temperature and a is the Wigner-Seitz radius

$$a = \left(\frac{3}{4 \cdot \pi \cdot n_{ion}}\right)^{\frac{1}{3}} \tag{2.15}$$

As $\lambda_s \to \infty$, $\kappa \to 0$ and we are in the COCP regime.

Γ is defined as

$$\Gamma = \frac{Z^2 q_{\text{ele}}^2}{a \cdot T_{\text{ion}} \cdot k_B}, \tag{2.16}$$

where T_{ion} is the ion temperature. For $\Gamma \ll 1$, the plasma is weakly coupled, and for $\Gamma \gg 1$, the plasma is strongly coupled. When the plasma is weakly coupled, it is characterized as being hot and diffusive. Otherwise the strongly coupled plasmas are considered to be cold

and dense. Another parameter of interest is the degeneracy parameter, Θ, it is defined as

$$\Theta = \frac{k_B \cdot T_{ele}}{E_f} \ , \tag{2.17}$$

where E_f is the Fermi energy. If $\Theta \approx 1$ and $\Gamma \approx 1$, then the plasma is in a warm dense matter state. The applications of these parameters will be discussed in a future section.

2.3.4 Thermal Conduction

We use three thermal conduction models for a 1D uncertainty quantification study, see Chapter 5. The models are the Lee-More, Hu and Spitzer thermal conductivity models. FLASH offers Lee-More and Spitzer conduction models to use. TICF has the default implementation of the Hu conductivity model, which is calibrated using QMD. The Spitzer conductivity model offered in FLASH is the standard implementation for many hydrodynamics codes, defined as

$$K_{ele} = \left(\frac{8}{\pi}\right)^{\frac{3}{2}} \cdot \frac{k_B^{\frac{7}{2}}}{e^4 \cdot \sqrt{m_{ele}}} \cdot \frac{1}{1 + \frac{3.3}{z}} \cdot \frac{T_{ele}^{\frac{5}{2}}}{z \cdot ln\,(\Lambda)}. \tag{2.18}$$

where $ln\,(\Lambda)$ is the Coulomb logarithm. Thus we will introduce the Lee-More and the Hu conduction models.

2.3.4.1 Lee-More

The Lee-More model computes the thermal conduction K_{ele} as

$$K_{ele} = n_{ele} \cdot k_B \cdot k_B \cdot T_{ele} \cdot \tau \cdot \frac{A_\beta}{m_{ele}}, \tag{2.19}$$

where n_{ele} is the electron number density, k_B is the Boltzmann constant, T_{ele} is the electron temperature, τ is the Lee-More relaxation time and A_β is the Spitzer thermal conduction

limit. More specifically, τ in 2.19 is represented by

$$\tau = max\left(\alpha, \beta\right) \tag{2.20}$$

where α is given by

$$\alpha = \frac{3}{2\sqrt{2.0}\cdot\pi}\cdot k_B^{1.5}\cdot\frac{\sqrt{m_{ele}}}{q_{ele}^4}\cdot\frac{T^{1.5}}{\Lambda\cdot\bar{z}+3.3\cdot n_{ele}}\cdot\left(1+e^{-\mu\cdot\nabla kT}\right)\cdot Fermi_{\frac{1}{2}} \tag{2.21}$$

and β is given by

$$\beta = \frac{\frac{4\cdot\pi\cdot n_{ion}}{3}^{-1/3}}{\sqrt{\frac{3\cdot k_B\cdot T}{m_{ele}}}} \tag{2.22}$$

and $Fermi_{\frac{1}{2}}$ is given by,

$$Fermi_{\frac{1}{2}} = \frac{n_{ele}}{2\cdot\frac{m_{ele}\cdot k_B\cdot T}{2\cdot\pi\cdot\bar{h}^2}^{3/2}} \tag{2.23}$$

2.3.4.2 Hu

The Hu model provides thermal conduction for the DT and CH materials unlike the Spitzer and Lee-More models. The key difference between the Hu, Lee-More and Spitzer model is the computation of Coloumb logarithm which allows conductivity for the DT and CH materials. Here, the K_{ele} for the DT and the CH material is

$$K_{ele} = \frac{20\cdot\left(\frac{2}{\pi}\right)^{1.5}\cdot k_B^{3.5}\cdot T^{2.5}}{\sqrt{m_e}\cdot\bar{z}\cdot q_{ele}^4}\cdot\frac{0.095\cdot\left(\bar{z}+0.24\right)}{1+0.24\cdot\bar{z}}\cdot\frac{1}{ln\Lambda_{QMD}}. \tag{2.24}$$

$ln\Lambda_{QMD}$ is the calibrated Coulomb logarithm and is defined differently for DT and CH. For DT the Coulomb logarithm is

$$ln\Lambda_{QMD} = \exp\left(\alpha_0 + \sum_{i=1}^{5} \alpha_i \cdot (ln\Gamma)^i + \beta_i \cdot (ln\theta)^i\right) \tag{2.25}$$

and for CH it is defined as

$$ln\Lambda_{QMD} = \exp\left(\alpha_0 + \sum_{i=1}^{6} \alpha_i \cdot (ln\Gamma)^i + \beta_i \cdot (ln\theta)^i\right) \tag{2.26}$$

where α_i and β_i are material dependent parameters calibrated using QMD and Γ and Θ are the coupling and degeneracy parameters.

2.3.5 Mass Diffusion

Physical concentration diffusion is sensitive to the variation in the plasma coupling regime. The TICF package includes a physical concentration diffusion model which conforms to the coupling. Within the weakly coupled regime, we use a kinetic theory approach of Chapman-Spitzer which takes into consideration the screening induced by ions [9]. When the plasma is strongly coupled, the diffusion between the constituents is modeled as an extension to the Daligault model [10, 11].

2.3.6 Viscous Diffusion

Viscosity has a secondary role in ICF simulations but not enough to influence the implosion dynamics [1]. Viscosity is also dependent on the plasma regime and thus needs careful consideration for any simulations that do require viscous modeling. Viscosity models themselves are sensitive to the coupling and the degeneracy parameter. Thus the absolute and kinematic viscosity coefficients computed from these models are functions of the thermodynamic variables (ρ, T_{ion}) in the plasma regime of interest.

When the ICF plasma is weakly coupled the degeneracy level becomes important in

applying the correct model. When the plasma is weakly coupled we use:

- $\Gamma < 0.5$ the standard Braginskii [3] viscosity model

and when the plasma is in the warm dense matter regime:

- $\Gamma > 0.5$ and $0 < \Theta < 1$ the Yukawa viscosity [25] model which has been calibrated using QMD [25]. This model has been used in a previous study related to turbulence in ICF [33]

and in the strongly coupled regime we use:

- $\Gamma > 0.5$ and $\Theta > 1$ the Bastea viscosity model [2].

Chapter 3

Post-shot 1D simulation

The first uncertainty we quantify is the effect from the electron preheating [4, 5] on the capsule core. The earlier, initial laser-plasma instabilities give rise to 'hot' electrons. During the acceleration phase, the 'hot' electrons can prematurely reach the core of the capsule thereby preheating the fuel which increases the adiabat and the compressibility. This has direct consequence on the hot spot thermodynamics and the resulting mix. The amount of preheating is certainly not known beforehand and so we vary this parameter which allows us to understand the effects of added energy on the performance of the core.

We conduct a set of 1D simulations which model the configuration of the hot spot and how the effect of preheating can influence the mixing of the fuel and cold shell. We conduct simulations using the HYDRA code and compare the results to the FLASH simulations. Our main result is that the hot spot thermodynamics is very sensitive to the amount of preheating. In addition, the FLASH simulations are in qualitative agreement with the HYDRA simulation and therefore similar conclusions exist for the two simulated results. See Appendix B.

Chapter 4

Length scales for mixing

The underlying physical transport coefficients (and instability initial conditions) are essential inputs to determining the mixing properties of an ICF implosion. The physical transport coefficients are sensitive to mixture composition and thus become dependent on them. In our second uncertainty quantification study we simulate the effects of transport coefficients while varying the species concentration. The ablator material is C_2H_3 and the properties are are used as given in [17] to model the ablator material.

We show the significance of the Schmidt and Prandtl number as a function of concentration. We notice that the flow is dependent on the concentration of the species and can be divided into two characteristic regions depending on the Schmidt number; that is, the Schmidt number of $O(1)$ and $Sc << 1$. At the regime where the Schmidt number is much smaller than unity, mass diffusion proceeds at a faster speed than momentum diffusion, and the mass boundary layer becomes much larger than the momentum boundary layer.

The simulations reveal that the Prandtl number is always negligible over different concentrations and thermal conductivity dominates. The value of the Schmidt number over the different concentrations suggests that atomic mix occurs in the cold shell. We also couple a 1D buoyancy drag mix model for the mixing zone edges in the FLASH code. See Appendix C.

Chapter 5

1D Uncertainty Quantification

This chapter is dedicated to the sensitivity of the ICF flow under various thermal and concentration diffusion models. In ICF, this topic is of importance because the physical transport models influence the hydrodynamics and energy transport. For our third uncertainty quantification study, we conduct an ensemble of 1D simulations which vary three different thermal diffusion models with a single concentration diffusion model.

We evaluate the variation in the physical transport coefficients by a factor of two and observe the effects on the hot spot thermodynamics. The aim is to quantify the effect of the variation on the simulations as opposed to agreeing with shot N120321 values such as the neutron yield or the burn-weighted temperature. The thermodynamics are determined from the underlying models used for inertial fusion simulations and so it is necessary to quantify the sensitivity of these models.

The simulations start at the beginning of the Richtmyer-Meshkov phase which occurs at 14.5 ns. For the sensitivity analysis we only focus on two physical transport models: thermal and mass. To examine the model uncertainty we carry out the following three sets of 1D simulations:

- The first simulation study has two purposes:
  - The first purpose is to study the variation across the thermal diffusion models

of Lee-More, Spitzer and Hu. Each model is then further multiplied or divided by a factor of two to capture the range of possible values of the temperature at bang time. The ion temperature varies by ≈20% in the direction of the variation. Other related thermodynamic variables are mostly unchanged thus there is an insignificant change on the hot spot thermodynamics. See Figs. 5.1, 5.2, 5.3, 5.4 and Table 5.1.

  - The second purpose is to study the effect of the Hu thermal diffusion coefficient while incorporating the concentration diffusion model and not varying the concentration diffusion coefficient. The ion temperature and density follow the trend from the first part of this simulation study as the thermal diffusion coefficient is varied. The carbon concentration is slightly sensitive to the variation in thermal diffusion. See Fig. 5.5.

- In the second set of simulations we fix the thermal conduction model of Hu and only vary the concentration diffusion model of Daligault by a factor of two up/down. There is no change in the hot spot thermodynamics from this variation. Insignificant change in the DT and CH concentrations are observed. See Figs. 5.6 and 5.7.

- For the last set of simulations, we vary the thermal conduction model of Hu and the concentration diffusion model of Daligault in either direction by a factor of two. The trend from the first simulation study follows as the thermal diffusion coefficient is varied. There is a ≈20% effect on the ion temperature but related thermodynamic variables are mostly unchanged. See Figs. 5.8, 5.9 and Tables 5.2, 5.3

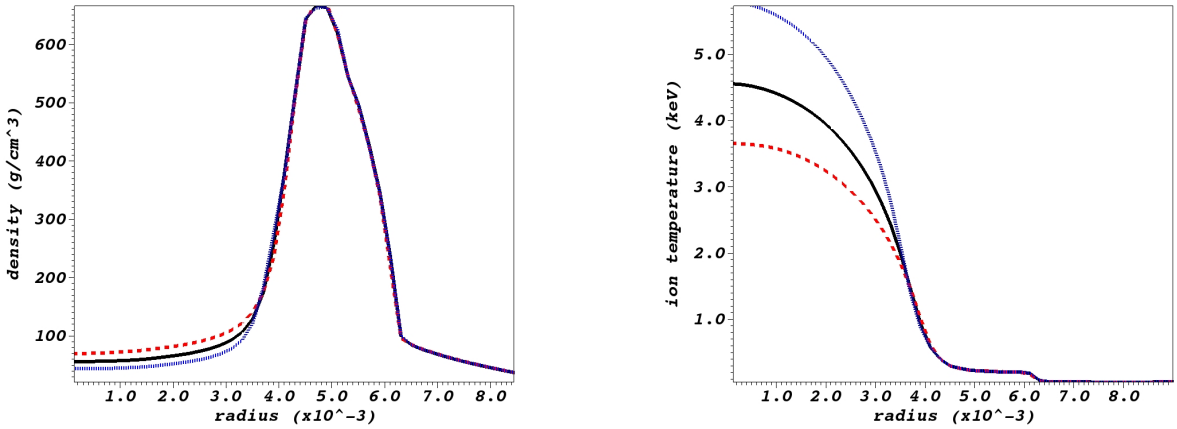

Figure 5.1: Comparison of simulations using the Lee-More thermal conduction at bang time. The black solid line represents the standard simulation with no factor of two. The dashed line represents the thermal diffusion coefficient increased by a factor of two and the blue line represents the decrease by a factor of two. Left: Plot of density. Right: Plot of ion temperature.

5.1 Thermal Diffusion Variation

5.1.1 Thermal with No Concentration

In the right frame of Fig. 5.1 the Lee-More model results in a ≈20% change in the ion temperature in both directions from the factor of two as compared to the standard (numerically determined coefficient) simulation. Similar trends are observed across the Spitzer and Hu models as well which are given in Figs. 5.2 and 5.3.

In Fig. 5.4, the density and temperatures from the Lee-More, Spitzer and Hu thermal conduction models are plotted at bang time. In the left frame, the density remains largely unchanged between the three models. The Hu model gives a slightly different solution at the peak of the cold shell but it is within 3% change with respect to the Lee-More and Spitzer models. The computation of the thermal conductivity in the Hu model is material dependent whereas the thermal conduction in the Lee-More and Spitzer models are computed as a single species for the entire region within the capsule. As a result, the computed Coulomb logarithm and thus the conductivity is slightly more accurate in the Hu model as opposed to the Lee-

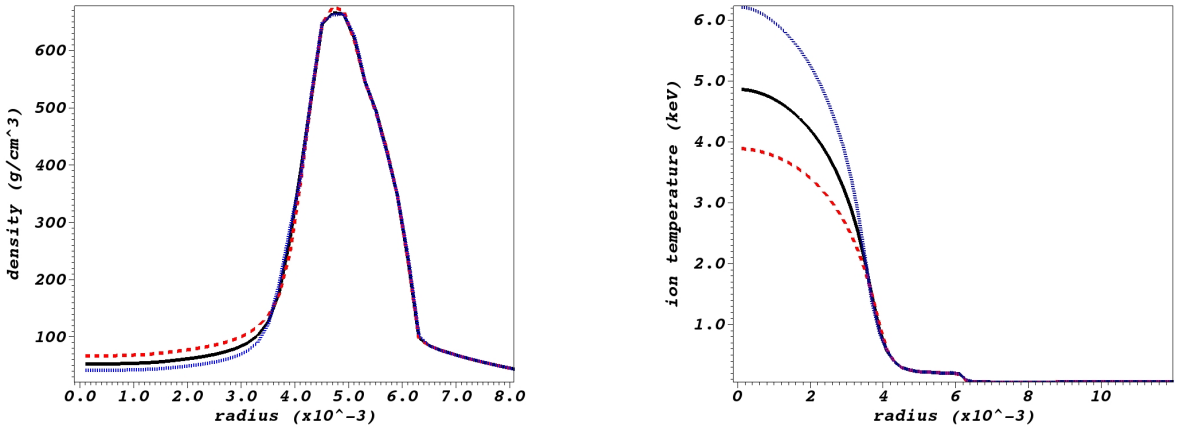

Figure 5.2: Comparison of simulations using the Spitzer thermal conduction at bang time. The black solid line represents the standard simulation with no factor of two . The dashed line represents the thermal diffusion coefficient increased by a factor of two and the blue line represents the decrease by a factor of two. Left: Plot of density. Right: Plot of ion temperature.

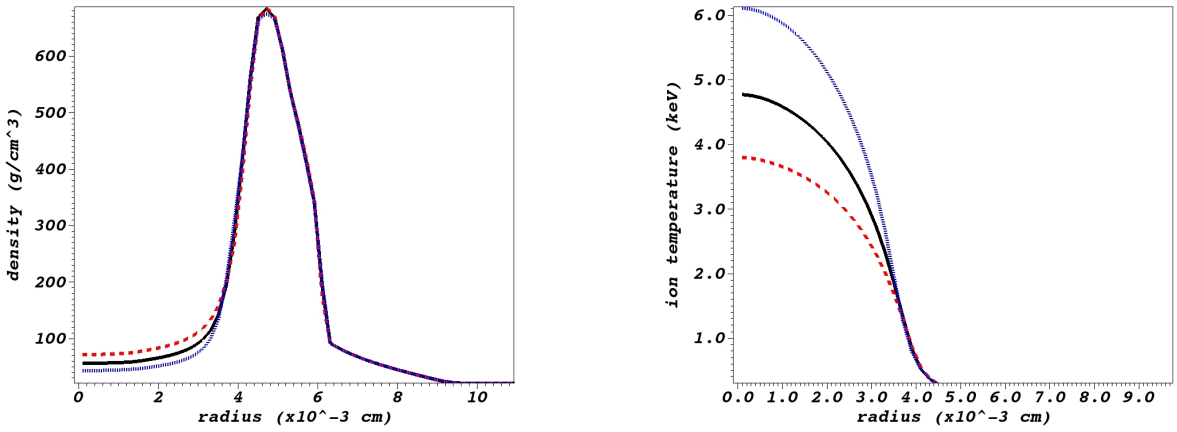

Figure 5.3: Comparison of simulations using the Hu thermal conduction at bang time. The black solid line represents the standard simulation with no factor of two. The dashed line represents the thermal diffusion coefficient increased by a factor of two and the blue line represents the decrease by a factor of two. Left: Plot of density. Right: Plot of ion temperature.

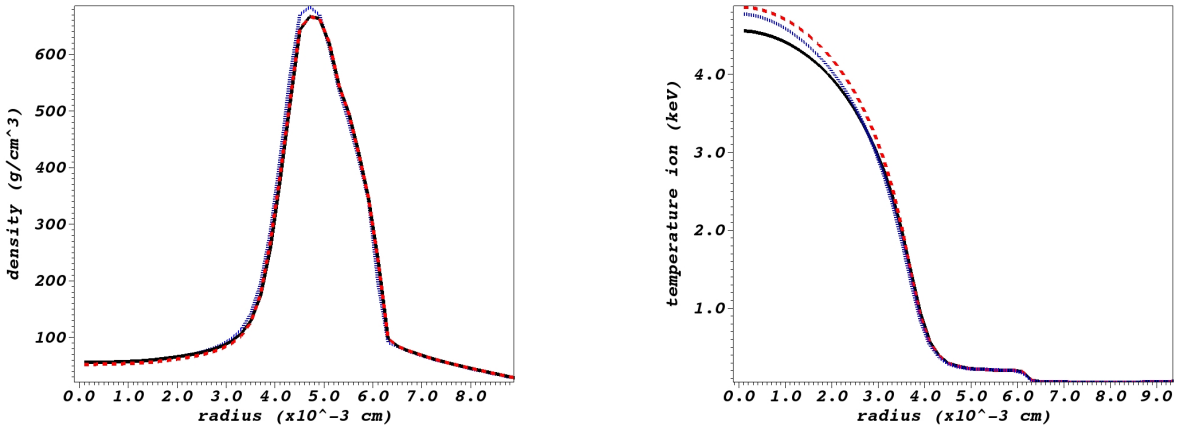

Figure 5.4: One way comparison of simulations varying the thermal conduction shown at bang time. The black solid line represents the Lee-More thermal conduction model. The red dashed line represents the Spitzer thermal diffusion coefficient and the blue line represents the Hu thermal conduction model. Left: Plot of density. Right: Plot of ion temperature.

More and Spitzer models. However, the Lee-More and Spitzer models both provide a very good approximation in the region of interest.

The increase/decrease factor of two in the thermal conductivity coefficients bands the ion temperature in the range from 4 keV to 6 keV at bang time across the three thermal models. The density does not have a broad interval as the ion temperature does. Table 5.1 summarizes the inertial confinement fusion diagnostic variables across the three models. The variables in Table 5.1 have good agreement amongst the thermal models but have no agreement with the experiment (shot N120321) as these are 1D simulations and additional effects such as 2D, 3D, radiation asymmetries and other potential factors are not taken into consideration here.

5.1.2 Thermal with Fixed Concentration

We then fix the Daligault diffusion model and vary the Hu thermal model by a factor of two. In this comparison, we observe the effects of a thermal diffusion model included with concentration diffusion. Fig. 5.5 shows the effect on the species concentration, the ion temperature

Table 5.1: Comparison of inertial confinement fusion diagnostic variables across thermal conduction models and shot N120321.

	Hu	Lee-More	Spitzer	N120321
Yield	7.77633×10^{15}	7.51786×10^{15}	8.25317×10^{15}	$4.1 \pm \times 10^{14}$
Burn Weighted Temperature	3.53 keV	3.41 keV	3.62 keV	2.7±0.2 keV
Areal Density	$0.92 \frac{g}{cm^2}$	$0.9 \frac{g}{cm^2}$	$0.89 \frac{g}{cm^2}$	$1.25 \frac{g}{cm^2}$
Down Scatter Ratio	4.39%	4.28%	4.25%	6.0±0.5%

and density as the thermal diffusivity is varied by a factor of two. There is a change in the ion temperature, density and the material concentration from the variation in the thermal conduction coefficient. From this set of simulations we conclude the variation in the thermal conduction coefficient included with the effect of physical concentration slightly influences the ion temperature, as well as the species concentration. The hot spot thermodynamics are nearly unchanged with or without the addition of the concentration diffusion model.

5.2 Concentration Diffusion Variation

Figs. 5.6 and 5.7 show the effect of the factor of two on the DT and ablator species concentration variables. The concentrations are slightly sensitive to the factor of two. In Fig. 5.6 the deuterium (left frame) and tritium (right frame) are slightly insensitive to the variation in the concentration diffusion coefficient where the variation is less than 1% which makes sensitivity to the coefficient variation insignificant. From the bottom left frame of Fig. 5.7 we conclude that the carbon concentration is nearly unchanged at bang time and is nearly insensitive to the variation in the concentration diffusion. The DT/CH boundary in the same frame is located at ≈40 μm and is also nearly insensitive to the variation in the concentration diffusion coefficient.

We conclude that the variation in the concentration diffusion coefficient has only marginal to effects on the species concentration. Deuterium and tritium show response to the in-

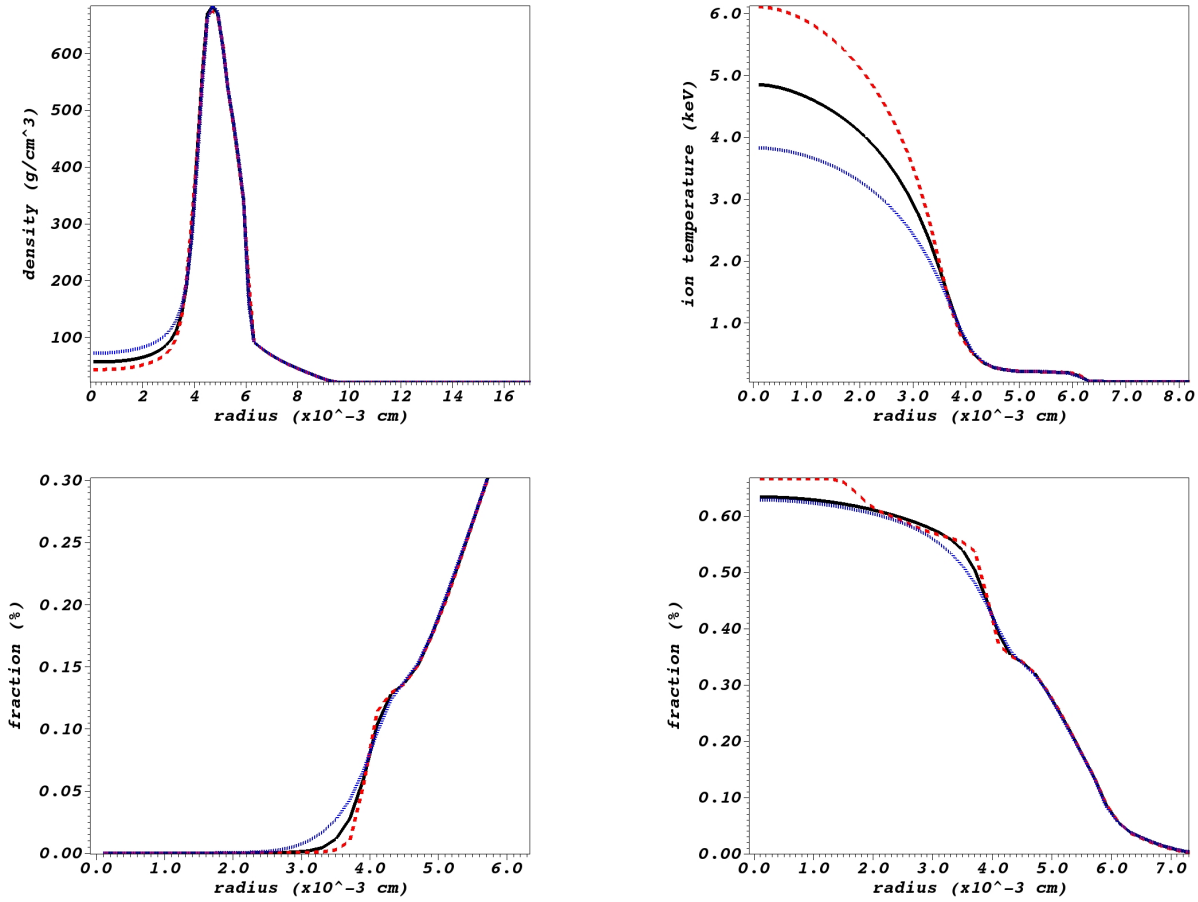

Figure 5.5: One way comparison of simulations varying the thermal conduction shown at bang time. The red dashed solid line represents the simulation with the Hu thermal diffusion coefficient divided by two, the blue line represents the thermal diffusion coefficient multiplied by two and black solid line represents the simulation with the standard thermal diffusion coefficient. All simulations include concentration diffusion. Top left: Plot of density. Top right: Plot of ion temperature. Bottom left: Plot of carbon. Bottom right: Plot of deuterium.

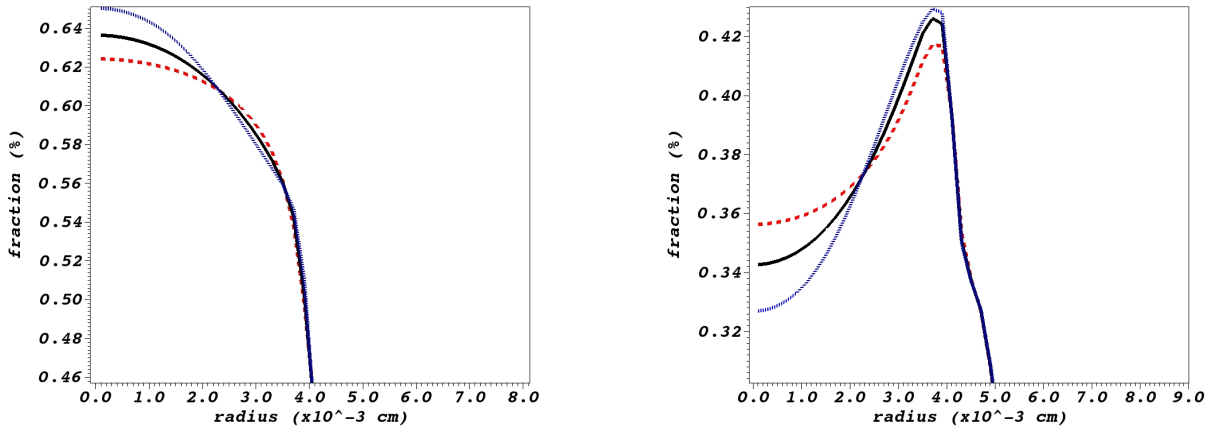

Figure 5.6: One way comparison of the deuterium and tritium concentration while varying the concentration diffusion coefficient shown at bang time. The black solid line represents the standard unmodified simulation. The blue line represents the Daligault concentration diffusion coefficient divided by a factor of two and the red line represents the concentration diffusion coefficient multiplied by two. Left: Plot of deuterium. Right: Plot of tritium.

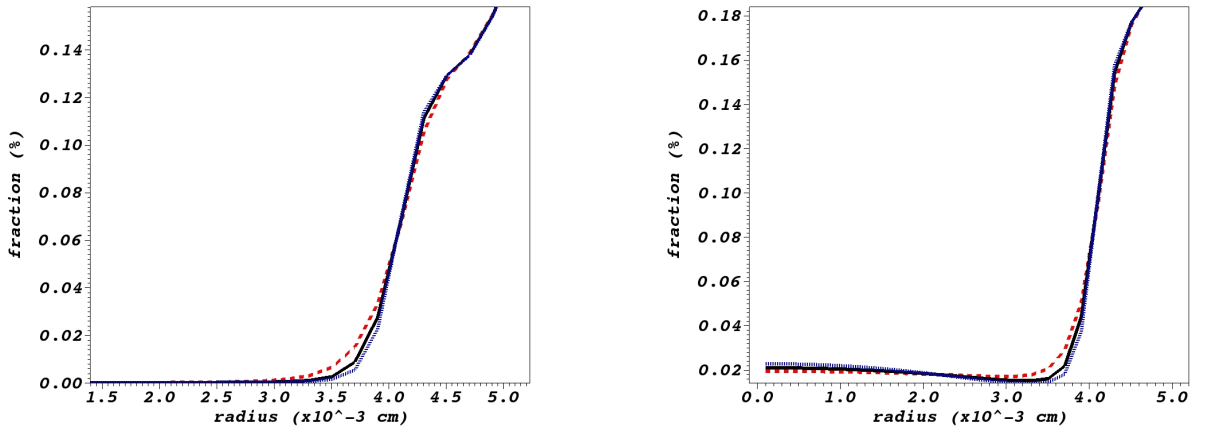

Figure 5.7: One way comparison of the carbon and hydrogen concentration while varying the concentration diffusion coefficient shown at bang time. The black solid line represents the standard unmodified simulation. The blue line represents the Daligault concentration diffusion coefficient divided by a factor of two and the red line represents the concentration diffusion coefficient multiplied by two. Left: Plot of carbon concentration. Right: Plot of hydrogen concentration.

crease/decrease whereas the carbon and hydrogen concentrations show limited response. Thermodynamic variables are strongly influenced by the thermal diffusion coefficient and thus no change is observed in them while varying the concentration diffusion coefficient.

5.3 Thermal and Concentration Diffusion Variation

In Fig. 5.8 we plot the density, ion temperature, carbon and deuterium concentrations at bang time. The thermal coefficient is divided by two and we vary the concentration coefficient up/down by a factor of two. There is a slight change in the deuterium concentration as shown in the bottom right frame but the change is within 1%. The ion temperature and the densities are following the same trends from the first set of calculations effectively showing that only the ion temperature is critically sensitive to the change in the thermal coefficient and not the density.

Table 5.2 shows a summary of the effects of the combined variation in the concentration and thermal diffusion coefficients on the hot spot diagnostics. An increase in the thermal coefficient by a factor of two has resulted in larger neutron yield as compared to the base case. In addition, ion temperature has moved away in the opposite direction from the experimental value. From the table, it is noticeable that the variation in the concentration coefficient results in nearly unchanged diagnostic values. The main driver for the change is the change in the thermal coefficient.

In Fig. 5.9 we vary the concentration diffusion coefficient up/down by a factor of two and hold the Hu thermal diffusion coefficient fixed by multiplying it by a factor of two. The same trend exists in these sets of simulation study as well. There is a slight change in the concentration of the carbon and deuterium whereas the ion temperature sees most of the influence from the thermal coefficient variation.

Table 5.3 shows again a summary of the effects of the combined variation in the concentration and thermal diffusion coefficients on the hot spot diagnostics. This time a decrease

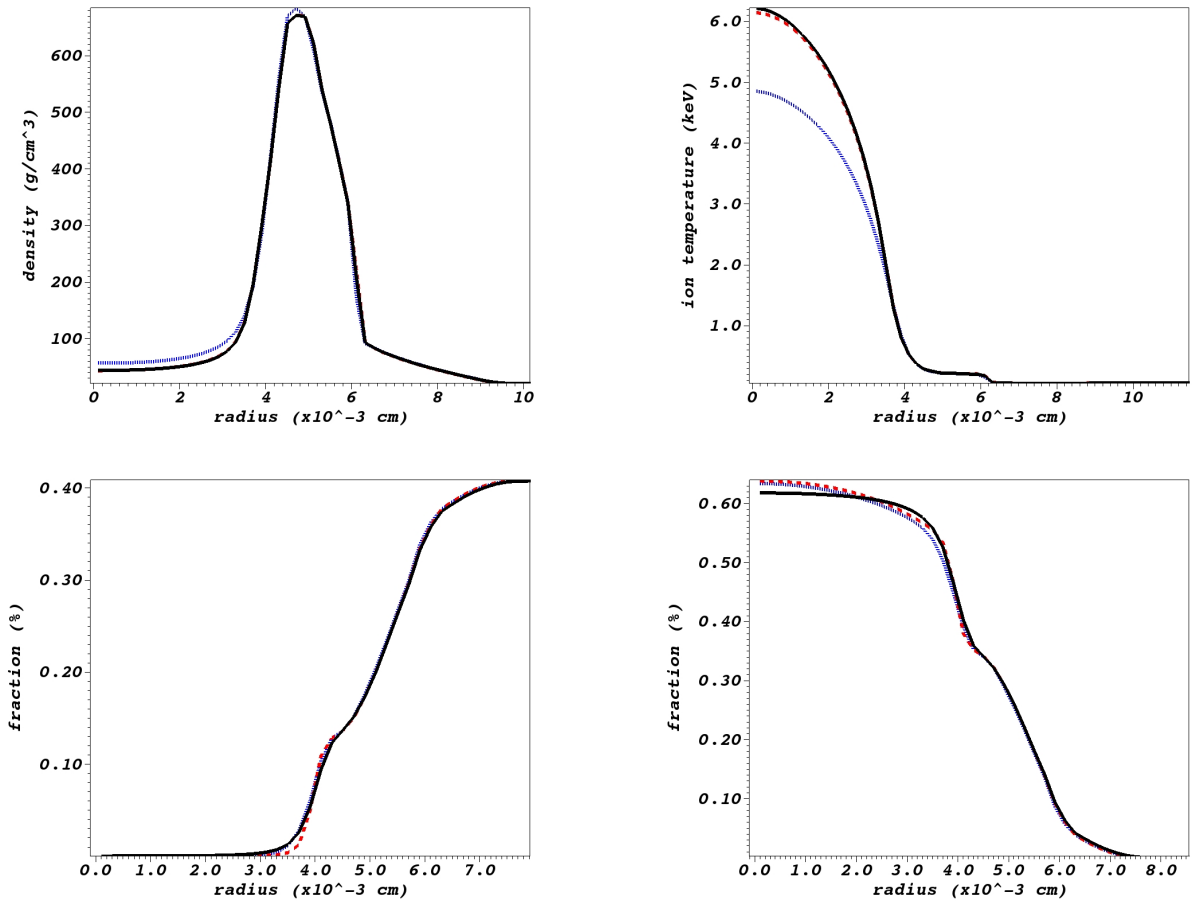

Figure 5.8: Comparisons of the density, ion temperature, carbon and deuterium concentrations while varying the concentration diffusion coefficient up/down by a factor of two and keeping the Hu thermal coefficient fixed by dividing it by two, shown at bang time. The black line represents the simulation with the concentration diffusion coefficient multiplied by two, the red dashed line represents the simulation with the concentration diffusion coefficient divided by a factor of two and the blue dotted line is the standard simulation with no variation. Top left: Plot of density. Top right: Plot of ion temperature. Bottom left: Plot of carbon. Bottom right: Plot of deuterium.

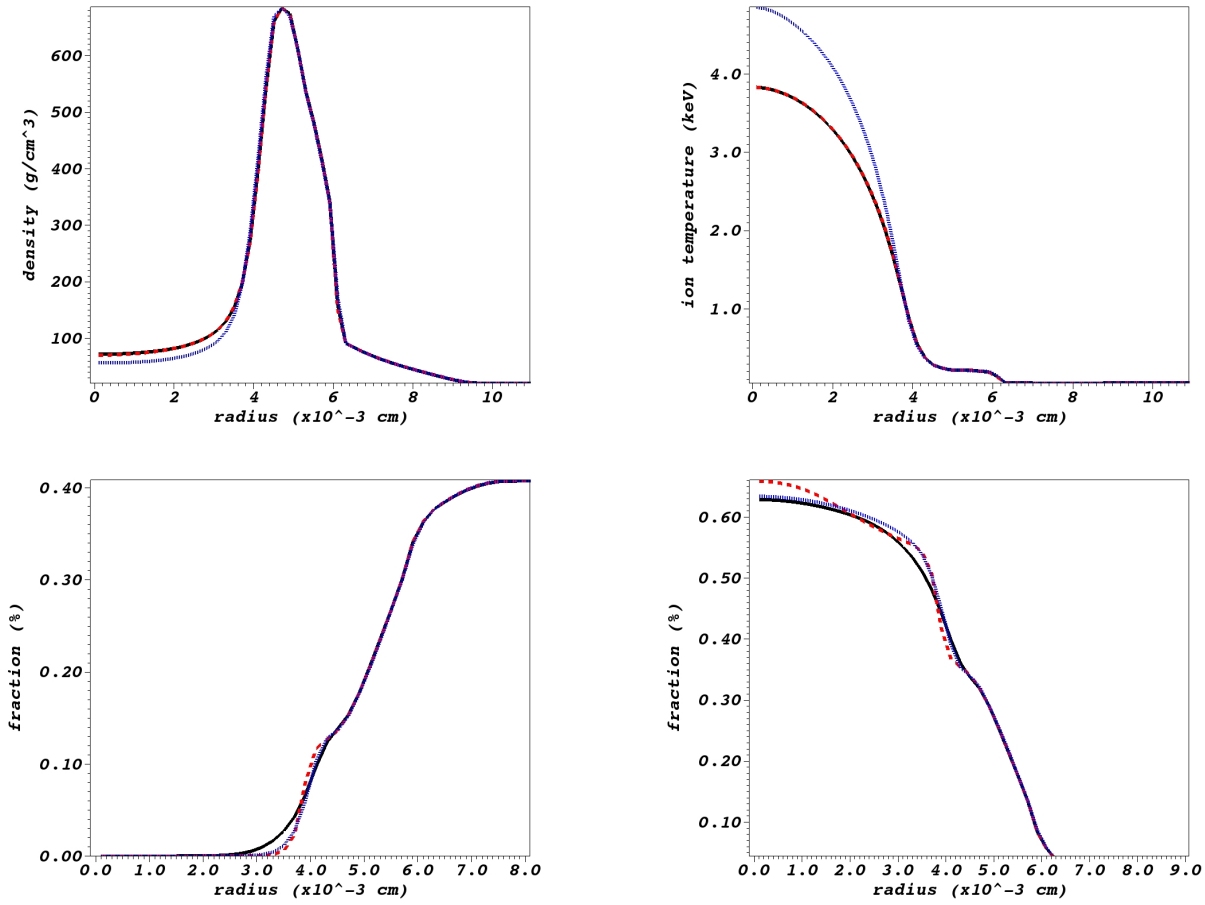

Figure 5.9: Comparisons of the density, ion temperature, carbon and deuterium concentrations while varying the concentration diffusion coefficient up/down by a factor of two and keeping the Hu thermal coefficient fixed by multiplying it by a factor of two, shown at bang time. The black solid line represents the simulation with the concentration diffusion coefficient divided by two while the red dashed line represents the simulation with the concentration diffusion coefficient multiplied by a factor of two and the blue dotted line is the base simulation with no modification to the thermal or concentration diffusion coefficients. Top left: Plot of density. Top right: Plot of ion temperature. Bottom left: Plot of carbon. Bottom right: Plot of deuterium.

Table 5.2: Comparison of inertial confinement fusion diagnostic variables. Base simulation is Hu thermal model with Daligault concentration model and no variation to either coefficient. The next two columns show the variation in the concentration diffusion model and both have the thermal diffusion coefficient divided by two.

	Base	Concentration × 2	Concentration % 2	N120321
Yield	7.77396×10^{15}	1.04753×10^{16}	1.05746×10^{16}	$4.1 \pm \times 10^{14}$
Burn Weighted Temperature	3.58 keV	4.54 keV	4.48 keV	2.7±0.2 keV
Areal Density	0.92 $\frac{g}{cm^2}$	0.87 $\frac{g}{cm^2}$	0.88 $\frac{g}{cm^2}$	1.25 $\frac{g}{cm^2}$
Down Scatter Ratio	4.39%	4.16%	4.17%	6.0±0.5%

Table 5.3: Comparison of inertial confinement fusion diagnostic variables. Base simulation is Hu thermal model with Daligault concentration model and no variation to either coefficient. The next two columns show the variation in the concentration diffusion model and both have the thermal diffusion coefficient multiplied by two.

	Base	Concentration × 2	Concentration % 2	N120321
Yield	7.77396×10^{15}	5.44959×10^{15}	5.55773×10^{15}	$4.1 \pm \times 10^{14}$
Burn Weighted Temperature	3.58 keV	2.92 keV	2.88 keV	2.7±0.2 keV
Areal Density	0.92 $\frac{g}{cm^2}$	0.95 $\frac{g}{cm^2}$	0.95 $\frac{g}{cm^2}$	1.25 $\frac{g}{cm^2}$
Down Scatter Ratio	4.39%	4.5%	4.53%	6.0±0.5%

in the thermal coefficient by a factor of two has resulted in a relatively smaller neutron yield as compared to the base case. In addition, the ion temperature has moved closer towards the direction to the experimental value. From the table, we observe that the decrease by a factor of two in the thermal diffusion coefficient along with the variation in the concentration diffusion coefficient results in near agreement with the experimental ion temperature. As compared with the Hu column in Table 5.1, the variation in the concentration diffusion and thermal diffusion resulted in reducing the discrepancy between the 1D simulation and the experimental ion temperature.

Chapter 6

Perturbed 2D simulation

One of the degradation sources, specifically divots, are formed from isolated defects in the outer capsule surface, which then feed through to the inner DT/CH boundary and then ultimately into the DT fuel. In our last uncertainty quantification study we simulate the isolated perturbation placed at the north pole in our 2D simulation, which is actually a 3D perturbation, only restricted to being rotationally symmetric. Thus, we choose to study axially symmetric 2D simulations in a spherical geometry, which allows us to explore the impacts of Front Tracking while exploring a variety of parameters and mesh levels. Our simulations for this study range from 0 to 0.6 radians in theta coordinates

The simulation begins at a time equivalent to 22.56 ns in the experiment, which is after the shocks have passed through the perturbed interface where we seed the initial perturbation. In our simulations, we model the single effect of the divot and do not include specific capsule features such as the tent and fill tube which have been included in certain ICF simulations. While this approach certainly leads to improved modeling of a specific shot for comparisons of diagnostics, it is not necessary for the analysis carried out here. We are not focused on obtaining agreement with the experiment, but instead in better understanding how the addition of effects such as front tracking interact with the mixing in simulations that do not include these effects. See Appendix D.

Chapter 7

Conclusions

In this dissertation we carried out multiple uncertainty quantification studies and its resulting effect on the ICF implosion process. To accomplish this we used the University of Chicago code FLASH along with front tracking algorithm available for use as an API (http://fti.ams.stonybrook.edu/FTAPI.html) and the TICF package. With the addition of TICF and FTI, we were able to compare tracked/untracked simulations with and without physical transport models in 1D radial and 2D spherical geometries.

ICF requires extremely careful modeling due to the length and time scales involved for the flow and the solution is very sensitive to the underlying physics. We found that front tracking is beneficial for ICF simulations because of its ability to reduce numerical diffusion in regions of sharp concentration gradients. We also note that transport models are important in capturing the characteristics of the ICF flow. Simulations which include effects of front tracking and physical transport models can provide an entire picture of the implosion process from start to end. It has been shown in this thesis that combined effects of numerical and physical diffusion models may play a significant role in the fusion dynamics. In particular, it was shown that the solution depends strongly on the numerical and thermal diffusion models.

We summarize our main conclusions for the uncertainty quantification study as follows:

- The hot spot thermodynamics are sensitive to electron preheating. It becomes important to equip hydrodynamic codes to account for this effect.

- Numerical and physical transport models are important in modeling the physics correctly. Transport models are sensitive to the underlying species concentration in ICF capsules.

- Thermal transport is the most significant form of diffusion process which effects the hot spot thermodynamics. Concentration diffusion does not influence the thermodynamics.

- Divots do not enter the hot spot if modeled as single localized perturbation. A more integrated simulation with combined degradation sources, more precise physics models and high resolution simulations are needed to determine the origin of the CH in the hot spot.

Bibliography

[1] Stefano Atzeni and Jrgen Meyer-Ten-Vehn. *The physics of inertial fusion : beam plasma interaction, hydrodynamics, hot dense matter*. International series of monographs on physics. Oxford University Press, Oxford, 2009. Publi initialement chez Clarendon press en 2004.

[2] S. Bastea. *Phys Rev E*, page 056405, 2005.

[3] S.I. Braginskii. Transport Processes in a Plasma. *Reviews of Plasma Physics*, 1:205, 1965.

[4] B. Cheng, T. Kwan amd Y.-M. Wang, and S. Batha. Scaling laws for ignition at National Ignition Facility from first principles. *Phys. Rev. E*, 88:041101, 2013. Los Alamos National Laboratory Preprint LA-UR-13-22638.

[5] B. Cheng, T. J. T. Kwan, Y. M. Wang, F. E. Merrill, C. J. Cerjan, and S. H. Batha. Analysis of nif experiments with the minimal energy implosion model. *Physics of Plasmas*, 22(8), 2015.

[6] I.-L. Chern, J. Glimm, O. McBryan, B. Plohr, and S. Yaniv. Front tracking for gas dynamics. *Journal of Computational Physics*, 62:83–110, January 1986.

[7] D. S. Clark, M. M. Marinak, C. R. Weber, D. C. Eder, S. W. Haan, B. A. Hammel, D. E. Hinkel, O. S. Jones, J. L. Milovich, P. K. Patel, H. F. Robey, J. D. Salmonson, S. M. Sepke, and C. A. Thomas. Radiation hydrodynamics modeling of the highest

compression inertial confinement fusion ignition experiment from the national ignition campaign. *Physics of Plasmas*, 22(2), 2015.

[8] L. Collins, I. Kwon, J. Kress, N. Troullier, and D. Lynch. Quantum molecular dynamics simulations of hot, dense hydrogen. *Phys. Rev. E*, 52:6202–6219, Dec 1995.

[9] Jérôme Daligault. Liquid-state properties of a one-component plasma. *Phys. Rev. Lett.*, 96:065003, 2006.

[10] Jérôme Daligault. Diffusion in ionic mixtures across coupling regimes. *Phys. Rev. Lett.*, page 225004, May 2012.

[11] Jérôme Daligault. Practical model for the self-diffusion coefficient in yukawa one-component plasmas. *Phys. Rev. E*, page 047401, Oct 2012.

[12] B. Fryxell, K. Olson, P. Ricker, F. X. Timmes, M. Zingale, D. Q. Lamb, P. MacNeice, R. Rosner, J. W. Truran, and H. Tufo. FLASH: An Adaptive Mesh Hydrodynamics Code for Modeling Astrophysical Thermonuclear Flashes. *apjs*, 131:273–334, November 2000.

[13] M. C. Herrmann, M. Tabak, and J. D. Lindl. *Nucl. Fusion*, 41:99, 2001.

[14] S. X. Hu, L. A. Collins, T. R. Boehly, J. D. Kress, V. N. Goncharov, and S. Skupsky. First-principles thermal conductivity of warm-dense deuterium plasmas for inertial confinement fusion applications. *Phys. Rev. E*, 89:043105, Apr 2014.

[15] S. X. Hu, L. A. Collins, V. N. Goncharov, J. D. Kress, R. L. McCrory, and S. Skupsky. First-principles investigations on ionization and thermal conductivity of polystyrene for inertial confinement fusion applications. *Physics of Plasmas*, 2016.

[16] T. Kaman, J. Glimm, and D. H. Sharp. Uncertainty Quantification for Turbulent Mixing Simulations. In N. V. Pogorelov, E. Audit, and G. P. Zank, editors, *5th International*

Conference of Numerical Modeling of Space Plasma Flows (ASTRONUM 2010), volume 444 of *Astronomical Society of the Pacific Conference Series*, page 21, October 2011.

[17] Flavien Lambert and Vanina Recoules. Plastic ablator and hydrodynamic instabilities: A first-principles set of microscopic coefficients. *Phys. Rev. E*, 86:026405, Aug 2012.

[18] Y. T. Lee and R. M. More. An electron conductivity model for dense plasmas. *Physics of Fluids*, 27:1273–1286, May 1984.

[19] Hyunkyung Lim, Justin Iwerks, James Glimm, and David H. Sharp. Nonideal rayleigh-taylor mixing. 107(29):12786–12792, 2010.

[20] John Lindl, Otto Landen, John Edwards, Ed Moses, and NIC Team. Review of the national ignition campaign 2009-2012. *Physics of Plasmas*, 21(2), 2014.

[21] John D. Lindl, Peter Amendt, Richard L. Berger, S. Gail Glendinning, Siegfried H. Glenzer, Steven W. Haan, Robert L. Kauffman, Otto L. Landen, and Laurence J. Suter. The physics basis for ignition using indirect-drive targets on the national ignition facility. *Physics of Plasmas (1994-present)*, 11(2):339–491, 2004.

[22] M. M. Marinak, G. D. Kerbel, N. A. Gentile, O. Jones, D. Munro, S. Pollaine, T. R. Dittrich, and S. W. Haan. Three-dimensional hydra simulations of national ignition facility targets. *Physics of Plasmas*, 8(5), 2001.

[23] Jeremy Melvin. *Numerical Modeling of Hydrodynamic Instabilities and their Impact on Mix in Inertial Confinement Fusion*. PhD thesis, Stony Brook University, 2016.

[24] E.E. Meshkov. Instability of the interface of two gases accelerated by a shock wave. *Fluid Dynamics*, 4(5):101–104, 1969.

[25] Michael S. Murillo. Viscosity estimates of liquid metals and warm dense matter using the yukawa reference system. *High Energy Density Physics*, 4(1? @ S2):49 – 57, 2008.

[26] H.-S. Park, O. A. Hurricane, D. A. Callahan, D. T. Casey, E. L. Dewald, T. R. Dittrich, T. Döppner, D. E. Hinkel, L. F. Berzak Hopkins, S. Le Pape, T. Ma, P. K. Patel, B. A. Remington, H. F. Robey, J. D. Salmonson, and J. L. Kline. High-adiabat high-foot inertial confinement fusion implosion experiments on the national ignition facility. *Phys. Rev. Lett.*, 112:055001, Feb 2014.

[27] Robert D. Richtmyer. Taylor instability in shock acceleration of compressible fluids. *Communications on Pure and Applied Mathematics*, 13(2):297–319, 1960.

[28] Y. Saillard. In *Proceedings of Inertial Fusion Sciences and Applications 2001*, pages 192–196, Paris, 2002. Elsevier.

[29] J. Sanz, J. Garrier, C. Cherfils, B. Canaud, L Masse, and M. Temporal. Self-consistent analysis of the hot spot dynamics for inertial confinement fusion capsules. *Phys of Plasmas*, 12:112702–1–112702–11, 2005.

[30] D. H. Sharp. An overview of Rayleigh-Taylor instability. *Physica D*, 12:3–18, 1984.

[31] D.H. Sharp and J.A. Wheeler. Late stage of rayleigh-taylor instability. *Institute for Defense Analyses*, 1961.

[32] Lyman Spitzer. *Physics of Fully Ionized Gases*. Interscience, New York, second edition, 1962.

[33] C. R. Weber, D. S. Clark, D. Cook, L. E. Busby, and H. F. Robey. Inhibition of turbulence in inertial-confinement-fusion hotspots by viscous dissipation. *Phys Rev E*, 89:053106–1–053106–5, 2014.

Appendices

Appendix A

Passive Tracking Rayleigh-Taylor Convergence [AMS Internal]

Front Tracking API: Verification And Application to FLASH

Verinder Rana, James Glimm, Ryan Kaufmann

August 22, 2013

Abstract

This paper presents a verification (code comparison) study for a Front Tracking API coupled to FLASH. The API enables passive tracking, and tracks discontinuity curves (2D) or surfaces (3D) in a passive passive scalar, i.e., a scalar quantity whose dynamics is determined by the underlying fluid velocities, but which has no influence on the FLASH simulation itself. The verification study is based on a Rayleigh-Taylor (RT) instability problem, computed using FLASH. To this calculation, we add a passive scalar, initialized at the RT interface, and advected using FLASH velocities. The passive scalar front dynamic is implemented both with and without the API tracking addition.

We show that the passive scalar field, computed with or without tracking, converges to a common fine grid solution for a limited time. For an extended time period, the two solutions both converge under mesh refinement, but to distinct solutions. The reasons for this solution non uniqueness are understood and explained in the text. We compare convergence properties only for a period in which the two limit solutions coincide. The reason for this choice of time limits is achieve solutions in qualitative agreement with experiment.

1 Introduction

1.1 FronTier

We introduce passive tracking to the hydrodynamics solver FLASH. A non-reacting chemical tracer element is a typical passive scalar. A passive front is a jump discontinuity in a passive scalar concentration field. Passive tracking is a front tracking algorithm for the computation of a passive front. The front thus moves with the speed of the fluids. This definition is to be contrasted with active tracking, which describes a interface defined by a fluid discontinuity surface, or front, in a fluid variable which is coupled to and influences the fluid flow. In the context of fluid dynamics, a contact discontinuity can be represented as an interface that separates two physically different fluids. The front is active or

passive according to whether the fluids have distinct properties which influence the dynamics of the fluid.

The front tracking method is advantageous for very complex, evolving dynamical interfaces. A careful treatment of the interface is required to ensure accurate modeling of the discontinuity in such cases. The front tracking method is implemented in the FronTier library. A fourth order Runge-Kutta solver is used to propagate the front points using a velocity field derived from the FLASH simulation.

We assume an inviscid, compressible fluid with a gamma law EOS. The equations for the fluids are

$$\frac{\partial U}{\partial t} + \frac{\partial F}{\partial x} = 0 \tag{1}$$

where $U = (\rho, \rho u, \rho E)$ and $F = (\rho u, \rho u^2 + p, \rho u E + up)$.

1.2 FLASH

We assess the performance of the front tracking method with FLASH, based upon a test case involving a passive scalar front initialized to coincide with a density discontinuity.

We make use of the passive scalar in FLASH and compare its FLASH solution with and without the Front Tracking API. The passive scalar is a special variable for the hydrodynamics solver in FLASH. It is advected but no other physical characteristics are applied to this variable. To compare two solutions i.e mesh convergence or change of method (with or without FT) , we use the L_1 norm.

The PPM method (on which the FLASH USM method is based) has known problems with modeling the tip of an RT bubble. We observe unstable bubble tips (dimples) on the fiduciary grid starting at T = 4 seconds. This feature has no counterpart in experimental data. For this reason, we restrict our comparison time to T = 3 seconds.

1.3 Grids

We consider four grid levels, I: 75^2, II: 150^2, III: 300^2 and IV: 600^2. These are used to test convergence of the passive scalar in the Rayleigh-Taylor instability. Our fiducial solution uses grid V, a 1200^2 grid. The computational domain is $\Omega = [-0.25, 0.25] \times [-0.5, 0.5]$; the densities of the two fluids are $\rho_{heavy} = 2.0$ and $\rho_{light} = 1.0$. Each of these, including the fiducial solutions, are computed with and without tracking.

1.4 Solution Non Uniqueness

At the level of the Euler equations, the passive scalar is underspecified physically in that the dimensionless Schmidt number (viscosity/scalar field concentration

diffusion) is indeterminate. A sequence of viscous, diffusive solutions, converging to the Euler limit, is needed to specify the solution. However, there are infinitely many such sequences, parameterized by the Schmidt number. The limits are conjectured to be different for different Schmidt numbers. Even different formal limiting equations can result. Numerically, the solutions also have a potential non uniqueness and are parameterized by a choice of physical transport terms, as suggested above. For finite resolution (less than the direct numerical solution (DNS) criteria of complete resolution of all relevant scales, the numerical cutoff introduces the need for turbulent sub-grid terms, which also parameterize the non-uniqueness of solutions. Additionally, the numerical method, with its numerical viscosity and numerical concentration diffusion, can also parameterize the non unique solutions. This is what occurs here, with the tracked and untracked algorithms selecting a different solution. Sub-grid terms, recommended, but not part of the present analysis, would further modify the solution selected. A general framework, based on the Renormalization Group [1, 2] explains these issues in more detail, with numerical evidence presented there and in [4, 3]. After restricting the solution time to achieve qualitative agreement with experimental data, we do not encounter situations that lead to non uniqueness.

2 Simulation Convergence Methods

Let $\varphi_i(\mathbf{X}, t), i = 1, 2$, be the passive scalar field from two simulations (as, for example, computed with different grid sizes or by different methods) and let $\varphi_f(\mathbf{X}, t)$ be the fiducial solution. We define the L_1 error used to compare to these solutions.

Definition 1. The time dependent L_1 error on a computational domain Ω is defined as

$$||\varphi_1(\mathbf{X}, t) - \varphi_2(\mathbf{X}, t)||_{L_1} = \int_\Omega |\varphi_1(\mathbf{X}, t) - \varphi_2(\mathbf{X}, t)| dx \tag{2}$$

Tracked fronts, if any, in $\varphi_i(\mathbf{X}, t)$, give rise to cut cells, which are triangulated to allow separate integration in (2) on each side of the tracked interface. For this purpose, we use a Delaunay triangulation. We now define the L_1 convergence order to compare the untracked and tracked solutions. Let $\epsilon_i : \epsilon_V, i = I, \cdots, IV$, be the time dependent L_1 error for the tracked or untracked simulations as measured between the current and fiducial grid solutions.

Definition 2. The convergence order μ for the 8-fold grid refinement between grids I and V is defined as:

$$\mu(\epsilon) = \ln_8 (\ frac\epsilon_I : \epsilon_V \epsilon_{IV} : \epsilon_V) \tag{3}$$

3 Results

The RT instability is initialized with a flat interface separating two fluids of different densities. The velocity field is perturbed, which excites the RT fluid

instabilities. A time independent acceleration from gravity pushes down on the heavier fluid. The Euler equations are solved; the interface describes the time evolution of the density discontinuity. The results are taken at $T = 3.0$ seconds, after the beginnings of a roll up region has formed on each side of the RT fingers.

We compare the numerical solution errors on grids I-IV as the difference with the solution from the fiducial grid. The L_1 norms of the differences generate the convergence data of Table 1 and the rates of convergence of Table 2. We observe somewhat better than second order convergence with tracking and somewhat better than first order convergence without tracking. The difference between the two fiducial solutions at $T = 3.0$ seconds is 8.65e-04, which is comparable to the untracked grid IV mesh errors. From this fact, we infer that the two solutions (tracked and untracked) are converging to a common solution.

Table 1: L_1 error at $T = 3$ seconds

	I	II	III	IV
FLASH without FT	0.011295	0.002327	0.001019	0.000922
FLASH with FT	0.006833	0.001408	0.000616	0.000057

Table 2: Convergence Rates at $T = 3$

	Order in L_1
FLASH without FT	1.2
FLASH with FT	2.3

Figure 1 shows the solution of the passive scalar with and without front tracking for the four grid levels at T = 3 seconds. Each frame shows the color contour plot of the untracked scalar field concentration, with the tracked front superimposed. The tracked concentration field (not shown) is purely red on one side of the tracked front and purely blue, on the other, with no yellow or green values. Figure 2 shows the an enlarged detail from the FLASH fiducial passive scalar solutions at T = 3. The three frames show the untracked solution with the tracked front superimposed, the untracked solution without the tracked front, and the front only from the tracked solution.

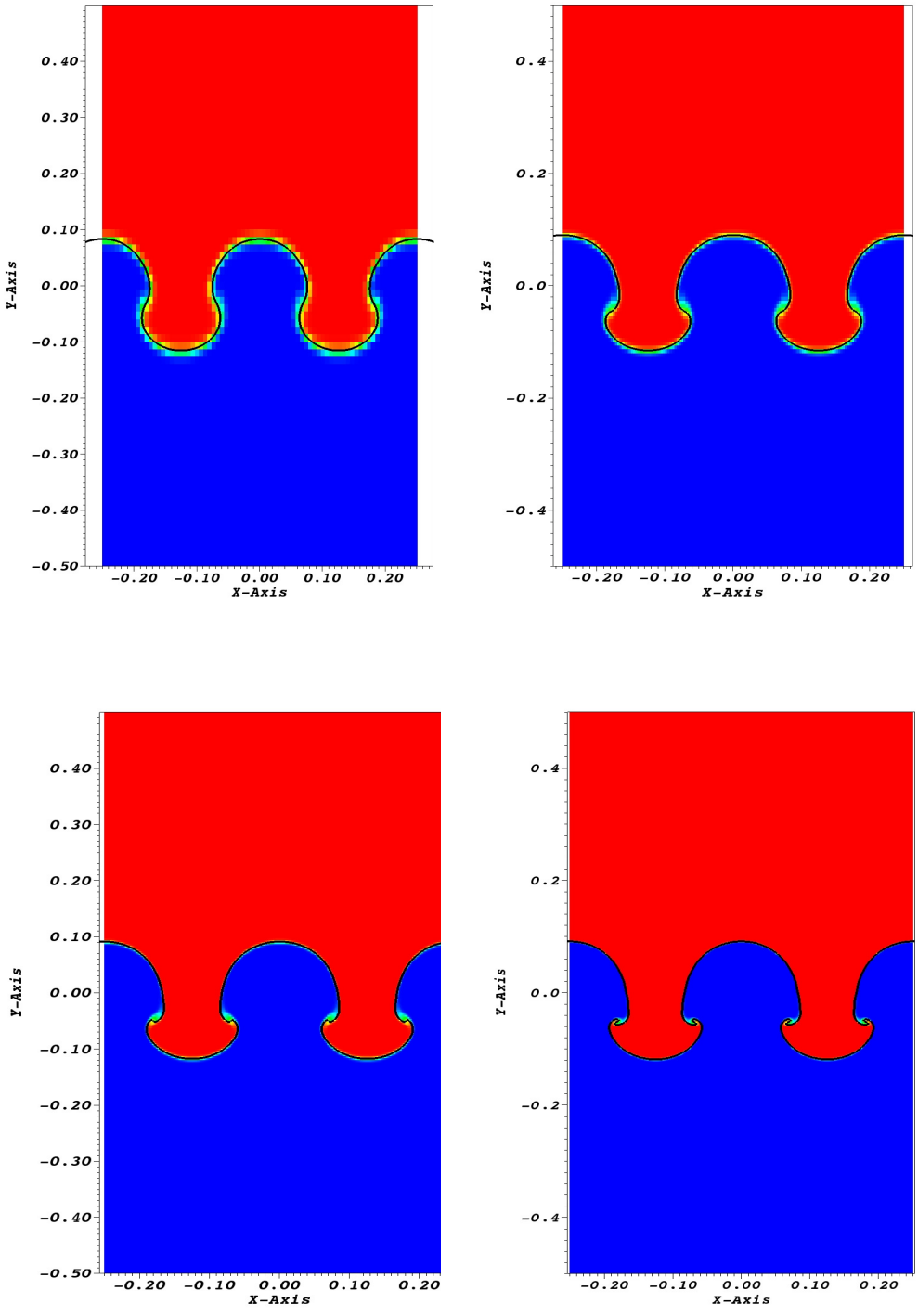

Figure 1: FLASH with FT, T = 3 seconds, for a sequence of grid levels, I – IV. The untracked scalar concentration is shown in a color contour plot, with the tracked front superimposed.

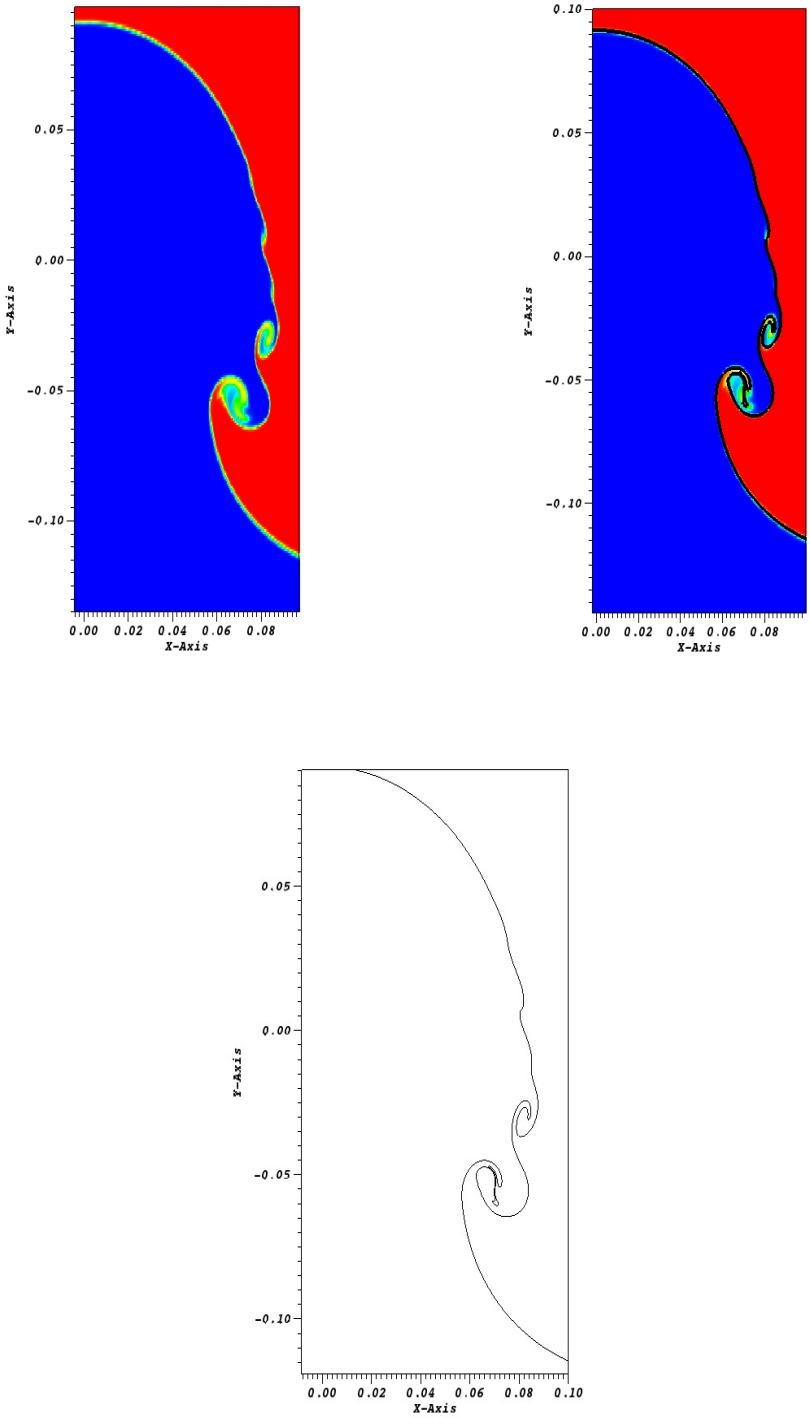

Figure 2: FLASH with FT, T = 3 seconds, using the fiducial grid V. Above left: the untracked scalar field concentration. Above, right: the tracked scalar field concentration. Below: the front taken from the tracked simulation.

4 Discussion

In this paper, we report a quantitative comparison of errors for a passive scalar in RT instability simulations. We compare the errors for tracked and untracked methods. We summarize the results in the following fashion.

1. The two solutions (tracked and untracked) converge to a common limit for a limited time. The tracked solution, with smaller errors, converges more rapidly.

2. We show convergence quantitatively, tabulating L_1 norm measures of grid errors and visually, through display of color contour plots of the values of the passive scalar concentration (untracked), with the tracked front superimposed.

3. The time of solution comparison is limited to $T = 3$ seconds to avoid solutions in disagreement with experiments, a known feature of PPM, on which this solver is based.

4. At later times the tracked and untracked solutions each continue to converge to their own limits, but these limits are distinct for the grids considered here.

Our next step will be the addition of active tracking, which will allow the modeling of active as well as passive solution fronts.

References

[1] J. Glimm, B. Plohr, and D. Sharp. Large eddy simulation, turbulent transport and the renormalization group. *arXiv*, arxiv.org > physics.flu-dyn > 1308.3221, 2013. Los Alamos National Laboratory Preprint Number LA-UR-12-26149, Stony Brook University Preprint Number SUNYSB-AMS-12-02.

[2] J. Melvin, R. Kaufman, H. Lim, T. Kaman, P. Rao, and J. Glimm. Macro and micro issues in turbulent mixing. *Science China*, 2013. In Press.

[3] J. Melvin, P. Rao, R. Kaufman, H. Lim, Y. Yu, J. Glimm, and D. H. Sharp. Atomic scale mixing for inertial confinement fusion associated hydro instabilities. *High Energy Density Physics*, 2013. In Press. Stony Brook University Preprint SUNYSB-AMS-12-01 and Los Alamos National Laboratory Preprint LA-UR 12-21555.

[4] J. Melvin, P. Rao, R. Kaufman, H. Lim, Y. Yu, J. Glimm, and D. H. Sharp. Turbulent transport at high reynolds numbers in an icf context. *ASME Journal of Fluids Engineering*, submitted(Stony Brook University Preprint Number SUNYSB-AMS-13-02, Los Alamos National Lab LAUR Number LA-UR-13-20765), 2013.

Appendix B

Sensitivity of ICF Hot Spot Properties to the DT Fuel Adiabat

[Physics of Plasmas, Accepted]

Sensitivity of ICF Hot Spot Properties to the DT Fuel Adiabat

J. Melvin,[1] H. Lim,[1] V. Rana,[1] B. Cheng,[2] J. Glimm,[1] D. H. Sharp,[2] and D. C. Wilson[2]

[1)] *Department of Applied Mathematics and Statistics, Stony Brook University, Stony Brook, NY 11794-3600, USA*

[2)] *Los Alamos National Laboratory, Los Alamos, NM 87545, USA*

We determine the dependence of key Inertial Confinement Fusion (ICF) hot spot simulation properties on the Deuterium-Tritium (DT) fuel adiabat, here modified by addition of heat to the cold shell. Variation of this parameter reduces the simulation to experiment discrepancy in several experimentally inferred quantities. The dependence is tested in four ways, through two simulation codes and two solution scenarios (an untuned generic Rev. 5 design and a post shot radiation tuned design). Our simulations are continued from capsule only 1D simulations using the Lawrence Livermore National Laboratory ICF code, HYDRA. The continuations employ a hydro only code, FronTier, modified with a radiation equation of state (EOS) model and the High Energy Density Physics (HEDP) University of Chicago code, FLASH. We show sensitivities of various measured quantities to the enhancement of initial entropy. Hot spot densities, burn-weighted ion temperatures and pressures show a decreasing trend, while the hot spot radius shows an increasing trend. In addition we use a theoretical model to predict 3D mix and observe a trend toward less mixing as the entropy is enhanced. Instantaneous quantities are assessed at the time of maximum neutron production within each simulation. These trends contribute to ICF science, as an effort to understand the NIC campaign simulation to experiment discrepancy, and in their relation to the high foot experiments, which features a higher adiabat in the experimental design and an improved neutron yield in the experimental results.

Keywords: ICF, Rayleigh-Taylor instabilities, hot spot, deceleration phase, adiabat

I. INTRODUCTION

The science mission of NIF, as recently emphasized[1], is to produce valuable experimental data from fusion ignition capsule implosions. The goal of improving the agreement between experiment and simulation is discussed in Clark et al (2013)[2]. Here we pursue this theme, by studying variations in an important parameter, the Deuterium-Tritium (DT) fuel adiabat, with a potential to improve the agreement of simulation with experiment. We consider in detail shot N120321, taken from the National Ignition Campaign (NIC) series. This shot, as is typical for this series, has a sequence of shocks (called low foot) whose goal is to produce a low adiabat for the trajectory of the compression. The simulations of such shots overpredict the experimentally measured quantities[2].

Our simulations are of four types, a Rev. 5 design[3] (untuned), a post-shot radiation drive modification of this design[2], a simulation with a higher adiabat and a combined (twice tuned) simulation with both the modified radiation drive and a higher adiabat. The higher adiabat, or entropy enhanced simulation[4] is achieved through a uniform increase in the temperature (adding internal energy at constant density) to the cold DT fuel. These simulations are continuations of two HYDRA[5] capsule only simulations which have reached the time of maximum implosion velocity. These two HYDRA simulations differ by the use of the post-shot radiation drive tuning to model shot N120321. The tuning achieves agreement with early time shock velocity and shock breakout VISAR data and Convergent Ablator (ConA) implosion trajectory and velocity data[2], all measured before the time of peak velocity. The radiation drive in a capsule only simulation occurs as an external source. Modification to this source results in simulated shock velocities, hot spot trajectories and bang time in agreement with experimental data[2,6]. We continue the simulation through the time of hot spot formation and maximum neutron production.

The continuation simulations rely on two alternate simulation codes, a hydro only front-tracking code, FronTier (FT)[7,8] enhanced with a radiation ideal fluid equation of state (EOS), and the University of Chicago high energy density physics (HEDP) code FLASH[9]. To support the results observed with these alternate simulation codes, we first compare simulations of the three codes and find them in reasonable, but not perfect, agreement. We identify three main physics model differences between HYDRA and our use of FLASH: 1. the EOS model, 2. the TOPS opacity data and 3. the treatment of thermal diffusion for

electrons.

Our main results are trends, observed consistently across all simulations considered here. Within these trends, we observe improved comparison to experimentally inferred quantities. Hot spot pressure and density, burn-weighted ion temperature and 3D mix, as modeled here, are sensitive to the DT fuel adiabat. All decrease as the initial adiabat increases. The hot spot radius and the burn width both increase with added entropy. Within each simulation model studied, the enhancement of the initial entropy reduces the discrepancy with the experimentally measured quantities. These conclusions suggest that hot spot thermodynamics could be a key in future efforts to achieve agreement between NIF experimental data and simulations. The high foot experiments, which use a high DT fuel adiabat, achieved improved ICF performance[10] and improved agreement with simulations relative to the low foot experiments.

In Sec. II we describe the procedure for the continuation simulations and we discuss differences in physics models across the simulation codes. In Sec. III we compare the hot spot properties for simulations without entropy enhancement with the HYDRA, FT and FLASH codes. In Sec. IV we show consistent trends in the results of entropy tuning in an already radiation tuned simulation. In Sec. V we analyze 3D mix as predicted by a mix model, and in Sec. VI we summarize our findings.

II. COMPUTATIONAL METHODOLOGY

1D untuned and post shot HYDRA simulations of the ICF capsule were performed, the former using a Rev. 5 framework[3] and the latter[2] with a radiation drive modified to match shot N120321. Data dumps starting at the time of maximum implosion velocity provide initial conditions and boundary data for continuation simulations using alternate simulation codes. The outer edge of the DT fuel is taken as the boundary point of the continuation simulation, with boundary conditions specified there from the HYDRA data. Our continuation simulations focus on the deceleration phase at the time of hot spot formation, run through maximum neutron production and terminate once the neutron production has become negligible. Models to redeposit energy from the nuclear burn and alpha heating are not included in these simulations. Continuations were provided by three codes, HYDRA itself, the HEDP code FLASH[9] and the hydro code FronTier[7,8].

A. FLASH

FLASH[9] is an Eulerian multi-physics code with multiple modules that can be joined together for a particular application. Here, we use a directionally split PPM hydro solver coupled with a $3T$ multigroup diffusion radiation model and a Lee-More[11] electron conduction model. For the EOS, we use an ideal fluid as described in Sec. II B. The multigroup diffusion is implemented with sixty energy groups, twenty-five between .03 keV and 1 keV, twenty-five between 1 keV and 5 keV and ten from 5 keV to 50 keV. Within each block, log-spacing is used. The opacities come from the Los Alamos National Laboratory TOPS code `http://aphysics2.lanl.gov/opacity/lanl` where an assumed 50/50 number fraction of Deuterium and Tritium is used. Other than as described above, we leave all necessary FLASH initialization parameters for these chosen modules at their default values. A benchmark comparison study of FLASH and HYDRA, including experimental validation[12], produced generally excellent agreement. A more detailed description of the FLASH simulation code, including the choices made here is available in Melvin et al (2014)[13].

B. FronTier

FronTier[7,8] is an Eulerian one temperature (T) hydro code with a Spitzer temperature dependent thermal conductivity (κ_{sp}) set to the electron conductivity[14,15], based on an assumed equilibration of the electron and ion temperatures. Using an optically thick radiation equilibrium diffusion approximation to simplify the coupled equations[16], radiation effects are approximated through a radiation modified ideal fluid EOS, following the formalism described in Lowrie and Morel (2001)[17]. Such an assumption may not be proper for ignition capsules. The ideal fluid EOS uses a temperature dependent adiabat index function $\gamma = \gamma(T)$, set to $\gamma(T) = 5/3$ in the hot spot and $\gamma(T) = 7/4$ in the cold fuel (See Melvin et al (2014)[13]). The single temperature T is used to set the radiation energy density e_r equal to aT^4, with a the radiation constant. During the decleration phase, radiation pressure is negligible compared to matter pressure, and thus the radiation pressure contribution to total pressure is neglected.

The total pressure is thus initialized as $P = P_i + P_e + P_c$ (P_c = cold pressure) and is represented as a single pressure throughout the simulation. P is then used to initialize the

matter specific internal energy through the typical ideal gas EOS relation, $e_m = \frac{P}{(\gamma(T)-1)\rho}$. Total specific internal energy is $e^* = e_m + e_r/\rho$. The total energy density then becomes $e_{tot} = \rho e^* + \frac{1}{2}\rho v^2$, leading to the equations

$$\begin{aligned} \frac{\partial \rho}{\partial t} + \nabla \cdot (\rho \mathbf{u}) &= 0 \ , \\ \frac{\partial \rho \mathbf{u}}{\partial t} + \nabla \cdot (\rho \mathbf{u}\mathbf{u}) + \nabla P &= 0 \ , \\ \frac{\partial e_{tot}}{\partial t} + \nabla \cdot (e_{tot}\mathbf{u} + P\mathbf{u}) &= \nabla \cdot \kappa_{sp} \nabla T \ . \end{aligned} \tag{1}$$

For further details on the implementation of the radiation EOS, see Melvin et al (2014)[13].

III. COMPARISON OF 1D ICF SIMULATIONS

The untuned HYDRA simulation presented in Fig. 1 is a generic version of the Rev. 5 design, and does not correspond to any specific experiment. The time of comparison (determined separately within each simulation) is set to the maximum neutron production time. In Fig. 1 we plot the density (left frame) and ion temperature (right frame) as given by each code, using the untuned simulations. The FLASH and HYDRA simulations are in qualitatively good agreement, while the more pronounced differences between these two and FT may be related to the simplified radiation model in FT. From the point of view of experimental data, the most sensitive aspects of these figures are their description of the hot spot properties. The 1D HYDRA simulations often over predict the inferred hot spot density and temperature compared to NIC experimental data. In this regard, Fig. 2 which repeats this comparison using the HYDRA code with a tuned radiation drive shows a significant decrease in density, which is a big improvement over Fig. 1.

IV. TRENDS FOR ENTROPY ENHANCED SIMULATIONS

We establish trends for the effects of initial entropy enhancement. Our main result is the strong sensitivity of hot spot density and predicted mix to additional entropy. Hot spot ion temperature decreases only slightly, while the hot spot radius increases. As this is affected by 3D mix, not included in the present simulations, a basis for direct comparison to experimental data is not apparent for the radius.

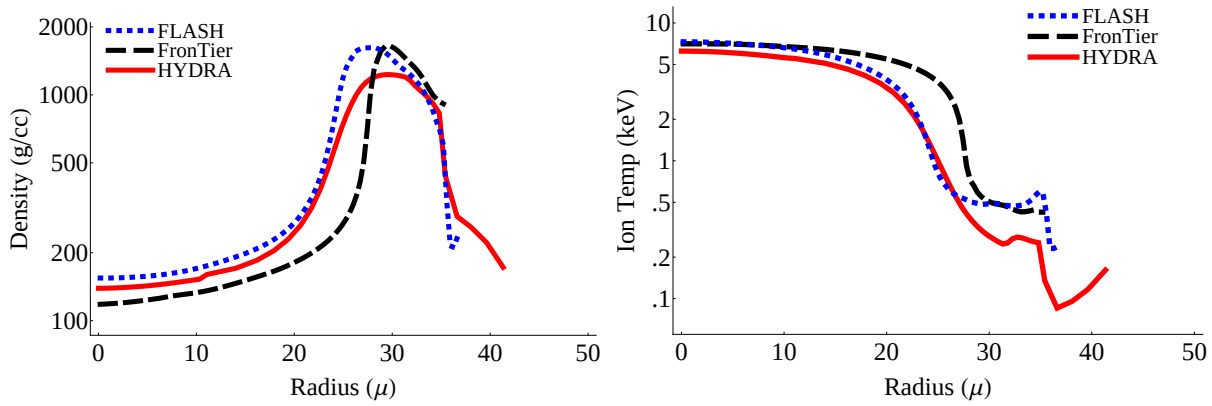

FIG. 1. Untuned simulations. Comparison of FronTier, FLASH and HYDRA continuation simulations at approximate maximum neutron production time. Dashed lines represent FronTier simulations, dotted lines, FLASH and solid lines HYDRA. Left frame: density, right frame: ion temperature.

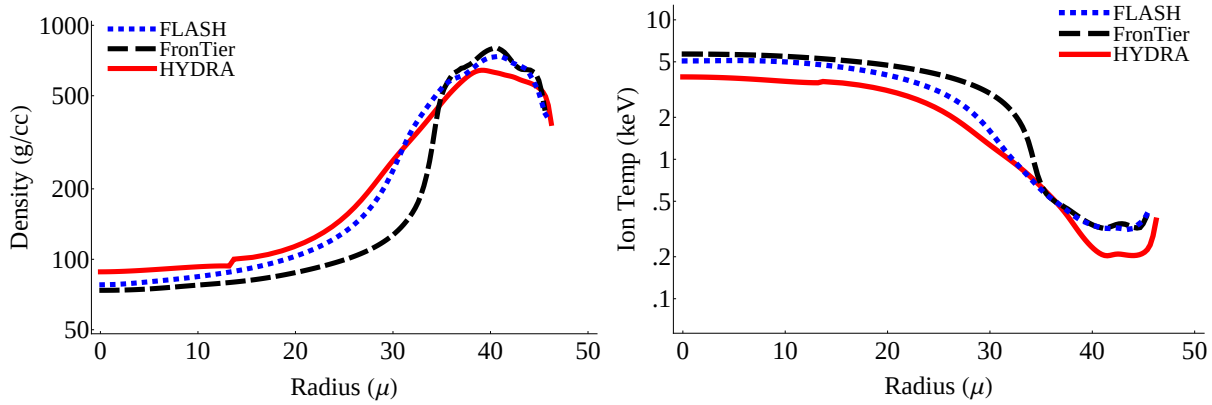

FIG. 2. Radiation drive tuned simulations. Comparison of FronTier, FLASH and HYDRA continuation simulations at approximate maximum neutron production time. Dashed lines represent FronTier simulations, dotted lines, FLASH and solid lines, HYDRA. Left frame: density, right frame: ion temperature.

Fig. 3 shows the effects of variation of preheat in simulations without tuning of the radiation drive and Fig. 4 shows the same comparison for simulations with a radiation tuned drive. From Figs. 3 and 4 we observe clear trends towards lower densities in both the hot spot and the cold shell as the cold shell moves to a higher adiabat. In addition, an improved agreement of the hot spot density with the experimentally inferred density is

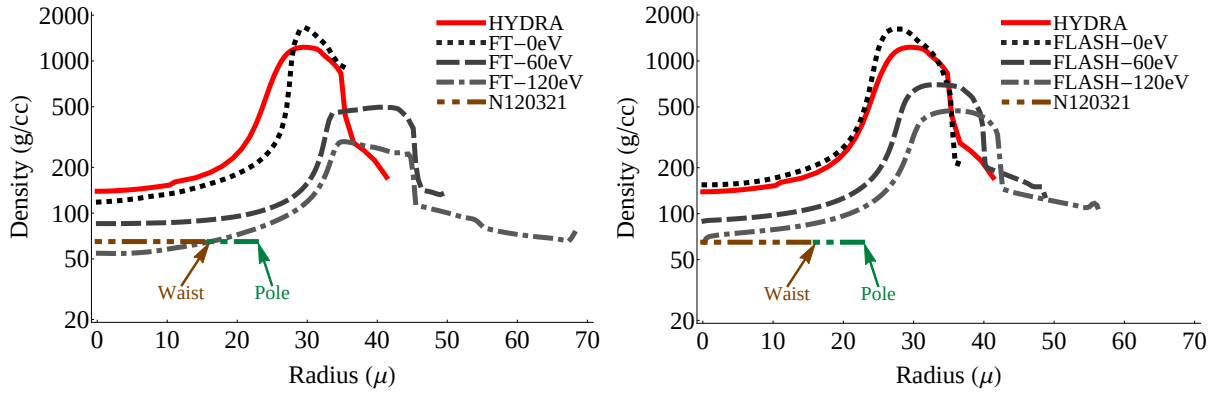

FIG. 3. Simulations without radiation drive tuning. Plot of density of continuation simulations using three values of cold shell preheat. Left frame: FT (0eV, 60eV and 120eV), right frame, FLASH (0eV, 60eV and 120eV), with comparison to the untuned HYDRA simulation and experimental values for shot N120321[18]. The experimental waist and (larger) pole radii are shown separately.

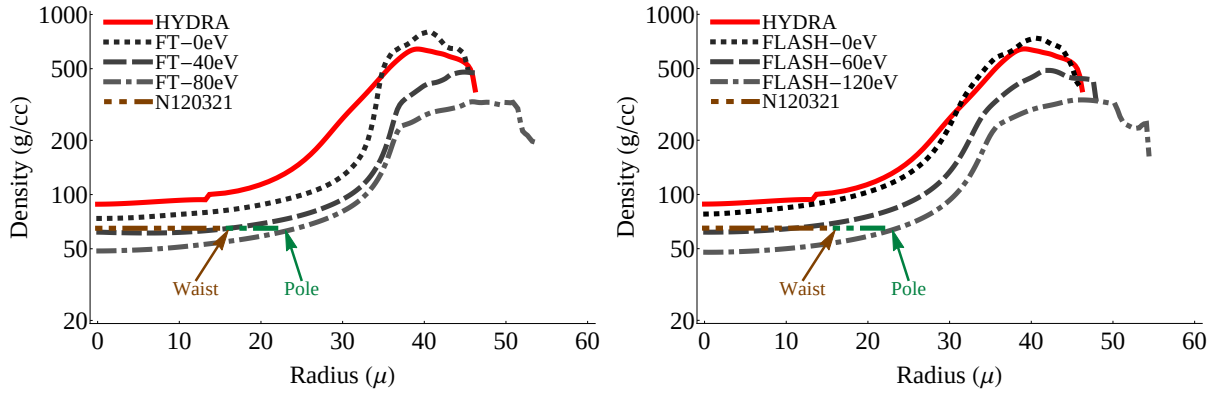

FIG. 4. Radiation drive tuned simulations. Plot of density of continuation simulations using three values of cold shell preheat. Left frame: FT (0eV, 40eV and 80eV), Right frame: FLASH (0eV, 60eV and 120eV), with comparison to the radiation tuned HYDRA simulation and experimental values for shot N120321[18]. The experimental waist and (larger) pole radii are shown separately.

observed. To account for these density trends, we note that added energy in the cold fuel has the effect of introducing less compression, which lowers the hot spot density and increases the hot spot radius.

In Figs. 5 we compare the ion temperatures at maximum neutron time among the same set of preheat simulations. For brevity, we only show radiation drive modified simulations.

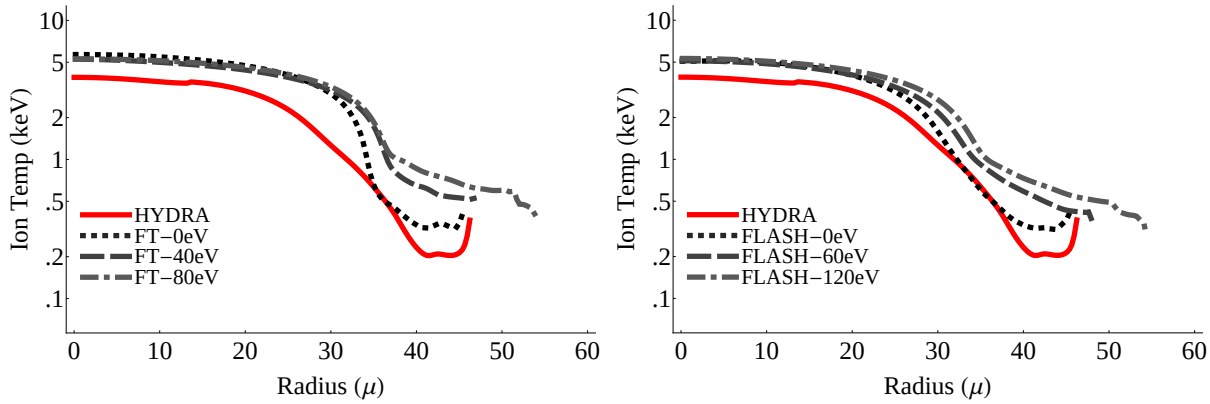

FIG. 5. Radiation drive modified simulations. Plot of temperature of continuation simulations using three values of cold shell preheat. Comparisons of Left frame: FT (0eV, 40eV and 80eV), Right Frame: FLASH (0eV, 60eV and 120eV) to HYDRA continuation simulations.

Overall, FLASH and FT have ion temperatures which are high compared to the HYDRA simulation, which we believe is a result of the thermal conduction model differences. Across the preheat simulations, we observe that the ion temperature shows little change at maximum neutron time. To facilitate ion temperature comparisons with experimentally inferred burn weighted values, we present in Table I the burn weighted ion temperatures amongst the radiation tuned simulations and experiment. Burn-weighted temperatures are calculated as an integral over time and space of the neutrons created multiplied by the temperature. We then divide by the total yield to get the overall burn-weighted temperature. We see that the burn weighted temperatures show a decreasing trend under preheat towards the experimentally inferred value. The HYDRA simulation presented here has 30μg of CH mixed into the fuel initially[2] and uses an FDS diffusion source to drive the capsule. These initial conditions for HYDRA may contribute to the lower than experimentally inferred burn weighted ion temperature value. We also present the burn widths for the various simulations in Table I. The burn width or full width half maximum is defined as the time period during which at least 50% of the maximum neutron production rate is observed. We see that the burn widths also are sensitive to entropy enhancement. The added entropy flattens out the burn, so that the burn width increases as the entropy increases. This tuning can bring the burn width into good agreement with the experimentally inferred values as evidenced by the FLASH 60eV simulation.

TABLE I. Comparison of 1D experimentally inferred burn weighted ion temperature and burn width with post shot (radiation drive and adiabat tuned) simulation quantities for shot N120321[18].

	$(T_i)_{bw}$(keV)	Burn Width (ps)
Experiment N120321	3.10	135
HYDRA (1D; this work)	2.80	111
FLASH (1D, 00eV)	3.67	103
FLASH (1D, 60eV)	3.54	140
FLASH (1D, 120eV)	3.51	159
FT (1D, 0eV)	3.85	118
FT (1D, 40eV)	3.61	199
FT (1D, 80eV)	3.54	239

In Fig. 6 we compare the pressures among the preheat simulations and the corresponding experimentally inferred pressure. We observe that pressure is also sensitive to entropy enhancement and decreases as the entropy is increased. For the range of preheats considered here, the hot spot density reaches approximately the experimentally inferred value, however in all codes, the calculated hot spot pressure and burn-weighted ion temperatures are slightly too high compared to experimentally inferred quantities. We do not report the calculated neutron yield or compare the results obtained for the neutron yield with different codes to each other or to experiment because we have not validated the methodology used for the computation of neutronics either in FT or in FLASH.

V. MULTIDIMENSIONAL INSTABILITY GROWTH

A. Validation of 3D Mix Model with its Parameter Settings

Values for RT and RM instability growth rates based on simulation[19–24] and theory[25] are consistent with numerous experiments[26–28]. Most notable among these is the dimensionless RT bubble growth rate in the planar case, $\alpha_b = h_b/Agt^2$, where h_b is the bubble instability penetration distance, A the Atwood number and g the acceleration. The bubble and spike side growth rates α_b and α_s are linked by a single theory[29], and this theory is linked to the RM growth rate exponents θ_b and θ_s. In these theories, there is a single free parameter

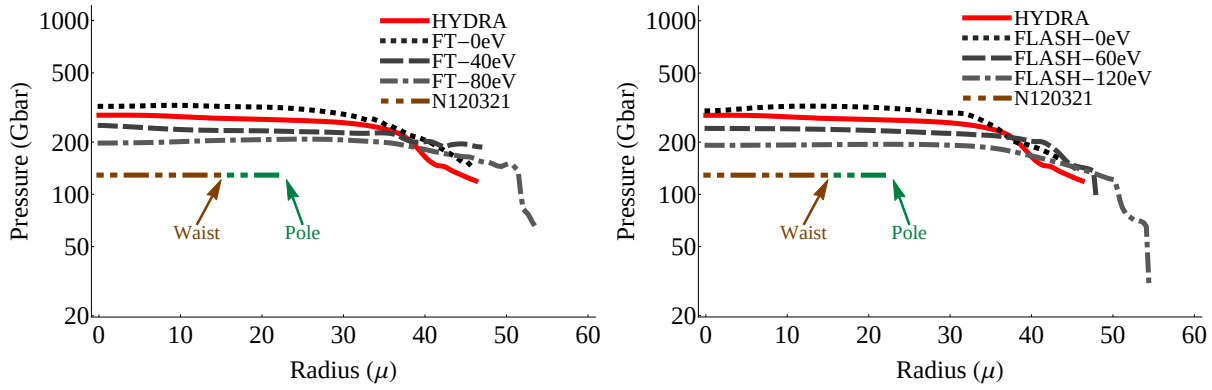

FIG. 6. Radiation drive modified simulations. Plots of pressure of continuation simulations using three values of cold shell preheat. Comparisons of Left frame: FT (0eV, 40eV and 80eV), Right Frame: FLASH (0eV, 60eV and 120eV) to HYDRA continuation simulations and experimental values from shot N120321[18].

governing the totality of two alphas and two thetas, and this parameter can be set in a variety of ways, e.g., theoretically by appeal to bubble merger models[25], experimentally[26] or through validated simulations[21]. Small differences observed among the (consistently normalized) growth rate constants or exponents between individual experiments can be captured accurately by high quality simulations, and in most cases explained as primarily due to changes in the physical transport properties between different experiments[21]. Initial condition effects, often discussed, are shown to play a small role in many experiments[24], but are significant for the (noisy) splitter plate water channel experiments[23]. These ideas were extended to the case (relevant here) of nonuniform gravity[30].

We apply the well established theory of RT/RM growth rates to the ICF instabilities. Among the several approximations involved in our use of this model, we mention: the use of planar (not spherical) geometry to determine the drag coefficient from Rayleigh-Taylor data, the assumption of only small perturbations at the onset of the deceleration instability, and the moderate Prandtl number RT simulations/experiments to calibrate the mix model for application to a small Prandtl number problem, namely the mix associated with the cold fuel shell deceleration in ICF. Of these three factors, the first two will increase the mixing and the third will decrease it.

B. Mix Predictions

Spike penetration into the hot spot limits alpha heating and lowers overall neutron yield. We estimate the spike penetration into the hot spot based on a 3D RT mix model. The spike penetration is estimated from a theoretical model based on a variable acceleration buoyancy drag equation[30], which gives

$$h_s = \int_0^t \int_0^{s_1} 2\alpha(s)A(s)g(s)dsds_1 \tag{2}$$

using the data of the 1D simulations. The Atwood number and the acceleration depend on the time as shown in Fig. 7. The coefficient $\alpha(s)$ comes from Cheng et al (2000)[29]. In using this reference we need a value for the bubble RT mixing rate α_b. We are not aware of either numerical or experimental studies of RT mixing with a small Prandtl number. Appealing to data from Melvin et al. (2012)[31] and Melvin et al. (2013)[32], we expect a grid dependent modification of the total Prandtl number (turbulent and atomic) in the range of a factor of 2 to 10, meaning that after accounting for turbulence effects, the Prandtl number remains small. Conventional numerical studies of RT mixing have substantial numerical diffusion, and small numerical Prandtl numbers. For this reason we use these estimates, which typically give a value $\alpha_b \sim 0.02 - 0.03$, and derive the spike penetration from this estimate and the methodology of Cheng et al (2000)[29]. The Atwood number, A, is defined as $A = (\rho_h - \rho_l)/(\rho_h + \rho_l)$, where ρ_h is the maximum density in the cold shell and ρ_l is the minimum density in the hot spot.

The acceleration is determined by tracking the lagrangian motion of a point where $dP \cdot d\rho < 0$ (RT unstable) and integrating the velocity field observed for this point. We then average the acceleration data over time to remove numerical noise.

Fig. 7 presents two factors that enter in (2), namely the Atwood number A and the deceleration g. The third factor, $\alpha(s)$, is a nonlinear function of A and is not plotted separately. In these frames we compare separately the effect of preheat on these variables in the FT (above) and FLASH (below) simulations. The corresponding variable for HYDRA is shown in each frame, but is not part of the comparison. The purpose of these frames is to give an understanding of the elements contributing to the spike penetration as the preheat is varied. For this reason, we emphasize the comparison of the plots for a single code.

We observe in Fig. 7's left frames that preheat causes a reduction in the Atwood number. This impact is amplified by the effect of $A(s)$ on $\alpha(s)$. The preheat deceleration forces act

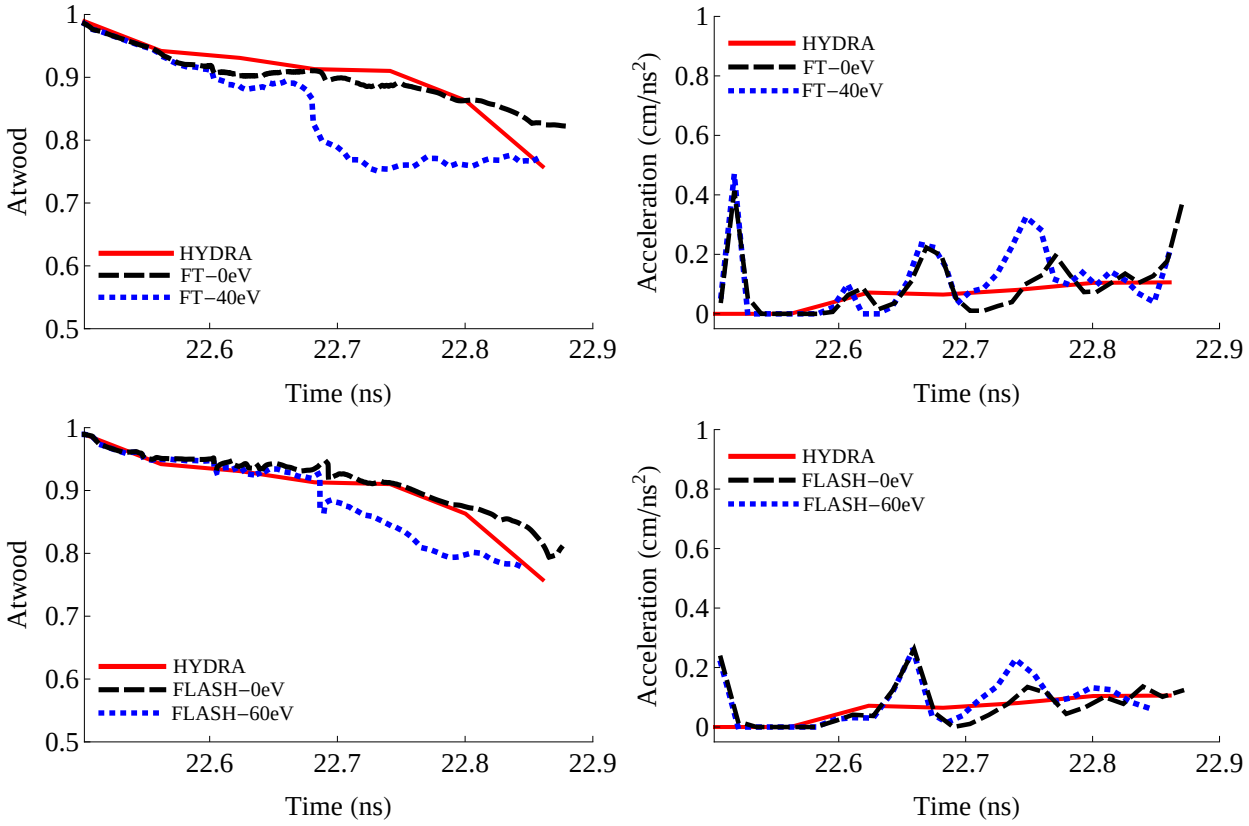

FIG. 7. Radiation drive modified simulations. Atwood number vs. time (left). Acceleration vs. time (right). FT - 0eV, FT - 40eV and HYDRA (above). FLASH - 0eV, FLASH - 60eV and HYDRA (below).

over a shorter time period, but are larger (See Fig. 7, right). Combining both deceleration and Atwood number effects, we see a decrease in mixing predicted by the mix model for the case of added preheat.

Table II shows the sensitivity of 3D RT growth on increases of the adiabat in the cold fuel. The sensitivity of hot/cold fuel mix to the cold fuel adiabat is apparent. The drop in spike penetration into the hot spot is due primarily to a change in the Atwood number for these simulations. While this change results in more favorable conditions for ignition, the loss of density and ion temperature in the hot spot as shown above suggests that overall, the entropy added simulations are less favorable to ignition. We note that the HYDRA entry on the table is calculated from very few datapoints as only a small subset of the simulation data was made available.

TABLE II. Comparison of spike penetration into the hot spot based on mix model predictions and on data from FT, FLASH and HYDRA simulations with a radiation tuned drive.

Simulation	spike penetration depth (μm)	hot spot mixed radial fraction (%)
HYDRA	$5-8$	$14-23$
FT - 0eV	$6-10$	$18-30$
FT - 40eV	$6-9$	$16-27$
FT - 80eV	$4-7$	$12-20$
FLASH - 0eV	$6-9$	$18-30$
FLASH - 60eV	$5-8$	$14-23$
FLASH - 120eV	$4-6$	$10-16$

VI. CONCLUSIONS

We have identified hot spot thermodynamic properties as a possible driver of significant discrepancies between preshot simulations and ICF NIC (lowfoot) experiments, specifically considering shot N120321. This assertion is based on prior studies combined with the analysis offered here. Likewise, the radiation drive and the 3D mix present important issues.

We have performed multiple 1D simulations of ICF capsules, taken from the time of maximum implosion velocity through neutron production. Using a fully integrated simulation to define the external radiation drive, a capsule only simulation in HYDRA was run and a data dump at the time of maximum implosion velocity was used to initialize further simulations. Using FronTier, a hydro only code and FLASH, a HEDP code, continuation simulations were compared to the results from HYDRA.

Entropy was added to the cold fuel in the FronTier and FLASH simulations, through a uniform addition to the temperature in the cold fuel at initialization. When these simulations are run to the point of maximum neutron production, they show less favorable conditions for ignition, a larger hot spot radius with smaller densities and nearly unchanged ion temperatures in the hot spot, as compared to the non-modified simulations across the two simulation codes FT and FLASH.

The Atwood number and deceleration, taken at a tracked Lagrangian point, representing the approximate cutoff between the hot spot and cold fuel, were used as input to a model for 3D RT growth. A significant decrease in theoretical model prediction of 3D mixing of hot/cold fuel in the entropy modified simulations was apparent. This result is qualitatively consistent with recent NIF high foot experimental data[33]. Future studies (2D and 3D) will allow quantitative analysis of this effect.

ACKNOWLEDGMENTS

The authors thank Dan Clark and Marty Marinak for permission to use HYDRA and the radiation tuned input files. The authors also thank Chris Fontes for assistance in retrieving proper opacity data through TOPS. In addition, the authors thank T.J.T. Kwan, S. Batha and P. Bradley for their support and helpful discussions. This work is supported in part by Leland Stanford Junior University 2175022040367A (sub award with DOE as prime sponsor), Army Research Office W911NF0910306. This manuscript has been co-authored by Los Alamos National Laboratory, under Contract No. JL3K00 NYSB0000, Inertial Confinement Fusion Campaign. This manuscript has been co-authored by Brookhaven Science Associates, LLC, under Contract No. DE-AC02-98CH1-886 with the U.S. Department of Energy. The United States Government retains, and the publisher, by accepting this article for publication, acknowledges, a world-wide license to publish or reproduce the published form of this manuscript, or allow others to do so, for the United States Government purposes. This research used resources of the National Energy Research Scientific Computing Center, which is supported by the Office of Science of the U. S. Department of Energy under Contract No. DF-AC02005CH11231.

REFERENCES

[1]W. Goldstein and R. Rosner, "Workshop on the science of fusion ignition on NIF," Tech. Rep. LLNL-TR-570412 (LLNL, 2012).

[2]D. S. Clark, D. E. Hinkel, D. C. Eder, O. S. Jones, S. W. Haan, B. A. Hammel, M. M. Marinak, J. L. Milovich, H. F. Robey, L. J. Suter, and R. P. J. Town, Physics of Plasmas **20**, 056318 (2013).

[3]S. W. Haan, D. Lindl, D. A. Callahan, D. S. Clark, J. D. Salmonson, B. A. Hammel, L. J. Atherton, R. C. Cook, M. J. Edwards, S. Glenzer, A. V. Hamza, S. P. Hatchett, M. C. Herrman, D. E. Hinkel, H. D, D, H. Huang, O. S. Jones, J. Kline, G. Kyrala, O. L. Landen, B. J. MacGowan, M. M. Marinak, D. D. Meyerhofer, J. L. Milovich, K. A. Moreno, E. I. Moses, D. H. Munro, A. Nikroo, R. E. Olson, K. Peterson, S. M. Pollaine, J. E. Ralph, H. F. Robey, B. K. Spears, P. T. Springer, L. J. Suter, C. A. Thomas, R. P. Town, R. Vesey, S. V. Weber, H. L. Wilkins, and D. C. Wilson, Phys. Plasmas **18**, 051001 (2011).

[4]B. Cheng, T. Kwan, Y.-M. Wang, and S. Batha, Phys. Rev. E **88**, 041101 (2013).

[5]M. M. Marinak, G. D. Kerbel, J. M. Konig, M. V. Patel, S. M. Sepke, B. Chang, P. Michel, and D. Larson, LLNL-PRES-496758 (2011).

[6]O. S. Jones, C. J. Cerjan, M. M. Marinak, J. L. Milovich, H. F. Robey, P. T. Springer, L. R. Benedetti, D. L. Bleuel, E. J. Bond, D. K. Bradley, D. A. Callahan, J. A. Caggiano, P. M. Celliers, D. S. Clark, S. M. Dixit, T. Doppner, R. J. Dylla-Spears, E. G. Dzentitis, D. R. Farley, S. M. Glenn, S. H. Glenzer, S. W. Haan, B. J. Haid, C. A. Haynam, D. G. Hicks, B. J. Kozioziemski, K. N. LaFortune, O. L. Landen, E. R. Mapoles, A. J. MacKinnon, J. M. McNaney, N. B. Meezan, P. A. Michel, J. D. Moody, M. J. Moran, D. H. Munro, M. V. Patel, T. G. Parham, J. D. Sater, S. M. Sepke, B. K. Spears, R. P. J. Town, S. V. Weber, K. Widmann, C. C. Widmayer, E. A. Williams, L. J. Atherton, M. J. Edwards, J. D. Lindl, B. J. MacGowan, L. J. Suter, R. E. Olson, H. W. Herrmann, J. L. Kline, G. A. Kyrala, D. C. Wilson, J. Frenje, T. R. Boehly, V. Glebov, J. P. Knauer, A. Nikroo, H. Wilkens, and J. D. Kilkenny, Physics of Plasmas **19**, 056315 (2012).

[7]E. George, J. Glimm, J. W. Grove, X.-L. Li, Y.-J. Liu, Z.-L. Xu, and N. Zhao, in *Hyperbolic Problems: Theory, Numerics, Applications*, edited by T. Hou and E. Tadmor (Springer Verlag, Berlin and New York, 2003) pp. 175–184.

[8]W. Bo, X. Liu, J. Glimm, and X. Li, SIAM J. Sci. Comput. **33**, 1505 (2011).

[9]P. MacNeice, K. M. Olson, R. de Fainchtein, and C. Parker, Computer Physics Comm. **126**, 330 (2000).

[10]H. S. Park, O. A. Hurricane, D. A. Callahan, D. T. Casey, E. L. Dewald, T. R. Dittrich, T. Doppner, D. E. Hinkel, L. F. B. Hopkins, S. L. Paper, T. Ma, P. K. Patel, B. A. Remington, H. F. Robey, and J. D. Salmonson, Physical Review Letters **112**, 055001 (2014).

[11]Y. T. Lee and R. M. More, Physics of Fluids **27**, 1273 (1984).

[12]C. Orban, M. Fatenejad, S. Chawla, S. C. Wilks, and D. Q. Lamb, ArXiv e-prints (2013), arXiv:1306.1584 [physics.plasm-ph].

[13]J. Melvin, H. Lim, V. Rana, B. Cheng, J. Glimm, D. H. Sharp, and D. C. Wilson, "Sensitivity of ICF hot spot properties to the DT fuel adiabat," Report LA-UR-14-24815 (Los Alamos National Laboratory, 2014).

[14]H. Takabe, L. Montierth, and R. L. Morse, Physics of Fluids **26**, 2299 (1983).

[15]J. Sanz, J. Garrier, C. Cherfils, B. Canaud, L. Masse, and M. Temporal, Phys of Plasmas **12**, 112702 (2005).

[16]J. W. Bates, D. A. Knoll, W. J. Rider, R. B. Lowrie, and V. A. Mousseau, J. Comp. Phys. **167**, 99 (2001).

[17]R. B. Lowrie and J. E. Morel, J. Quantitative Spectrocopy and Radiative Transfer **69**, 475 (2001).

[18]C. Cerjan, P. T. Springer, and S. M. Sepke, Physics of Plasmas **20**, 056319 (2013).

[19]X.-F. Liu, Y.-H. Li, J. Glimm, and X.-L. Li, J. Comput. Phys. **222**, 644 (2007).

[20]X.-F. Liu, E. George, W. Bo, and J. Glimm, Phys. Rev. E **73**, 056301 (2006).

[21]H. Lim, J. Iwerks, J. Glimm, and D. H. Sharp, Proc. Nat. Acad. Sci. **107(29)**, 12786 (2010).

[22]H. Lim, J. Iwerks, Y. Yu, J. Glimm, and D. H. Sharp, Physica Scripta **T142**, 014014 (2010).

[23]N. Mueschke and O. Schilling, Physics of Fluids **21**, 014106 1 (2009).

[24]J. Glimm, D. H. Sharp, T. Kaman, and H. Lim, Phil. Trans. R. Soc. A **371**, 20120183 (2013).

[25]B. Cheng, J. Glimm, and D. H. Sharp, Chaos **12**, 267 (2002).

[26]V. S. Smeeton and D. L. Youngs, "Experimental investigation of turbulent mixing by Rayleigh-Taylor instability (part 3)," AWE Report Number 0 35/87 (1987).

[27]N. Mueschke, M. Andrews, and O. Schilling, J. Fluid Mech. **567**, 27 (2006).

[28]P. Ramaprabhu and M. Andrews, J. Fluid Mech. **502**, 233 (2004).

[29]B. Cheng, J. Glimm, and D. H. Sharp, Phys. Lett. A **268**, 366 (2000).

[30]E. George and J. Glimm, Physics of Fluids **17**, 1 (2005).

[31]J. Melvin, P. Rao, R. Kaufman, H. Lim, Y. Yu, J. Glimm, and D. H. Sharp, High Energy Density Physics **9**, 288 (2013).

[32]J. Melvin, P. Rao, R. Kaufman, H. Lim, Y. Yu, J. Glimm, and D. H. Sharp, ASME

Journal of Fluids Engineering **In Press** (2013).

[33]O. A. Hurricane, D. A. Callahan, D. T. Casey, P. M. Celliers, C. Cerjan, E. L. Dewald, T. R. Dittrich, T. Dppner, D. E. Hinkel, L. F. B. Hopkins, J. L. Kline, S. L. Pape, T. Ma, A. G. MacPhee, J. L. Milovich, A. Pak, H.-S. Park, P. K. Patel, B. A. Remington, J. D. Salmonson, P. Springer, and R. Tommasini, Nature **506**, 343 (2014).

Appendix C

Mixing with applications to ICF implosions [Physical Review E, Accepted]

Mixing with applications to ICF implosions

V. Rana, H. Lim, J. Melvin, and J. Glimm

Department of Applied Mathematics and Statistics,

Stony Brook University, Stony Brook, NY 11794-3600, USA

B. Cheng and D. H. Sharp

Los Alamos National Laboratory, Los Alamos, NM 87545, USA

Abstract

Approximate 1D as well as 2D and 3D simulations are playing an important supporting role in the design and analysis of future experiments at NIF. This paper is mainly concerned with 1D simulations, used extensively in design and optimization. We couple a 1D buoyancy-drag mix model for the mixing zone edges with a 1D ICF simulation code. This analysis predicts that National Ignition Campaign designs are located close to a performance cliff, so that modeling errors, design features (fill tube and tent) and additional, unmodeled instabilities could lead to significant levels of mix. The performance cliff we identify is associated with multimode CH mix into the hot spot DT. The buoyancy-drag mix model is mode number independent, and selects implicitly a range of maximum growth modes.

Our main conclusion is that single effect instabilities are predicted not to lead to hot spot mix, while combined mode mixing effects are predicted to affect hot spot thermodynamics and possibly hot spot mix. Combined with the stagnation Rayleigh-Taylor instability, we find the potential for mix effects in combination with the ice/gas DT boundary, numerical effects of Eulerian species CH concentration diffusion and ablation driven instabilities.

With the help of a convenient package of plasma transport parameters developed here, we give an approximate determination of these quantities in the regime relevant to the NIC experiments, while ruling out a veriety of mix possibilities. Plasma transport parameters affect the 1D buoyancy-drag mix model primarily through its phenomenological drag coefficient as well as the 1D hydro model the buoyance-drag equation is coupled to.

I. INTRODUCTION

The purpose of this paper is to examine Rayleigh-Taylor (RT) and Richtmyer-Meshkov (RM) mixing in NIC fusion capsules in terms of their overall instability growth rates. We couple a a 1D buoyancy-drag mix model for the mixing zone edges to a 1D ICF simulation code. The main prediction indicates that the NIC designs are located near a performance cliff – a conclusion which appears to be consistent with NIF/NIC experimental data.

We analyze several single cause instability mechanisms and find that the design is stable relative to these effects, but we find that combined mechanisms are more dangerous, and have a potential to degrade the performance of NIF fusion capsules.

Input to this analysis is a systematic study of plasma transport parameters, covering the NIC implosion range. In more detail, we find

1. No multimode CH mix into the NIC hot spot from the RM and stagnation RT instabilities. No significant role is found for concentration diffusion.

2. Severe mesh requirements for Eulerian simulations to avoid spurious CH mix into the cold shell.

3. Possible mix of CH into the hot spot from a combination of the RT stagnation instability and laser drive inhomogeneities. Other combined mechanisms may also degrade the NIC performance, especially the temperature of the hot spot at bang time.

Simulations in 1D, 2D as well as 3D are playing an important role in the design and analysis of future experiments at NIF. We concentrate in this paper on 1D simulations, widely used for design and optimization, augmented with an easy to use 1D mix model for the mixing zone edges. Simulations in any number of space dimensions will be facilitated and improved with a convenient package of plasma transport parameters, introduced here, that covers the NIC experiments discussed in this paper.

Mix is sensitive to transport parameters; a reasonably accurate determination of their values reduces model uncertainty. Remaining uncertainties concern a mixing model drag coefficient extrapolated beyond its presently validated limits to the highly variable and low Schmidt number ICF regime, and the influence of spherical geometry. 2D simulations, independent of the mix model, provide a level of confirmation for our conclusions.

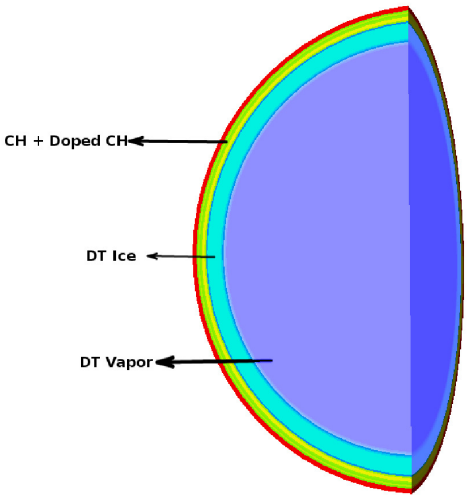

FIG. 1: The three principal layers of an ICF capsule.

In Sec. II, we summarize aspects of the theory of mixing important for the present paper. In Sec III we analyze the dimensionless Schmidt (Sc) and Prandtl (Pr) numbers,

$$Sc = \frac{\text{viscous diffusivity}}{\text{concentration diffusivity}} \; ; \quad Pr = \frac{\text{viscous diffusivity}}{\text{thermal diffusivity}} \; . \tag{1}$$

These ionic level transport parameters are major determinants of concentration and thermal mixing (whether due to turbulent or non turbulent stirring) of the fluids.

In Sec. IV, we analyze 3D instabilities using 1D simulations. We start with a diffusion model applied to the RM instabilities (of unknown initial amplitude in our analysis, as we do not model the ablation phase of the implosion). If the diffusion (physical or numerical) is sufficiently strong, in combination with the initial amplitude perturbations, the mixing crosses an RT stagnation instability threshold and becomes highly unstable. We confirm that this scenario cannot occur on the basis of physical mass diffusion, but it is possible through numerical diffusion based on Eulerian calculations, for all but exceedingly fine grids. It is also possible due to combined effect instabilities with strong RM initial perturbations or for ablation induced instabilities.

The 1D simulations, using the ICF code HYDRA [1] and the HEDP code FLASH [2] pertain only to the fuel capsule, described in [3, 4]. 2D simulations, given in Sec. V, support the mix analysis of Sec. IV. Conclusions are discussed in Sec. VI.

TABLE I: Table of Acronyms Used in this Paper

API	Application Programming Interface
AWE	Atomic Weapons Establishment
CDF	Cumulative Distribution Function
CH	Carbon/Hydrogen (ablator)
DNS	Direct Numerical Simulation
DT	Deuterium/Tritium
FLASH	University of Chicago HEDP code
FT	Front Tracking
HEDP	High Energy Density Physics
HYDRA	LLNL ICF code
ICF	Inertial Confinement Fusion
IPD	Ionization Potential Depression
LEM	Linear Electric Motor
LES	Large Eddy Simulation
LCLS	Linac Coherent Light Source
NIC	National Ignition Campaign
NIF	National Ignition Facility
OCP	One Component Plasma
OFMD	Orbital Free Molecular Dynamics
PAMD	Pseudo Atomic Molecular Dynamics
PDF	Probability Density Function
Pr	Prandtl numbr
RAGE	LANL multiphysics code
RANS	Reynolds Averaged Navier Stokes
RM	Richtmyer-Meshkov
RT	Rayleigh-Taylor
Sc	Schmidt number
YOCP	Yukawa One Component Plasma

II. TRANSPORT AND MIX

The important scientific principles which govern mixing phenomena are – broadly speaking – transport, initial conditions, mode competition, dominant or single mode growth rates and multimode growth rates. In many cases, we see that parameters which characterize these phenomena are better understood for planar geometry mix, so that extrapolation to mix in spherical geometry introduces uncertainty into the analysis.

A. Transport

We note the importance of fluid transport for the study of mix. Three important sources of transport are

- molecular or ionic (physically generated),
- turbulent (numerically mesh generated from averages of nonlinear quantities),
- numerical (algorithmically generated).

Turbulent transport is based on subgrid scale models, according to a widely accepted dynamic theory [5–7]. It does not occur in the governing Navier-Stokes equation, nor in its solution at a DNS level of numerical resolution. It is needed for RANS and LES. Numerical transport should be eliminated to the extent possible and in any case should be kept lower than the total transport, because diffusion, once added to a simulation, cannot be removed. The required numerical technology, Front Tracking, has been successfully used for fluid mixing problems, and is now available in the form of an API for ease of insertion into physics codes. For use here, we have inserted it into FLASH.

In a series of papers [8–10], the authors and coworkers presented accurate simulation studies of the RT dimensionless mixing ra, validated against rocket rig and splitter plate experimental data.

$$\alpha = \text{mix penetration distance}/Agt^2 \tag{2}$$

with Atwood number A and acceleration g. See Table II.

We also mention some more detailed code comparisons. These include an RM comparison between RAGE and FronTier [18], and comparison of converged LES/Front Tracking

TABLE II: Comparison of simulation to experiment, for the RT growth rate α. Discrepancy refers to the comparison of results outside of uncertainty intervals, if any, as reported. We omit simulations in gross disagreement with experiment and also those which achieve one parameter agreement with experiment through tuning one adjustable parameter. We acknowledge that there may be other validated, parameter free RT simulations, of which we are unaware.

Ref.	Exp.	Sim. Ref.	α_{exp}	α_{sim}	Discrepancy
LES/SGS/FT					
[11]	#112	[8]	0.052	0.055	6%
[11]	#105	[9]	0.072	0.076 ± 0.004	0%
[11, 12]	10 exp.	[10]	0.055-0.077	0.066	0%
[13]	air-He	[14]	0.065-0.07	0.069	0%
[15]	hot-cold	[8, 9]	0.070 ± 0.011	0.075	0%
[16]	salt-fresh	[9]	0.085 ± 0.005	0.084	0%
DNS					
[15]	hot-cold	[15]	0.070 ± 0.011	~ 0.070	0%
Particle Methods					
[17]		[17]		0.06 ± 0.005	

simulations [19] of the second moment of the velocity and other fluid variables that have been measured in a laboratory RT experiment.

Our previous work addressed convergence issues for PDFs and CDFs [20, 21] with experimental validation in [19, 22, 23], relative to the hot-cold water splitter experiments [15]. We have also considered two-point statistical descriptions of RT and RM mixtures [24–26]. Simulation of second moments provides data for RANS simulations, but convergence criteria for second moments are more demanding of a simulation than are convergence criteria for mean quantities or overall mixing rates.

B. The Buoyancy-Drag Equation

Our analysis of RT mix and mixing zone edges in Sec. IV is based upon the variable acceleration buoyancy-drag equation [27–29],

$$(\rho_i + k_i\rho_{i'})\frac{dV_i}{dt} = (\rho_i - \rho_{i'})g(t) - (-1)^i\frac{C_i\rho_{i'}V_i^2}{|h_i|}, \quad i = 1, 2 \quad , \tag{3}$$

where the "added mass" coefficient k_i, and the drag coefficient C_i, are the model's phenomenological parameters, $i = 1 = b$ (bubble) and $i = 2 = s$ (spike), $V_i \equiv dh_i/dt$ is the velocity of the edge i of the mixing zone, with h_i the mixing zone height. Also ρ_1 and ρ_2 are the light and heavy fluid densities, and $i' = i + 1(mod 2)$ is the opposite index to i. This formula allows a unified treatment of bubble and spike growth rates for both Rayleigh-Taylor and Richtmyer-Meshkov instabilities [29]. Specifically the four parameters $\alpha_i, \theta_i,\ i = 1, 2$ characterizing Rayleigh-Taylor and Richtmyer-Meshkov bubble and spike asymptotic growth rates are not independent. Any three are determined by specification of the fourth. We take the remaining single free parameter as the RT bubble growth rate, which is given by the bubble merger multimode growth rate as an independent theory [30] in agreement with experimental data..

The form of the drag force reflects the assumption that the fluid infinitely far upstream of the bubble or spike is stagnant. We consider cylindrical bubbles and spikes with $k_i \sim 1$ and the drag coefficient given by

$$C_i = \frac{1/\alpha_i - (1 + (-1)^i A) - k_i(1 - (-1)^i A)}{2(1 - (-1)^i A)}, \tag{4}$$

where α_i is the RT growth rate. For given α_b, the growth rate of spikes (α_s) can be obtained by assuming a stationary center of mass of the mixing layer [29]. The results, with the choice $k_i \sim 1$, are in good agreement with the Linear Electric Motors (LEM) experiment data [29, 31, 32], as shown in Fig. 2 taken from [29], with additional validation data to be found in [29]. In using (3), we start at a specified location in the cold shell at the beginning of the deceleration phase. We refer to this point as the Lagrangian point. It is then followed with Lagrangian dynamics. Eq. (3) yields equations for the associated RT bubble and spike tips. The acceleration is determined as a time derivative of the velocity interpolated to the Lagrangian point and the Atwood number is determined locally from the density variation over a region approximately bounding the bubble and spike tips.

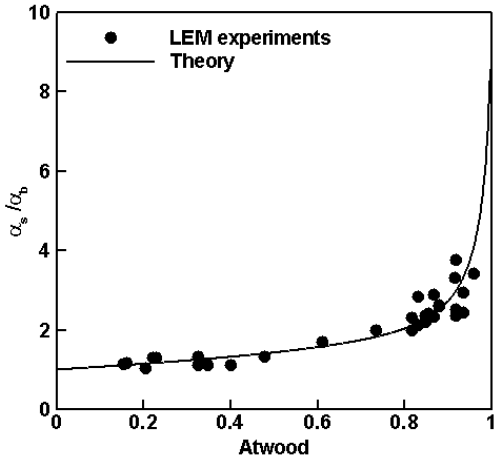

FIG. 2: The ratio of α_s/α_b as a function of Atwood number is shown for $\alpha_b \sim 0.05$. The solid dots are data from LEM experiments [32] and the solid curve is data from the model in [29].

We conclude that RT and RM instability growth rates are well understood, both theoretically and numerically (see Table II), but for planar geometry only. This knowledge is subsumed in the buoyancy-drag equation. As we apply this theory to determine the drag coefficient in the buoyancy-drag equation, we encounter extrapolation of the RT bubble growth rate beyond its validation range, a source of uncertainty for our analysis.

III. TRANSPORT PARAMETERS

A. The Transport Package TICF

Fluid mixing depends on fluid transport. In this section we discuss ionic or molecular level transport in a plasma as a contributor to the total fluid transport.

As noted [33], the large hot spot viscosity leads to a sharply reduced hot spot Reynolds number. The Reynolds number, depending on velocity fluctuations, is estimated as $10^0 - 10^2$ for the hot spot and $10^4 - 10^5$ for the cold shell [33].

The same plasma properties affect the thermal conductivity and species concentration diffusivity, with the result that for the hot spot $Pr \leq \mathcal{O}(10^{-1})$ and $\mathcal{O}(10^{-1}) \leq Sc \leq \mathcal{O}(1)$. The large variation in Sc is due to its dependence on the relative concentration χ of the CH

and DT ions,

$$\chi = \frac{i_{CH}}{i_{CH} + i_{DT}}, \tag{5}$$

where i_{CH} and i_{DT} are the respective ion number densities.

Both the viscosity and the species diffusion are strongly influenced by charge screening, which replaces the long range Coulomb interaction with a short range exponentially decaying interaction potential. The screening length depends on the density of electrons. This in turn is influenced by the species concentrations, as the DT has fewer electrons to ionize than does CH. In contrast, the (colder, denser) cold shell viscosity is smaller.

We introduce a package of molecular level viscosity, concentration diffusion and thermal transport parameters, summarized in Table III, and building on prior work [34–38] for the NIC parameter regime. The package is a composite of existing models and model switching criteria, with the switching criteria respecting the limits of model validity. The switching criteria are defined in terms of the degeneracy parameter Θ and the plasma parameter Γ introduced below. Our transport package, which we call TICF, covers the entire domain relevant to ICF experiments. In this sense it appears to go beyond other currently published transport packages [39]. It is available from the URL `www.ams.sunysb.edu/TICF`, and has been installed into the FLASH code.

The degeneracy parameter Θ, the ratio of electron to Fermi energies, determines the plasma state, as a classical plasma ($\Theta > 1$), or degenerate plasma ($\Theta < 1$). Specifically,

$$\Theta = \frac{k_B \cdot T_{ele}}{E_f} \ , \tag{6}$$

where E_f is the Fermi energy, k_B is the Boltzmann constant and T_{ele} is the electron temperature.

The plasma parameter Γ is the ratio of (Coulomb) potential energy to plasma kinetic energy. It measures the strength of the electron-ion coupling within the plasma [40]. For $\Gamma < 1$ the plasma is weakly coupled and for $\Gamma > 1$ it is strongly coupled. Γ is defined as

$$\Gamma = \frac{Z^{*2} q_{\rm ele}^2}{a \cdot T_{\rm ion} \cdot k_B} \ , \tag{7}$$

where $T_{\rm ion}$ is the ion temperature, $Z^* \cdot q_{\rm ele}$ is the species charge and

$$a = \left(\frac{3}{4 \cdot \pi \cdot n_{ion}} \right)^{\frac{1}{3}} \tag{8}$$

is the average inter-particle distance. Here n_{ion} is the number density of the ions. The Coulomb potential, whose value at separation a is ${}^{Z^{*2}\cdot q_{\text{ele}}^2}/_{a}$, governs the interactions between the ions. We model the non-ideal, strongly coupled plasma with One-Component Plasma (OCP) and Yukawa One-Component Plasma (YOCP) based viscosity models. Screening is modeled by a Yukawa OCP, with a dimensionless inverse screening length [35]

$$\kappa = a \cdot \frac{\sqrt{4 \cdot \pi \cdot Z^* \cdot n_{ion} \cdot q_{ele}^2}}{\sqrt{\left(k_B \cdot T_{ele}\right)^2 + \left(\frac{2}{3} \cdot E_f\right)^2}} \ , \tag{9}$$

dimensionalized in terms of the ionic radius a. The OCP is the limiting case of YOCP with an infinite screening length, $\kappa \to 0$. For the HYDRA simulation we are analyzing, $0 < \kappa < 4$.

If $\Theta \approx 1$ and $\Gamma \approx 1$, the plasma describes warm dense matter. When the plasma is weakly coupled, $\Gamma < 1$, it can be described as an ideal gas because the potential energy of the electrons is small compared to the average plasma kinetic energy. In this regime, we rely on the Braginskii approximation [34] for the kinematic viscosity when the plasma is fully ionized. The viscosity of the $\Gamma > 1$ plasma is computed by either the Yukawa viscosity model or the Bastea model [36], with a transition point depending on the plasma degeneracy Θ. Since the YOCP based viscosity model provides a fit for liquid metal and warm dense matter regime, we use this only when $0 < \Theta < 1$. During the Richtmyer-Meshkov instability, the matter is characterized by warm dense properties. The pure OCP Bastea model does not incorporate degeneracy effects, is not mapped to any special physical regime and is used when $\Theta > 1$.

Multicomponent transport models are required for mixtures. We regard CH and DT as single entities and apply mixture models to these entities. The ionization level Z^* is computed using More's parameterization [41] of Thomas-Fermi pseudo-ionization. We use A_{CH}, the average atomic weight of the C_2H_3 molecule as given in [42], to model the CH material. The effective ionization Z_{eff} for binary mixtures is computed using the binary ionic mixture model [43],

$$Z_{eff}^2 = \langle Z^* \rangle_{av}^{\frac{1}{3}} \langle Z^{*\frac{5}{3}} \rangle_{av} \ , \tag{10}$$

where $\langle Z^{*p} \rangle_{av} = x_1 \cdot Z_1^{*p} + x_2 \cdot Z_2^{*p}$ with x_i the number concentration and Z_i^* the Thomas-Fermi ionization associated with element i.

Recently, a new framework called pseudo-atom molecular dynamics (PAMD) was developed [44] to study dynamic structure in the warm dense matter regime. The dynamical

structure factor contains information about the temporal and spatial correlations in the system and is experimentally observable. From the dynamic structure we can extract information regarding the acoustic speed and other quantities. The dynamic structure factor for warm dense aluminum given by the PAMD framework [44] has been compared with that given by the orbital-free framework [45]. The comparisons were performed up to 5 eV since the pseudo-potential used in the orbital-free calculations in [45] scales up to 5 eV. There are discrepancies between the two models at 5 eV.

Currently we use Orbital Free Molecular Dynamics (OFMD) based diffusion models as opposed to PAMD based diffusion models because they scale to the higher temperature regimes needed for ICF applications, while PAMD based simulations must consider comparisons at pseudo-potentials at higher temperatures. A direct comparison of the PAMD based Thomas-Fermi fit and OFMD is provided in [46]. Excellent agreement between these two models is found for large ranges of temperature and pressure. We therefore believe that the enhanced PAMD based on a Kohn-Sham or Thomas-Fermi approximation versus that of OFMD would give slight improvement over the current results.

The concentration diffusion model starts with the self diffusion parameter of each species, from which the mutual diffusion parameter is derived [37, 47]. When the plasma is weakly coupled, the species diffusion parameter is determined via the Chapman-Spitzer approximation. Otherwise, we use the Cage model. In both cases, the models presented in [37, 47] are enhanced to include screening.

We model thermal conduction using the Lee-More model [38]. The CH/DT mixture depends on an average atomic weight. The model includes screening when computing the Coulomb forces, and is also applicable when the plasma exhibits degeneracy and strong ion coupling effects. The viscous and mass diffusion properties of CH/DT mixtures are derived from molecular dynamics simulations [35–37]. Given the empirical nature of the model and the possible influence of not using a MD based thermal conduction model, the present results can only be regarded as contributing to the scientific understanding of the method. RT instability growth rates are only weakly sensitive to uncertainty in the transport parameters. From [8, 48] we infer a 3% effect in the value of the RT growth rate coefficient α from a factor of 2 modification in the transport, which is well within the margin of error of the numerical simulations themselves for this variation in the transport parameters.

TABLE III: Transport models used to model CH/DT mixtures in an ICF capsule implosion.

Variable	Model	Γ	Θ	Summary
Viscous Diffusion	Braginskii [34]	$\Gamma < 1$		Braginskii model for weakly coupled hot, diffusive plasmas
Viscous Diffusion	Yukawa OCP[35]	$\Gamma > 1$	$0 < \Theta < 1$	Yukawa model for screened systems
Viscous Diffusion	OCP [36]	$\Gamma > 1$	$\Theta \geq 1$	Model based on one component plasma
Mass Diffusion	Chapman-Spitzer [37]	$\Gamma < 1$	$\Theta > 0$	Extends Chapman-Spitzer perturbation analysis with fit to screening
Mass Diffusion	Cage [37]	$\Gamma > 1$	$\Theta > 0$	Yukawa One-Component Plasma model with screening
Thermal Diffusion	Lee-More [38]			Classical thermal transport for ionized plasma

B. Transport Properties for NIC

In Figs. 3 and 4 we post-process a 1D post-shot HYDRA simulation, described in [3], using our transport package. We show concentration and thermal diffusion parameters, Sc and Pr respectively, which are of fundamental importance in understanding the extent or limits of RM and RT mixing. In the first of these figures, the concentration of CH is set to 0, while in the second it is set to 10%.

Sc and Pr show a strong dependence on the relative CH/DT concentration χ. See Figs. 5, 11, the latter in the supplementary material in the on-line version of this paper. Taking as typical hot spot temperature and density $T = 4.5\ keV$ and $\rho = 63\ g/cm^3$, we study Sc and Pr as functions of the relative CH vs. DT concentration χ. The dependence of these parameters on χ results from their large electron density in the CH rich region, which accounts for an increase in the screening length, resulting in smaller Sc and Pr values, see Fig. 5. A similar concentration dependence occurs during the RM stage, see Fig. 11, in the Appendix, available on-line. The non-monotone dependence of Sc on concentration is not a consequence of switching between models. This region lies entirely within the scope

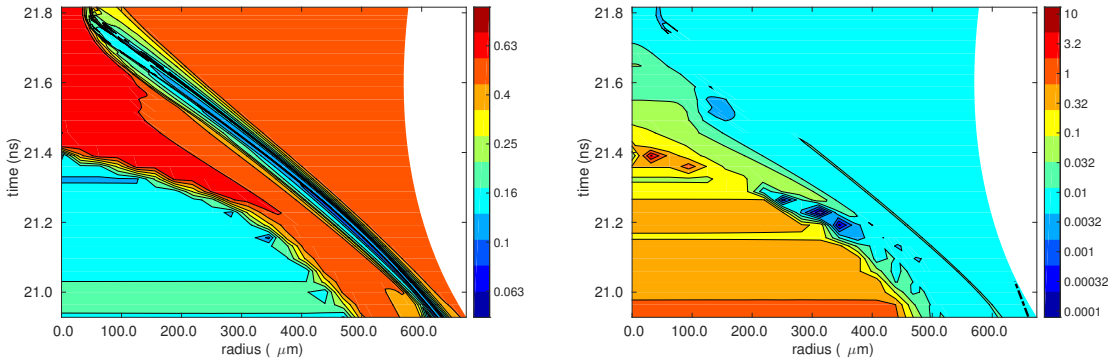

FIG. 3: RT phase of an ICF implosion in an r, t plot for the diffusion of the ablator into DT, Sc (left) and Pr (right) from a HYDRA simulation. From the left frame, we see that significant ablator into DT RT instabilities are allowed by the values of the transport parameters. From the right frame, we see that RT instabilities generated by thermally induced density gradients are regulated by the high levels of thermal conduction. The outer radius shown is outside the CH-DT interface.

of the Bastea model. It is rather a direct consequence of the Bastea OCP model itself, due to competing and opposite effects resulting from increased CH concentration. Among the multiple thermodynamics effects, we isolate what appear to be primary drivers. The increase in Sc for concentration in the interval [0.0,0.05] results from the increased proportion of heavy ions (which diffuse less rapidly). The decrease in Sc over the concentration interval [0.05,1], in contrast, is also driven by an increasing fraction of CH, which increases the electron density, thus increasing the screening length and lowering the viscosity. In any case, the screening effects of the plasma have a characteristic length scale of $[0.3, 0.6]$ $\mathring{A}$ in the hot spot, which implies that the hot spot plasma is weakly screened and as a result the dimensionless transport parameters become independent of screening at bang time.

The variation of Sc has hydrodynamical, mixing and possible numerical significance. The larger values of Sc at high DT concentration suggest a novel RT mixing behavior. The authors are not aware of scientific studies of mixing in which the concentration diffusivity and Schmidt number has such a striking dependence on the concentration. We suggest as a possible consequence that the RT spike and bubble will have well defined outer boundaries, but will still allow significant DT diffusion interior to the spike. We would suggest an

RT bubble growth rate of perhaps $\alpha = 0.06$, in lieu of more detailed scientific analysis, not presently available, and with α spike values coming from the theoretical relations of [29]. For less than DNS resolution, the values of Sc also suggest a role for a front tracking simulation [19, 49], to avoid excess numerical concentration diffusion.

In dense plasmas, free electrons orbit in close vicinity of ions. Therefore, the ions are no longer isolated. The screening induced from the dense environment skews their atomic energy levels, which in turn causes ionization potential depression (IPD). IPD is a key factor for understanding the ionization balance, charge state distribution, opacity and plasma equation of state. IPD occurs when a neighboring charged particle disrupts the ionic potential of an ion immersed in a plasma. IPD can be seen in two limits, the Debye shielding model and the ion sphere model (IS). The Debye shielding model holds when the plasma is in a weakly coupled regime, where the Debye length is greater than the inter-particle spacing. In high energy density plasmas, the number of particles in a Debye sphere are considerably lower, and instead we use the ion sphere model.

The IPD has been formulated in two ways. Stewart and Pyatt (SP) [50] solve for the IPD by calculating the electrostatic potential of the charged particles within the framework of the Thomas-Fermi theory. Ecker-Kroll (EK) [51] developed a generalized form of the Saha equation, based on the plasma chemical potential.

The SP/IS models are favored over the EK models in Orion Laser experiments performed at AWE [52], but the reverse is true for experiments at LCLS [53]. The experiments show that the IPD depends on the temperature and density, which are different between the two experiments, but a detailed analysis of the discrepancy is still lacking.. We believe that the IPD for our ICF simulation falls somewhere in between the SP and EK models with the choice treated as domain specific.

IV. MIX MODELS AND MIXING ZONE EDGES

We state our main results in this section, based on 1D simulations augmented by a buoyancy-drag mix model and confirmed by 2D simulations in Sec. V. We find

1. There is only a minor effect from concentration diffusion into the hot spot or the cold shell from the cold shell-gas T vs. D concentration discontinuity, or from the DT/CH boundary, based on the RM/RT stages of the implosion, see Fig. 6.

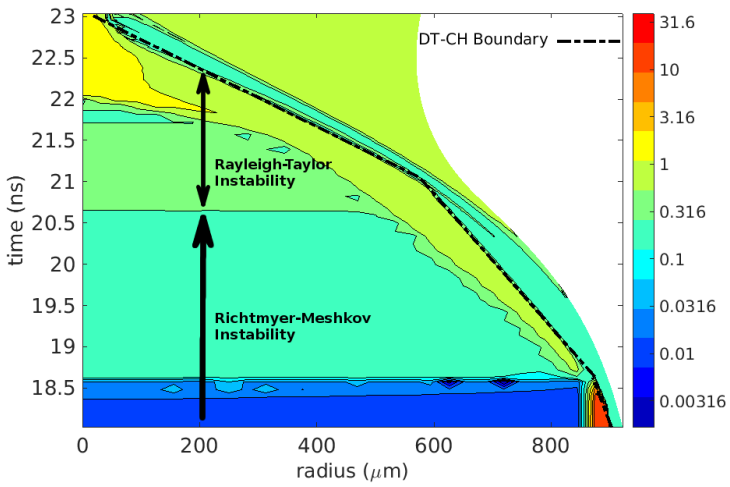

FIG. 4: Contour plot of Sc shown in the r, t space of a HYDRA simulation. The outer boundary of the plot includes approximately 1/3 of the ablator. The time (18 ns) starts shortly before the arrival of the fourth shock wave at the outer DT boundary. The black dashed line is the CH/DT boundary. The RM phase begins at 14.5 ns with the shock arrival at the CH/DT boundary (not shown in this figure). After the arrival of the 4th shock at this interface (18.5 ns), the CH/DT concentration χ becomes important. The plot assumes a 10% relative concentration of CH in the mixture and, at this value, Sc is large enough to allow significant DT-ablator mixing at both the RM and RT stages. If RM/RT spikes enter into the DT, diffusivity of the concentrations guarantees that all concentration values will occur as one passes through the spike from interior to exterior. 10% was chosen as an arbitrary value within this continuum of choices.

2. Untracked Eulerian simulations, at the resolution level of a finely gridded 3D simulation, show significant numerical effects, crossing an RT instability threshold, resulting in significant mixing of CH into DT in the cold shell. The effect is eliminated by Eulerian mesh refinement, by Lagrangian simulation codes, or by Front Tracking. The effect serves as a caution for the use of Eulerian codes for implosion problems. In the present context, approx 5000 cells (0.25 micron resolution) in the radial direction are needed to remove the numerical aspects of the simulation and to obtain a converged solution, with even qualitative agreement with the Lagrangian (HYDRA) or Front Tracking solutions. See Fig. 7. At higher levels of numerical diffusion, RM initial amplitudes or ablation induced instabilities, an effect on the hot spot thermal properties

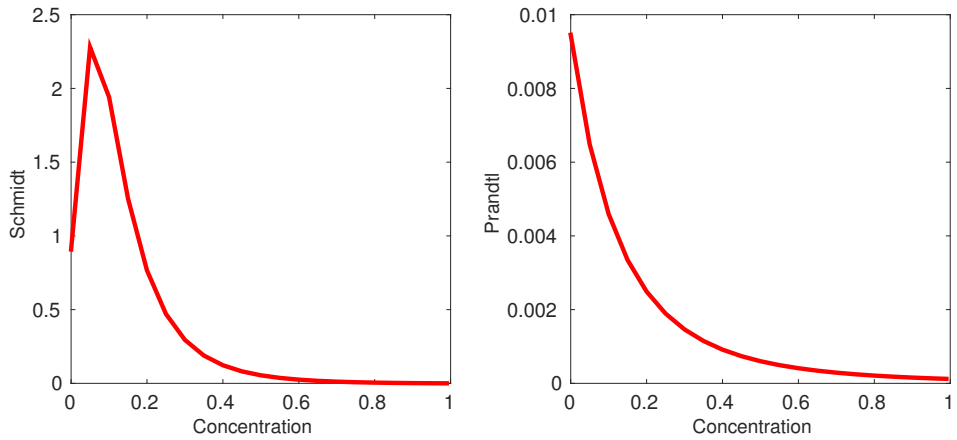

FIG. 5: The range Sc and Pr values as the concentration $\chi = \frac{i_{CH}}{i_{CH}+i_{DT}}$ is varied for fixed $T = 4.5keV$ and $\rho = 63\frac{g}{cm^3}$, typical values for the hot spot at bang time.

is possible. See Sec. V.

3. Combined effects of amplitude growth at the initial gas/ice boundary and the RT unstable thermal gradient at the edge of the hot spot adds a mix related component to the thermal diffusion, thereby reducing the size of the high temperature hot spot. See Sec. V.

4. Combined effect of ablation and RT instabilities appear to be a possible cause of CH mix into the hot spot. See Sec. V.

To establish these points, we conduct comparison 1D simulations, and repeated in 2D, in Sec. V. To assess the effects of numerical concentration diffusion, we simulate with and without front tracking, with various levels of (1D) mesh refinement and with and without physical concentration diffusion.

The ICF instabilities start at the ablation surface, with a modified RT instability, due to drive asymmetries and surface imperfections. Next in time are the cold shell RM instabilities associated with each of the ablator – DT ice and DT ice – DT vapor interfaces. In the case of "low-foot" or NIC shots, these instabilities are driven by each of four shock waves. We omit until later, discussion of the ablation instabilities that feed through to the RM initial amplitudes. Consequently, we set the RM initial conditions to those as measured on manufactured capsules. The importance of these is diminished by the nature of the

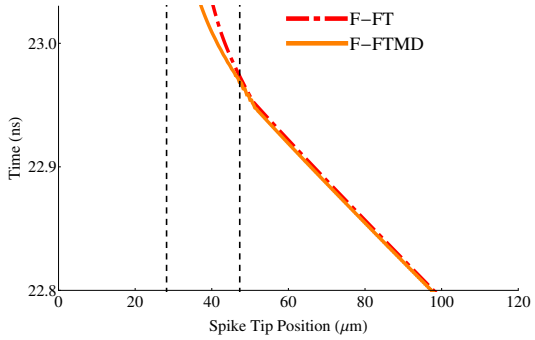

FIG. 6: We plot the inner radius of the CH spikes in r, t space of an NIC implosion for FLASH tracked simulations with (F-FTMD) and without (F-FT) physical mass diffusion. The spike tip location is assessed from the buoyancy drag equation associated with the 10% contour of CH. Only a minor effect from the addition of physical mass diffusion is observed at bang time, ≈ 23 ns. The inner and outer edges of the cold shell at bang time are demarcated on the plot with the dashed black lines.

RM evolution, which is in an RT stable (instability decreasing) regime. Thus we base our analysis of the RM phase not on the RM instabilities, but on diffusive transport occurring within this period.

Following the RM phase in time is the RT stagnation instability. The locus of RT instability, set by outgoing pressure waves reflected from the origin, is close to the unperturbed DT-CH boundary.

To establish point 1., we consider the inner radius of the spikes of CH in 1D simulations augmented by the buoyancy-drag mix model. We compare front tracked solutions in Fig. 6, showing the CH spike penetration in r, t space. The minor change between the two tracked solutions at bang-time, ≈ 23 ns, (having no numerical CH concentration diffusion), with and without physical diffusion shows the lack of importance of physical mass diffusion for NIC studies. To establish 2., we present a mesh refinement study in Fig. 7, plotting density vs. radius at bang time, with the medium mesh (0.25μm) needed to reach a nearly converged solution for the thermodynamics. Significant temperature differences arise from CH diffusion into the hotspot, especially in the presence of strong RM initial conditions, See Fig. 9.

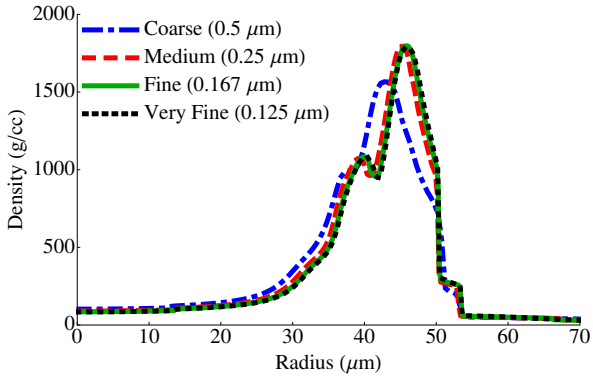

FIG. 7: A mesh convergence study for an untracked Eulerian simulation, showing density vs. radius at bang time. The nonconverged solutions have incorrect thermodynamics within the cold shell, see Sec. V, Fig, 8, but do not impact the hot spot thermodynamics.

V. 2D SIMULATIONS

The purpose of this section is to confirm claims 1. and 2. of Sec. IV, to establish claim 3. and to discuss the basis for statement 4.

Using the University of Chicago, HEDP code FLASH [2], we conduct 2D capsule-only simulations of NIC campaign shot N120321. As FLASH does not have as sophisticated a laser deposition and ablation package as HYDRA, we use the data from the 1D HYDRA run to initialize FLASH at 14.5ns, about 500 picoseconds before the first shock hits the fuel-ablator interface. A more complete analysis of these 2D simulations can be found in [54].

A. Absence of hot spot mix from instabilities arising at the DT/CH interface during the RT/RM implosion phases

We seed initial perturbations randomly into the fuel-ablator interface using spherical harmonics from mode 8 to 30, chosen to to reflect the level of mesh rolusion afforded in this study. These 2D simulations are designed to confirm the 1D simulations of Sec. IV. The initial rms amplitudes of the perturbations are chosen as 1 μm for the DT/CH interface and 1μm (nominal) and 5μm (strong) as a sensitivity study at the ice/gas interface.

The simulations show little growth of instability amplitude during the RM implosion

stage due to the RT stable nature of this implosion stage. During the RT stage, enhanced growth is observed in the strong initial perturbation case, but not sufficient enough to cause CH spikes to penetrate into the hotspot using the front tracked solution as a surrogate to the converged solution at bang time. See Fig. 8 bottom row, which shows both the nominal initial perturbation (left) and strong perturbation (right) CH concentrations that do not reach the hot spot. However, the combined effects of the coupling between the nearby perturbations at the initial ice/gas interface and steep thermal gradients at the edge of the hot spot, predicts a significant change in the hot spot thermodynamics, see Fig. 9 of Sec. V C.

B. Numerically induced RT/RM mixing

We find a potential for a significant level of numerically induced mix in the cold shell, for untracked Eulerian simulations with less than extremely refined grids. Comparing down the columns in Fig. 8, we show simulations with identical initial conditions, run at a resolution of 0.5μm using an untracked Eulerian configuration (top) and tracked Eulerian (bottom). The numerical diffusion present in the untracked simulations is amplified when the level of instability increases in the stronger initial perturbation (right column). The level of single effect RT/RM mixing is not sufficient to impact the hot spot thermodynamics, but combined effects are considered in Sec. V C.

C. Combined effects, gas/ice and thermal gradient RT instabilities

We observe a sensitivity to hot spot thermodynamics from a coupling effect between stronger perturbations at the ice/gas boundary and the strong thermal gradients at the hot spot edge. In Fig. 9, we show the hot spot density via the color plot and temperature contours (2keV and 5keV moving inward) for the nominal perturbation (left) and strong perturbation (right). The top half of each figure represents the 2D solution, which can be compared to the 1D solution in the bottom half of each frame. Both simulations are front tracked Eulerian, as representative of a converged solution, but only a minor sensitivity was observed between the front tracked and untracked solutions for the hot spot thermodynamics. The enhanced mixing reduces the temperature in the central hotspot with no 5 keV contour present in the

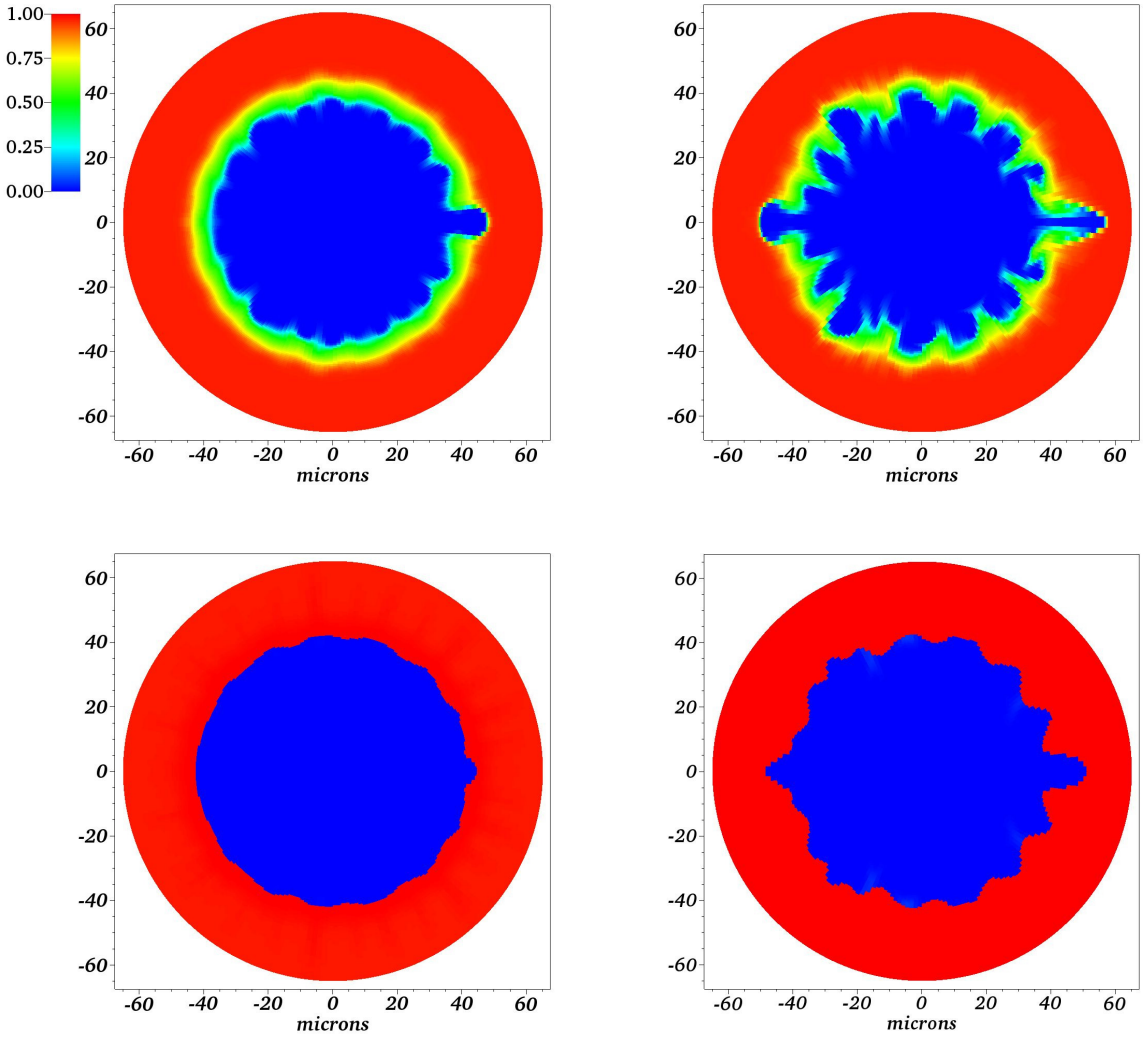

FIG. 8: CH spike edges at bang time for both nominal (left) and strong (right) RM initial conditions. When compared, the top row (without front tracking) and bottom row (with front tracking) show a large impact on the CH penetration due to numerical diffusion which interacts with the RT instability and is pulled inward. When comparing the nominal and strong initial conditions, a coupling effect between the larger perturbations and the growth of the instability at the thermal gradient, where the main potential for mixing occurs, is observed.

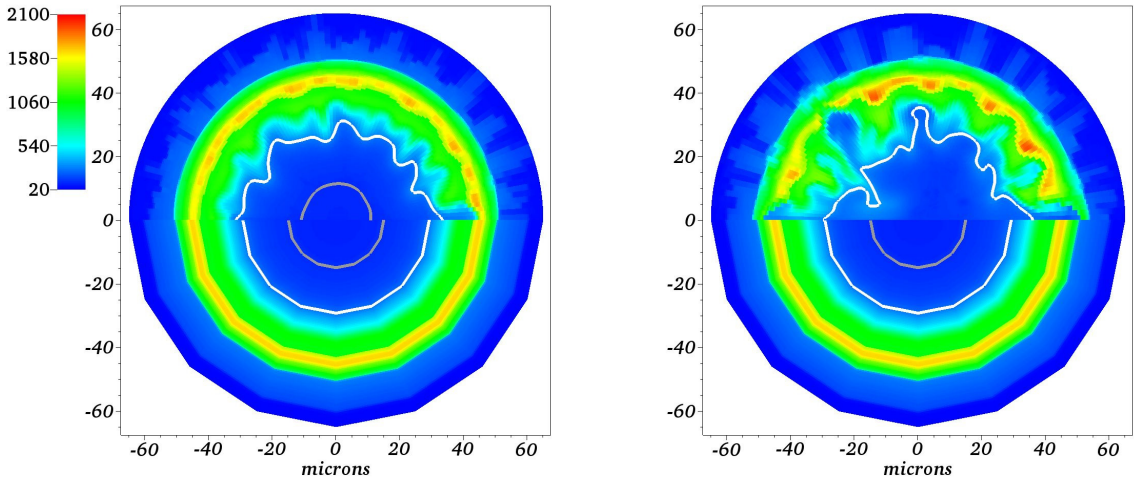

FIG. 9: Thermodynamics of the hotspot at bang time as observed through the density plots (color) and temperature contours (moving inwards 2keV and 5keV levels). Left: Front tracked Eulerian nominal initial perturbation. Right: Front tracked Eulerian strong initial perturbation. The top half of each frame is the 2D simulation compared with the bottom half from the companion 1D simulation. Enhanced mixing induced by the stronger initial perturbation results in the complete elimination of the 5keV contour and thus a lowering of the hot spot temperature, degrading the performance of the capsule.

right frame.

D. Combined effects: Ablation and DT/CH RT instabilities

According to post shot NIC simulations, 200ng (N120321) [55] or 50ng (N120321) [56] of CH is pre-mixed into the hot spot to capture the effects of ablator mix in the hot spot observed in the experiments, independent of the effects generated by the tent and fill tube [55]. Here we address the question of a physics based mechanism for this mix to occur.

Mode 2 instabilities of magnitude 8.3% and 15% have been reported for shots N120321, N120215, [57, 58]. The amplitude of mode number 6 and higher instabilities are not measured. The time dependent locus of RT instability (reversal of the direction of acceleration from inward to outward) lies inside the cold shell, and is near the CH boundary at the late implosion stages, with a radius beginning at $\approx$ 30% of the CH inner boundary radius at

the onset of the deceleration stage. As the deceleration phase progresses this RT instability locus moves towards the CH boundary as the pressure equilibrates from the outward moving stagnation shock. In Fig. 10 left, we plot the inner radius of the CH spike tips, as predicted by the 1D mix model analysis of a simulation started at the beginning of the RT deceleration phase. We show a range of perturbation amplitudes, measured as a fraction of the unperturbed CH radius. If the amplitude exceeds 10-15% of the DT radius at the initiation time for the RT instability, we observe spike tips penetrating into the hot spot.

To justify the use of the buoyancy-drag model for predictions of the CH spike penetration, in Fig. 10 right, we compare the predicted 3D mix from the model against the observed spike penetration from a companion 2D simulation. The simulation used for this comparison was the FLASH base simulation with a strong initial perturbation run from the beginning of the RM phase. The early increased amplitude in the simulation (solid blue line) is a result of the extra vorticity in the solution from the increased size of the perturbation, which is not present in a 1D model. As bang time is approached (23.1 ns for this simulation), the buoyancy drag model slightly overpredicts the growth allowing the lines to converge. Overall, the buoyancy-drag model has resaonably good agreement with the 2D spike penetration. This suggests that the model should be a resonable predictor of 3D mix and can be used for parameter studies based off of 1D simulations.

Based on the spike penetration observed for various perturbations amplitudes, it is possible that an ablation driven instability can push the CH across this critical RT unstable locus and onto a trajectory of inward directed spike development. Such an event is consistent with the experiments and analysis of [59], and moreover, we have a quantitative estimate of the amplitude needed to generate the instability, see Fig. 10 left. Current NIC simulations [60] focus on localized defects on the ablator outer surface as generating narrow CH spikes, which presumably couple to the RT unstable point, as analyzed in Fig. 10. See also the related experimental paper [61]

VI. DISCUSSION

Our proposed model indicates that the NIC design is located near a performance cliff, a conclusion consistent with NIF/NIC experimental data. We find no single mechanism mix related effects from the RM/RT implosion stages but possible effects from combined

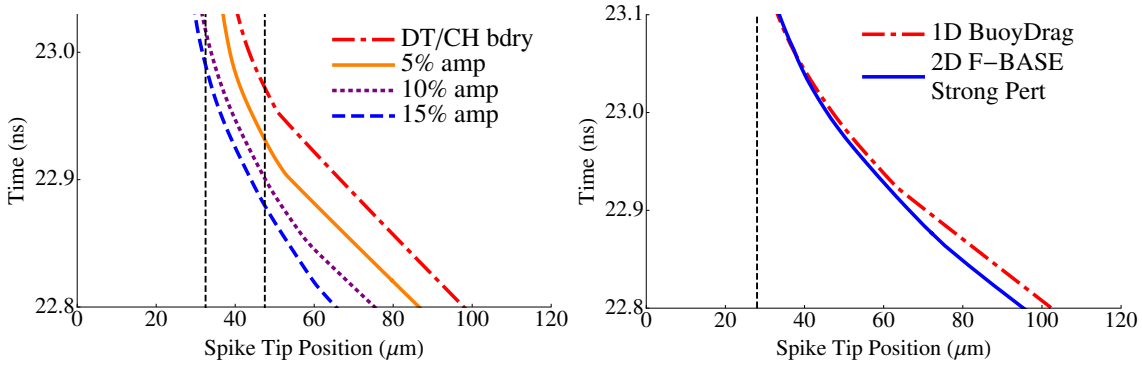

FIG. 10: Left: Penetration of the CH spike tips into the DT fuel at bang time, in an r, t plot, for a range of perturbation amplitudes, using a simulation iinitialized at the beginning of the RT stage. For amplitudes in excess of 10-15%, we observe penetration of spikes into the hot spot. The dotted black lines represent the edge of the hot spot and cold shell region at bang time ($\approx$ 23 ns), respectively. Right: Comparison of 1D buoyancy-drag model against 2D spike penetration from companion simulation initialized at the beginning of the RM stage. Reasonable agreement is observed between the buoyancy-drag model and the simulated spike penetration through bangtime ($\approx 23.1ns$), suggesting the model is a can be used for prediction of 3D mix.

mechanisms.

We find at most marginal effects from mass (CH/DT or D/T concentration) diffusion, but possible combined RM/RT mix related effects on the hot spot thermodynamics.

We find significant effects from numerical mass diffusion for Eulerian codes for all but the most extreme levels of mesh refinement. These effects are associated with the CH/DT interface, and have a possible (numerically induced) impact on the hot spot thermodynamics.

We discuss an ablation/RT combined effect which may lead to CH mix in the hot spot.

The basis for these results is a 1D mix model simulation for NIC experiments, based on buoyancy-drag equations. This equation, toether with its parameters have been extensively validated, but is used here outside of the validation regime, and for this purpose we propose estimates based on judgment and available knowledge. Additionally, the equation and its validation have been carried out for planar but not spherical geometry. Uncertainties in the mix model, as applied to NIC, include RM initial conditions, extrapolation of the model drag coefficient beyond their presently validated limits, and the effects of spherical geometry.

2D simulations are condiuucted using FLASH, and with fronnt tracking added via an API for convenience of code development. The 2D simulations confirm the 1D and mix model analysis of Sec. IV. Additionally, they identify combined effect mixing instabilities not idnetified by the 1D analysis. Specifically, we find coupling between instabilities at the ice-gas boundary and the RT stagnition instability, which lowers the hot spot temperature even eithout introducing CH into the hot spot.

In support of the mix model and the 2D simulations, we have determined parameterized plasma transport models, with model switching criteria, showing significant variation as the implosion progresses. The transport package is available to others and could aid future HED simulation studies.

Acknowledgments

This manuscript has been co-authored by Los Alamos National Laboratory, under Contract No. JL3K00 NYSB0000, Inertial Confinement Fusion Campaign. Los Alamos preprint LA-UR 16-20021. This research used resources of the National Energy Research Scientific Computing Center, which is supported by the Office of Science of the U. S. Department of Energy under Contract No. DF-AC02005CH11231. This research used computational resources of Lawrence Livermore National Laboratory. It is a pleasure the thank Lee Collins and Joel Kress for helpful comments.

---

[1] M. M. Marinak, G. D. Kerbel, N. A. Gentile, O. Jones, D. Munro, S. Pollaine, T. R. Dittrich, and S. W. Haan, Physics of Plasmas **8**, 2275 (2001).

[2] B. Fryxell, K. Olson, P. Ricker, F. X. Timmes, M. Zingale, D. Q. Lamb, P. MacNeice, R. Rosner, J. W. Truran, and H. Tufo, Astrophysical Journal ,Supplement **131**, 273 (2000).

[3] J. Melvin, H. Lim, V. Rana, B. Cheng, J. Glimm, D. H. Sharp, and D. C. Wilson, Physics of Plasmas **22**, 022708 (2015).

[4] J. Melvin, H. Lim, V. Rana, B. Cheng, J. Glimm, D. H. Sharp, and D. C. Wilson, Journal of Physical Science and Application **5**, 24 (2015).

[5] A. Honein and P. Moin, "Numerical aspects of compressible turbulence simulations," Report

No. TF-92 (Stanford Univ., 2005).

[6] P. Moin, K. Squires, W. Cabot, and S. Lee, Phys. Fluids A **3**, 2746 (1991).

[7] U. Piomelli, W. H. Cabor, P. Moin, and S. Lee, Phys. Fluids A **3**, 1766 (1991).

[8] H. Lim, J. Iwerks, J. Glimm, and D. H. Sharp, Proc. Natl. Acad. Sci. **107(29)**, 12786 (2010), Stony Brook University Preprint SUNYSB-AMS-09-05 and Los Alamos National Laboratory Preprint LA-UR 09-06333.

[9] J. Glimm, D. H. Sharp, T. Kaman, and H. Lim, Phil. Trans. R. Soc. A **371**, 20120183 (2013), Los Alamos National Laboratory Preprint LA-UR 11-00423 and Stony Brook University Preprint SUNYSB-AMS-11-01.

[10] E. George, J. Glimm, X.-L. Li, Y.-H. Li, and X.-F. Liu, Phys. Rev. E **73**, 016304 (2006).

[11] V. S. Smeeton and D. L. Youngs, "Experimental investigation of turbulent mixing by Rayleigh-Taylor instability (part 3)," AWE Report Number 0 35/87 (1987).

[12] K. I. Read, Physica D **12**, 45 (1984).

[13] P. Ramaprabhu and M. Andrews, J. Fluid Mech. **502**, 233 (2004).

[14] X.-F. Liu, E. George, W. Bo, and J. Glimm, Phys. Rev. E **73**, 056301 (2006).

[15] N. Mueschke and O. Schilling, Physics of Fluids **21**, 014106 1 (2009).

[16] N. J. Mueschke, *Experimental and numerical study of molecular mixing dynamics in Rayleigh-Taylor unstable flows*, Ph.D. thesis, Texas A and M University (2008).

[17] K. Kadau, T. C. Germann, N. G. Hadjiconstantinou, P. S. Lomdahl, G. Dimonte, B. L. Holian, and B. J. Alder, Proc. Natl. Acad. Sci. **101**, 5851 (2004).

[18] T. O. Masser, *The Effects of Temperature Equilibrium in Mixed Cell Hydrodynamics*, Ph.D. thesis, State University of New York at Stony Brook (2007).

[19] J. Glimm, W. Hu, H. Lim, B. Plohr, and D. H. Sharp, Ann. Math. Sci. and Applications **1**, 149 (2016), los Alamos Preprint LA-UR-12-26149. Stony Brook University Preprint Number SUNYSB-AMS-15-05.

[20] T. Kaman, R. Kaufman, J. Glimm, and D. H. Sharp, in *Uncertainty Quantification in Scientific Computing*, IFIP Advances in Information and Communication Technology, Vol. 377, edited by A. Dienstfrey and R. Boisvert (Springer, 2012) pp. 212–225, Stony Brook University Preprint number SUNYSB-AMS-11-08.

[21] J. Melvin, P. Rao, R. Kaufman, H. Lim, Y. Yu, J. Glimm, and D. H. Sharp, High Energy Density Physics **9**, 288 (2013), Stony Brook University Preprint SUNYSB-AMS-12-01 and Los

Alamos National Laboratory Preprint LA-UR 12-21555.

[22] P. Rao, J. Melvin, W. Hu, R. Kaufman, H. Lim, and J. Glimm, in *11th World Congress on Computational Mechanics (WCCM XI)* (2014) Stony Brook University Preprint SUNYSB-AMS-14-01.

[23] J. Glimm, D. H. Sharp, H. Lim, R. Kaufman, and W. Hu, Phil. Trans. R. Soc. A **373**, 20140282 (2015), Los Alamos National Laboratory Preprint LA-UR-14-29521 and Stony Brook University Preprint SUNYSB-AMS-14-04.

[24] J. Glimm, J. W. Grove, X.-L. Li, W. Oh, and D. H. Sharp, J. Comput. Phys. **169**, 652 (2001).

[25] H. Lim, Y. Yu, J. Glimm, X. L. Li, and D. H. Sharp, Physica Scripta **T142**, 014062 (2010), Stony Brook Preprint SUNYSB-AMS-08-07 and Los Alamos National Laboratory Preprint LA-UR 08-07725.

[26] H. Lim, Y. Yu, H. Jin, D. Kim, H. Lee, J. Glimm, X.-L. Li, and D. H. Sharp, Compu. Methods Appl. Mech. Engrg. **197**, 3435 (2008), Stony Brook University Preprint SUNYSB-AMS-07-05.

[27] G. Dimonte and M. Schneider, Phys. Fluids **12**, 304 (2000).

[28] D. Oron, O. Sadot, Y. Srebro, A. Rikanti, Y. Yedvab, U. Alon, L. Erez, G. Erez, G. Ben-Dor, L. A. Levin, D. Ofer, and D. Shvarts, Lasers and Particle Beams **17**, 465 (1999).

[29] B. Cheng, J. Glimm, and D. H. Sharp, Phys. Lett. A **268**, 366 (2000).

[30] B. Cheng, J. Glimm, and D. H. Sharp, Chaos **12**, 267 (2002).

[31] G. Dimonte and M. Schneider, Phys. Rev. E **54**, 3740 (1996).

[32] G. Dimonte, Phys. Plasmas **6**, 2009 (1999).

[33] C. R. Weber, D. S. Clark, D. Cook, L. E. Busby, and H. F. Robey, Phys Rev E **89**, 053106 (2014).

[34] H. F. Robey, Phys. of Plasmas **11**, 4123 (2004).

[35] M. S. Murillo, High Energy Density Physics **4**, 49 (2008).

[36] S. Bastea, Phys Rev E **71**, 056405 (2005).

[37] J. Daligault, Phys. Rev. E **86**, 047401 (2012).

[38] Y. T. Lee and R. M. More, Physics of Fluids (1958-1988) **27**, 1273 (1984).

[39] E. L. Vold, A. S. Joglekar, M. I. Ortega, R. Moll, D. Fenn, and K. Molvig, Physics of Plasmas **22** (2015).

[40] D. Salzmann, *Atomic Physics in Hot Plasmas* (Oxford University Press, Oxford, 1998).

[41] R. More, Advances in Atomic and Molecular Physics, **21**, 305 (1985).

[42] F. Lambert and V. Recoules, Phys. Rev. E **86**, 026405 (2012).

[43] J. P. Hansen, G. M. Torrie, and P. Vieillefosse, Phys. Rev. A **16**, 2153 (1977).

[44] N. M. Gill, R. A. Heinonen, C. E. Starrett, and D. Saumon, Phys. Rev. E **91**, 063109 (2015).

[45] T. G. White, S. Richardson, B. J. B. Crowley, L. K. Pattison, J. W. O. Harris, and G. Gregori, Phys. Rev. Lett. **111**, 175002 (2013).

[46] C. E. Starrett, J. Daligault, and D. Saumon, Phys. Rev. E **91**, 013104 (2015).

[47] J. Daligault, Phys. Rev. Lett. , 225004 (2012).

[48] H. Lim, J. Iwerks, Y. Yu, J. Glimm, and D. H. Sharp, Physica Scripta **T142**, 014014 (2010), Stony Brook University Preprint SUNYSB-AMS-09-07 and Los Alamos National Laboratory Preprint LA-UR 09-07240.

[49] R. Kaufman, H. Lim, and J. Glimm, Bulletin of the Institute of Mathematics, Academia Sinica New Series **11**, 115 (2016), stony Brook University Preprint SUNYSB-AMS-15-01.

[50] J. C. Stewart and J. Pyatt, Kedar D., The Astrophysical Journal **144**, 1203 (1966).

[51] G. Ecker and W. Krll, Physics of Fluids **6**, 62 (1963).

[52] D. J. Hoarty, P. Allan, S. F. James, C. R. D. Brown, L. M. R. Hobbs, M. P. Hill, J. W. O. Harris, J. Morton, M. G. Brookes, R. Shepherd, J. Dunn, H. Chen, E. Von Marley, P. Beiersdorfer, H. K. Chung, R. W. Lee, G. Brown, and J. Emig, Phys. Rev. Lett. **110**, 265003 (2013).

[53] O. Ciricosta, S. M. Vinko, H.-K. Chung, B.-I. Cho, C. R. D. Brown, T. Burian, J. Chalupský, K. Engelhorn, R. W. Falcone, C. Graves, V. Hájková, A. Higginbotham, L. Juha, J. Krzywinski, H. J. Lee, M. Messerschmidt, C. D. Murphy, Y. Ping, D. S. Rackstraw, A. Scherz, W. Schlotter, S. Toleikis, J. J. Turner, L. Vysin, T. Wang, B. Wu, U. Zastrau, D. Zhu, R. W. Lee, P. Heimann, B. Nagler, and J. S. Wark, Phys. Rev. Lett. **109**, 065002 (2012).

[54] J. Melvin, *Numerical Modeling of Hydrodynamic Instabilities and their Impact on Mix in Inertial Confinement Fusion*, Ph.d. thesis, Stony Brook University (2016).

[55] D. S. Clark, M. M. Marinak, C. R. Weber, D. C. Eder, S. W. Haan, B. A. Hammel, D. E. Hinkel, O. S. Jones, J. L. Milovich, P. K. Patel, H. F. Robey, J. D. Salmonson, S. M. Sepke, and C. A. Thomas, Physics of Plasmas **22** (2015).

[56] D. S. Clark, C. R. Weber, J. L. Milovich, J. D. Salmonson, A. L. K. andS. W. Haan, B. A. Hammel, O. A. Hurricane, O. S. Jones, M. M. Marinak, P. K. Patel, H. F. Robey, and S. M. Sepke, "High-resolution, detailed simulations of low foot and high foot implosion experiments

on the NIF," (2015), 57th Annual Meeting of the APS Division of Plasma Physics.

[57] D. S. Clark, D. E. Hinkel, D. C. Eder, O. S. Jones, S. W. Haan, B. A. Hammel, M. M. Marinak, J. L. Milovich, H. F. Robey, L. J. Suter, and R. P. J. Town, Physics of Plasmas **20**, 056318 (2013).

[58] C. Cerjan, P. T. Springer, and S. M. Sepke, Physics of Plasmas **20**, 056319 (2013).

[59] B. R. snd L. J. Atherton, L. R. Benedett, L. Berzak-Hopkins, D. K. Bradley, D. A. Callahan, D. T. Casey, P. M. Celliers, C. J. Cerjan, D. S. Clark, E. L. Dewald, T. R. DFittrich, S. N. Dixit, F. Doppner, D. H. Edgell, M. J. Edwards, R. Epstein, J. Frenje, M. Gatu-Johnson, S. Glenn, S. H. Glenzer, G. Grim, S. W. Haan, B. A. Hammel, A. Hamza, D. Hicks, W. W. Hsing, O. Hurricane, N. Izumi, O. S. Jones, M. H. Key, S. F. Khan, J. D. Kilkenny, G. A. Kyrala, O. L. Landen, S. LePape, J. D. Lindl, , T. Ma, B. J. MacGowen, A. J. Mackinnon, A. G. MacPhee, N. B. Meezan, J. D. Moody, E. I. Moses, A. Nikroo, A. Pak, T. Parham, H.-S. Park, P. K. Patel, R. Petrasso, J. Pino, J. E. Ralph, K. Raman, S. P. Regan, H. F. Robey, J. S. Ross, B. K. Spears, V. A. Smalyuk, P. T. Springer, I. J. Suter, R. Tipton, R. Tommasim, R. P. Town, and S. V. Weber, "Hydrodynamic instabilities and mix studies on nif: predictions, observations and a pathe forward," (2016).

[60] C. R. Weber, D. S. Clark, A. W. Cook, D. C. Eder, S. W. Haan, B. A. Hammel, D. E. Hinkel, O. S. Jones, M. M. Marinak, J. L. Milovich, P. K. Patel, H. F. Robey, J. D. Salmonson, S. M. Sepke, and C. A. Thomas, Physics of Plasmas **22**, 032702 (2015), http://dx.doi.org/10.1063/1.4914157.

[61] S. Mitchell and M. Vynnycky, Journal of Computational and Applied Mathematics **236**, 4181 (2012).

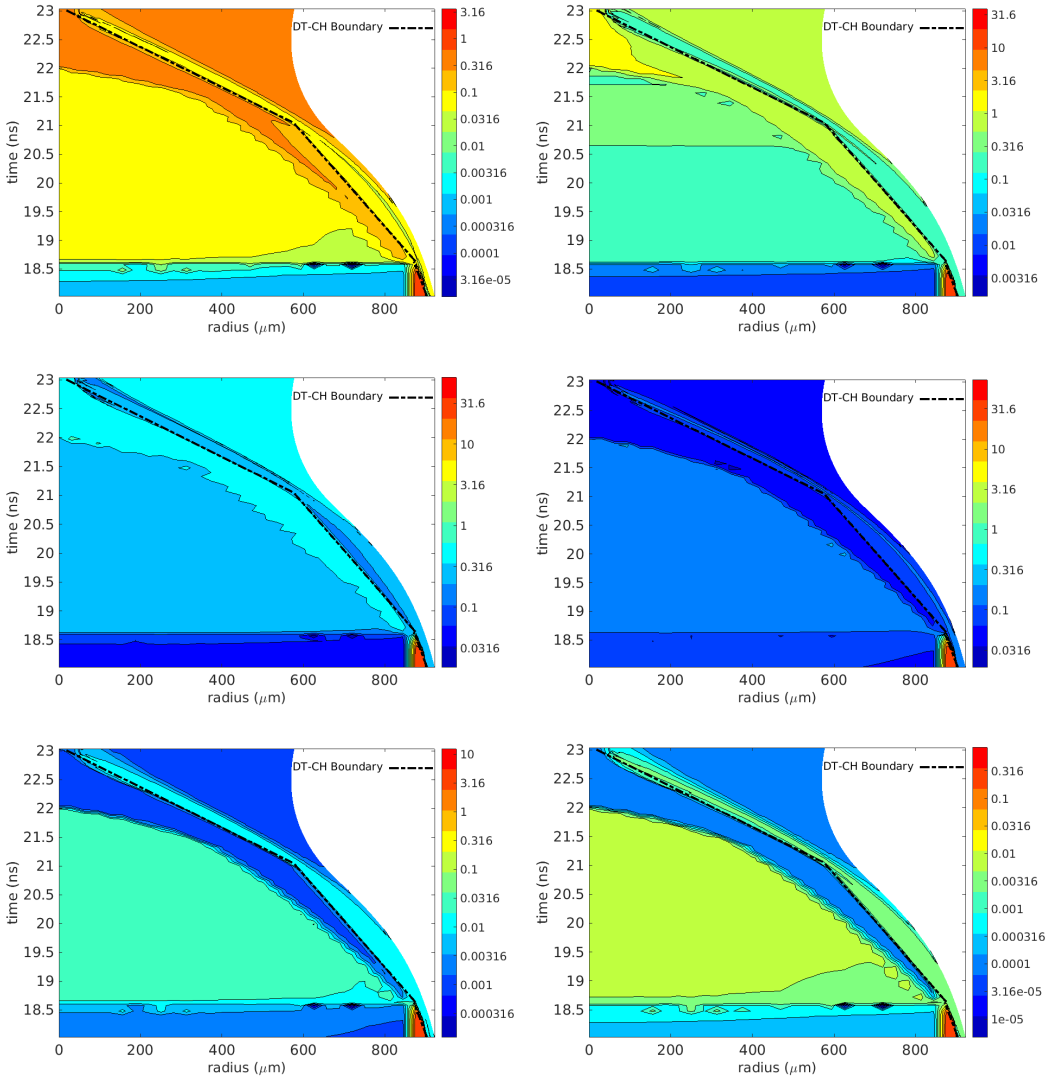

FIG. 11:

[aip,amsmath,amssymb,preprint,pop,floatfix]revtex4 graphicx The appendix to this paper is included as supplementary material in the on line version only.

APPENDIX A: CONCENTRATION DEPENDENT RM AND RT SCHMIDT NUMBERS

In Fig. 11, we plot Schmidt number in the r, t space of a NIC implosion, for a representative sequence of CH/DT relative concentrations.

Appendix D

The Influence Of Divots On The Thermodynamic Properties Of The Hotspot In Inertial Confinement Fusion Implosions [Publication Draft]

The Influence Of Divots On The Thermodynamic Properties Of The Hotspot In Inertial Confinement Fusion Implosions

V. Rana, J. Melvin, and J. Glimm
Department of Applied Mathematics and Statistics,
Stony Brook University, Stony Brook, NY 11794-3600, USA

B. Cheng and D. H. Sharp
Los Alamos National Laboratory, Los Alamos, NM 87545, USA

We study the effects of isolated surface defects (divots) on the inertial confinement hot spot thermodynamics. Radiographic measurements infer the presence of CH in the hot spot, beyond what is ascribed to the tent and fill tube in calibrated simulation models, and accordingly we focus on the CH location at bang time resulting from a divot. We find significant effects on the hot spot thermodynamics across multiple variations of the simulation parameters, however no CH is found to enter the hot spot. The physical diffusion coefficient emerges as an important valuable across all simulations considered here. Our study places the divots near or slightly beyond an instability cliff for entry into the hot spot but arriving there sufficiently late in time not to protrude into the hot spot. Large effects from the divot are observed on the location of the 4 keV hot spot ion temperature boundary. We also show that the divot penetration is sensitive to the numerical method, with strong differences between the tracked and the untracked, even though both are nominally converged. We identify the tracked solution as correct while the nominally converged but incorrect untracked solution raise issues for further thought.

The study is by simulation, starting at the stagnation Rayleigh-Taylor (RT) instability point and continues to bang time. We vary the divot amplitude and width, the numerical method (as it relates to numerical concentration diffusion), the physical concentration diffusion model and the refinement of the mesh. Our simulation platform, is based on the FLASH code, to which we have added options for plasma transport and for front tracking to reduce numerical concentration diffusion. Our methods are suitable for the analysis of the stagnation instability (of Rayleigh-Taylor type), and so we assume divot like perturbations of the implosion at the initiation of this stage, leaving to a separate study the creation of these perturbations from the ablation acceleration of the capsule, also a type of modified Rayleigh-Taylor unstable acceleration.

I. INTRODUCTION

Recent NIF experiments [1] provide insight into possible drivers that degrade the nuclear reactions. Identified are hydrodynamic instabilities, x-ray asymmetries, the capsule-support tent and the fill-tube [2], and the mix of ablator material into the hot spot [3]. In this paper, we examine the effect of a single localized surface defect (divot) which we postulate to result in a high mode number jet of CH protruding into the DT; we study its effect on the hot spot ignition environment. We define the hot spot as the interior of the unperturbed 4 keV temperature contour and bang time also taken from the unperturbed simulation. In [3] the ion temperature is decreased from individually modeling a single high mode divot when compared to a 1D simulation but still larger than the experimentally observed. The CH appears not to reach the hot spot. As our base case simulation, we include physical concentration diffusion and reduced numerical concentration diffusion (with front tracking). We vary the divot amplitude and width and the mesh resolution.

We study the low-foot shot N120321 [4], which was the highest compression shot of the NIC campaign. Excess CH in the hot spot for shot N120321 as estimated by radiographic data, beyond that inferred as due to the tent and fill tube was variously reported as 50 ng [5], 75 ng [5] and 200 ng [3]. For shot N120405, which differs in the strength of the laser, the excess CH, determined as above, is 750 ng [5]. The degraded performance of shot N120405 relative to shot N120321 occurs in many of the experimental quantities, and is hypothesized to result from a stronger laser [3].

Section II gives a brief description of the simulation platform including the Transport For Inertial Confinement Fusion (TICF) package and the Front Tracking Interface API (FTI), added to FLASH. Section III presents our main simulation results, with conclusions in Section IV

II. SIMULATION METHODOLOGY

The as manufactured surface of the capsule contains a number of defects of various sizes and shapes [6], commonly known as divots. To assess the impact of a divot on the hot spot thermodynamics, we perform 2D post shot

simulations (tuned to match VISAR[] and ConA[] data) using a wedge geometry of the ICF capsule based on the radiation hydrodynamics code FLASH [7]. A perturbation to model the divot effect is initialized at the north pole at the CH-DT interface in a 2D simulation geometry at the onset of the stagnation RT instability. The initial perturbation (divot) amplitude is specified as a fraction (per cent) of the cold shell. All simulations are performed in half wedge geometry but shown with the reflected full wedge geometry for clarity.

The simulations begin at 22.56 ns which is the time of maximum implosion velocity in our FLASH simulations. To generate the divot dynamics, we perturb the CH-DT boundary by a cylinder of CH penetrating into the DT. The perturbed divot length is expressed as a percent of the DT cold shell and its diameter express as a wave number (whose inverse is a fraction of 2π). The velocity perturbation is computed from the amplitude as the incremental velocity needed to achieve the perturbed amplitude after arrival of the fourth shock. We considered as a base case simulations with front tracking [8], physical concentration diffusion, an initial perturbation of 16% and a mesh of 1.7 μm in the radial direction. The effects [2, 9] from the fill-tube and tent are not included.

A. FLASH

FLASH is an Eulerian multi-physics radiation hydrodynamics code. We employ its Piecewise Parabolic Method (PPM) hydrodynamics solver. The hydrodynamics is based on a three temperature model using multi group radiation. We use 60 radiation energy groups logarithmically spaced in three bands: i) 25 groups from 30 eV to 1 keV, ii) 25 groups from 1 keV to 5 keV and iii) 10 groups from 5 keV to 100 keV. Our FLASH simulations model 6 species (Deuterium, Tritium, Hydrogen, Carbon, Oxygen and Silicon). Each species has its own tabulated opacity table, generated from the Los Alamos TOPS Opacity database [10].

B. TICF: Transport for ICF

We have developed a simulation package TICF for the plasma transport properties (viscosity, temperature and concentration diffusion) for the ICF implosion process and especially in the late time and hot spot regime [11]. The plasma transport models in TICF are calibrated using quantum molecular dynamics (QMD) simulations. TICF uses the Hu [12, 13] model of thermal conduction and the Daligault [14–16] concentration diffusion model with screening. The concentration diffusion coefficients estimated to be accurate within a factor of two in comparison to QMD data.

C. FTI: Front Tracking API

The front tracking software has been packaged into an Application Programming Interface (API), FTI, and is adapted to the FLASH code for use in 2D [17]. In that study, we found that converged front tracking simulations in agreement with much more finely resolved untracked simulations, but considerable and even qualitative differences were observed between the tracked and untracked simulations at grid levels which were converged for tracking but under resolved for the untracked simulations. Here this trend is more pronounced, as the perturbations are stronger than [17], and the untracked and tracked simulations are not fully in agreement at the finest mesh presented. We identify the front tracked solution as correct through comparison to analytic solution at times for which the errors are already significant but early enough so that a simple analytical model can be used for verification. Through this comparison to an analytical solution, we identify the numerical concentration diffusion is equal to five times the physical concentration diffusion.

The front tracking algorithm couples a lower-dimensional surface, which is tracked, to a standard Eulerian solver. Front tracking eliminates numerical diffusion across the tracked front. It has been observed to converge on coarser grids than are required for untracked simulations. Detailed front tracking Rayliegh-Taylor simulation simulations with added physical concentration diffusion have been verified and validated [18–20], with comparison to experiments of Smeeton-Youngs [21].

III. SIMULATION RESULTS

The effect of the numerical and physical diffusion, variation of the divot amplitude and width and the mesh convergence on the divot dynamics are studied as they influence the hot spot properties. The effect of the divot could be amplified if it crosses the location within the cold shell where the flow becomes RT unstable due to stagnation (acceleration direction reversal). This does occur but too late in time for the divot to enter into the hot spot. This

TABLE I: Four way comparison of simulations with and without numerical concentration diffusion and with and without physical concentration diffusion. The minimum radii are defined as the location for the 4 keV boundary and the 0.5% carbon concentration. The diffusion cliff is defined as the location of the change of acceleration at bang time. Note the strong differences between the tracked and untracked simulations as well as between with and without concentration diffusion.

Physical Concentration Diffusion	Numerical Concentration Diffusion	4 keV Minimum Radius (μm)	0.5% Carbon Concentration Minimum Radius (μm)	Diffusion Cliff Location(μm)
Yes	FT-Yes	2.45	17.1	22.23
No	FT-Yes	0	17.1	20.52
Yes	FT-No	0	8.55	13.68
No	FT-No	0	5.13	11.97

RT unstable locus is referred to as a performance cliff due to the change in behavior for perturbations which reach it. We take our base simulation for the comparison analysis to be front tracking, physical concentration diffusion, with the divot amplitude of 16% and a mesh of 1.7 μm. We vary one or two of these parameters at a time, while holding the others fixed at the base case values. Front Tracking (FT) represented with a Yes means that the Front Tracking is removing numerical diffusion or otherwise No. Similarily with physical concentration diffusion (MD) with a Yes mean that TICF is being used otherwise No. Our main conclusions are as follows.

1. We present combined effects of numerical and physical concentration diffusion transport. The divot does not enter the hot spot other than for the unphysical case of no physical concentration diffusion and without front tracking. This statement is exact up to double precision floating point accuracy withing the simulations, but we note that the exact solution of the diffusion equation includes propagation of exponential small quantities of CH into the hot spot. There is a significant effect on the hot spot thermal properties which results from the CH moving towards the core of the capsule. The divot extends beyond an instability cliff for CH mixing.

   (a) Physical concentration diffusion plays a significant role on the divot dynamics and puts the divot beyond an instability cliff. There is a strong effect on the 4 keV temperature boundary. There is no entry of the divot into the hot spot (7 μm) aside from the unphysical case. See Fig. 1 and Table I.

   (b) The physical concentration diffusivity is varied by a factor of two in accordance with TICF uncertainty estimates described in []. The increase in the concentration diffusion coefficient does not cause CH to enter the hot spot. See Table II.

2. We vary the mesh resolution for both tracked and untracked simulations inclusive of physical concentration diffusion. Both tracked and untracked simulations appear convergent, but to significantly different apparent limits. We believe that the front tracked solution is correct by examining early time simulation data in comparison to an analytic. The nominal or apparent convergence of the untracked solution to an apparent (but appearantly incorrect) limit is an issue beyond the scope of this paper. In Fig. 3, left frame, we compare the tracked and untracked solutoins at t = xxx ns to to an analytical solution. In this comparison, the tracked solution is clearly the (nearly) correct one and the untracked solution is far from agreement. In Fig. 3, right frame, we compare the untracked solution to an analytical solution having 5 times larger diffusion coefficient, with approximate agreement. We conclude that the untracked solution has a numerical concentratoin diffusion about 5 times larger than the physical concentration diffusion. See Figs. 2, 3 and Table III.

3. We present effects from the variation of the divot amplitude and width.

   (a) We vary the divot amplitude from the base case with amplitudes of 5%, 10%, 16% and 25%. The larger amplitude perturbation has stronger thermodynamic effects on the hotspot properties. No ablator material enters the hot spot as the strength of the perturbation increases. See Fig. 4 and Table IV.

   (b) The divot width is varied by a factor of two in a simulation with FT-TICF. The wider divot results in a more strongly perturbed ion temperature boundary at the edge of the hotspot. See Fig. 5

IV. DISCUSSION

We find no support for the divots to enter into the hotspot. However, we do find a significant influence on the hotspot thermodynamics. The 4 keV ion temperature boundary is significantly decreased. Large perturbations amplify this

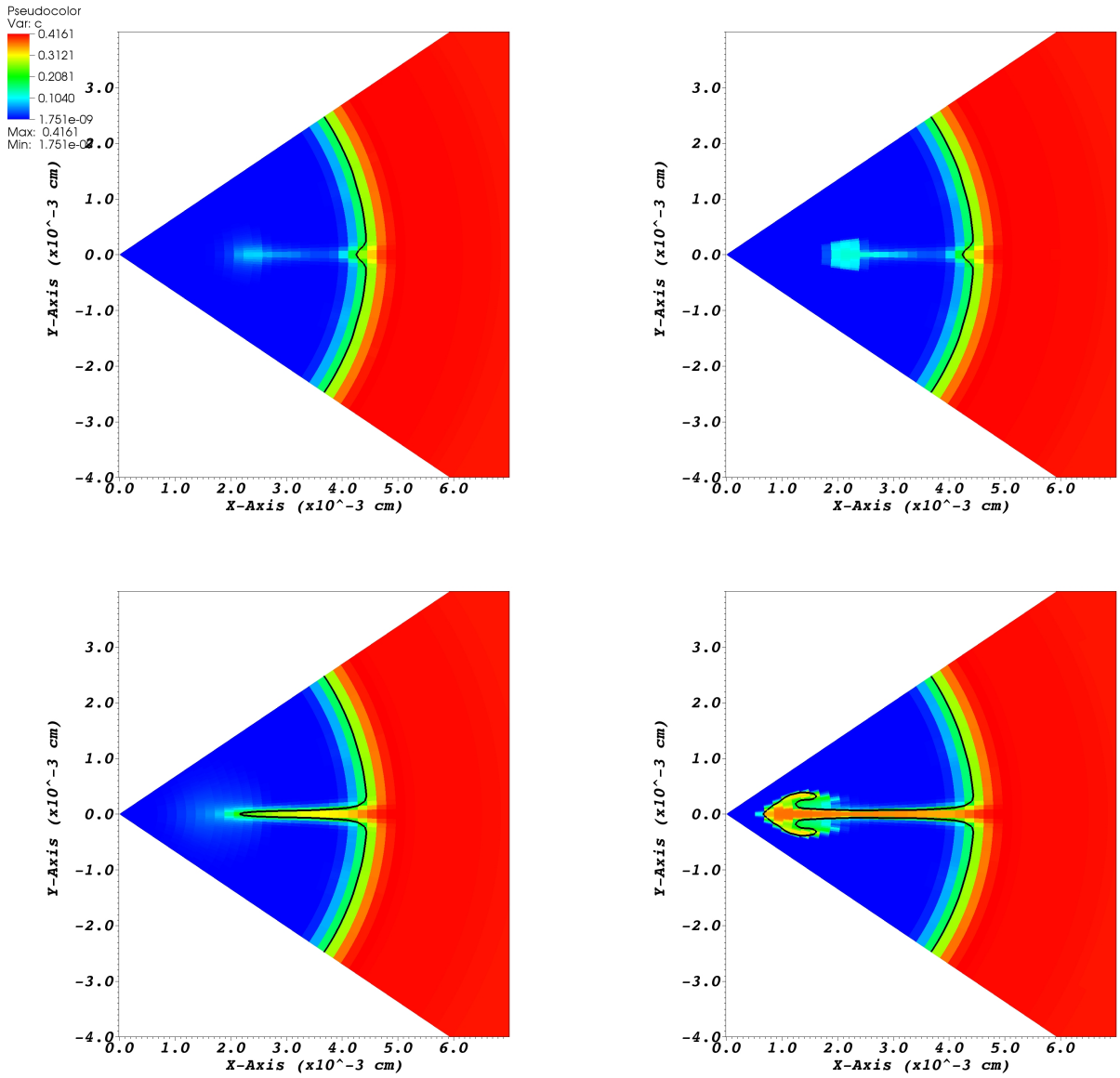

FIG. 1: Carbon color plots at bang time. Starting clockwise from the top left frame is Front Tracking + TICF + 16%, top right frame is Front Tracking + 16%, bottom right is untracked with no physical concentration diffusion with 16% and bottom left is Physical Concentration Diffusion + 16%. We conclude that Front tracking (reduction of numerical concentration diffusion) and the addition of physical concentration diffusion are both important variables.

TABLE II: Comparison of simulations with fixed diffusion coefficients increased by a factor of two. Other variables are as in Table I. Lines 1 and 2 should be compared to lines 1 and 3 of Table I to see the effect of the increase on the physical mass diffusion.

Physical Concentration Diffusion	Numerical Concentration Diffusion	4 keV Minimum Radius (μm)	0.5% Carbon Concentration Minimum Radius (μm)	Diffusion Cliff Location(μm)
Yes	FT-Yes	2.88	18.81	22.23
Yes	FT-No	0	8.55	13.68

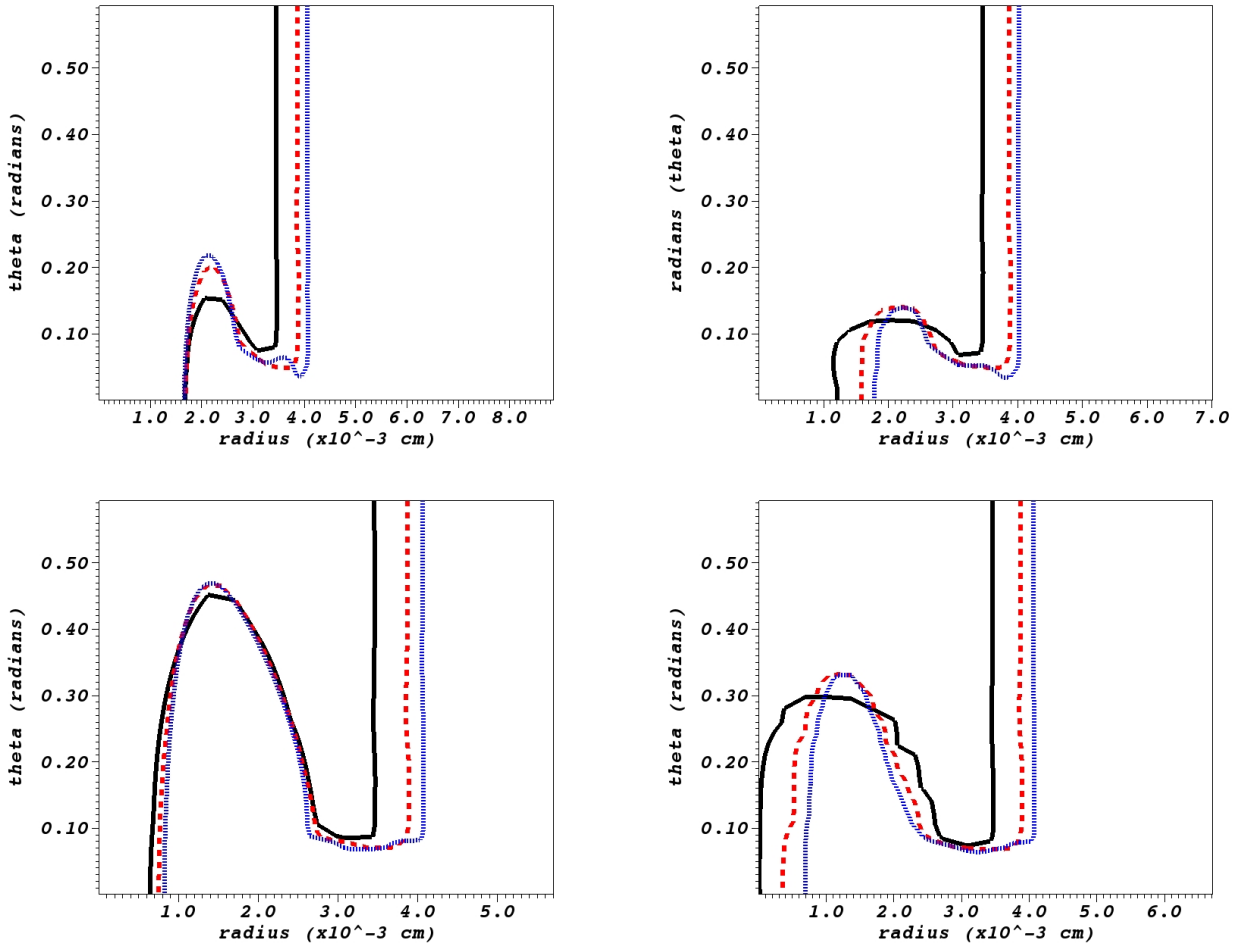

FIG. 2: Mesh refinement study of the 0.5% carbon contour at bang time for the tracked (top) and untracked (bottom) solutions with physical concentration diffusion (left) and none (right). The mesh in each figuree is 3.4 μm (solid black), 1.7 μm (dashed red) and 0.8 μm (dotted blue). The solutions appear to be converged nominally but for a top to bottom compartison of identical physics, the solution do not agree.

effect. We also find that the divot is sensitive to numerical mass diffusion (Front Tracking or not), even for solutions which appear to be converged nominally. Physical mass diffusion is an important variable and its inclusion is required for a correct solution.

Acknowledgments

This manuscript has been co-authored by Los Alamos National Laboratory, under Contract No. JL3K00 NYSB0000, Inertial Confinement Fusion Campaign. Los Alamos preprint XXXXXXXXXXX. This work was supported by the Army Research Office W911NF1310249. This research used computational resources of Stony Brook University.

[1] D. L. Lindl, R. L. McCrory, and E. M. Campbell, Physics Today **45**, 32 (1992).
[2] S. R. Nagel, S. W. Haan, J. R. Rygg, M. Barrios, L. R. Benedetti, D. K. Bradley, J. E. Field, B. A. Hammel, N. Izumi, O. S. Jones, S. F. Khan, T. Ma, A. E. Pak, R. Tommasini, and R. P. J. Town, Physics of Plasmas **22** (2015).

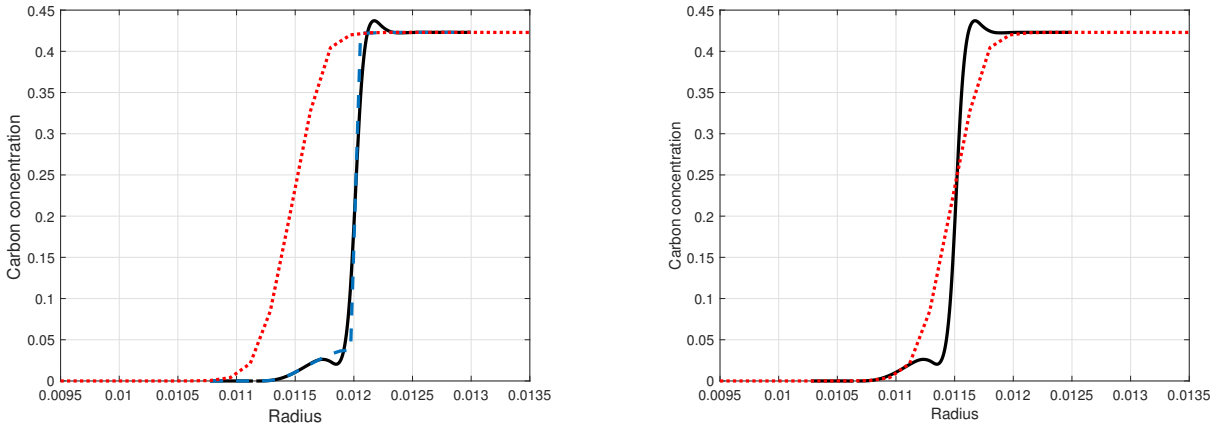

FIG. 3: Left: The analytical solution (solid black) being compared to FT-TICF (dashed blue) and TICF simulation (dotted red) at an earlier time of the deceleration phase. Right: Untracked solution (dotted red) compared to an analytic solution (solid black) with a diffusion constant 5%× the tracked with physical concentration diffusion.

TABLE III: Mesh convergence study with and without front tracking using a divot amplitude of 16% and physical mass diffusion along is fixed. Note the apparent convergence but to distinct solutions for a common problem for the two algorithms compared.

Numerical and Physical Concentration Diffusion	Mesh Level (μm)	4keV Minimum Radius (μm)	0.5%Carbon Concentration Minimum Radius (μm)	Diffusion Cliff Location (μm)
FT-Yes,MD-Yes	3.4	0	17.1	20.52
FT-Yes,MD-Yes	1.7	2.45	17.1	22.23
FT-Yes,MD-Yes	0.85	3.04	16.25	21.38
FT-No,MD-Yes	3.4	0	6.84	13.68
FT-No,MD-Yes	1.7	0	8.55	13.68
FT-No,MD-Yes	0.85	0	8.55	14.54
FT-No,MD-No	3.4	0	3.42	13.68
FT-No,MD-No	1.7	0	5.13	11.97
FT-No,MD-No	0.85	0	7.7	12.83

[3] D. Clark, "Direct simulation of a high convergence cryogenic implosion experiment on the national ignition facility," Tech. Rep. preprint (Lawrence Livermore National Laboratory, Livermore, CA, 2014).

[4] S. W. Haan et al., Phys. of Plasmas **18**, 051001 (2011).

[5] D. S. Clark, C. R. Weber, J. L. Milovich, J. D. Salmonson, A. L. Kritcher, S. W. Haan, B. A. Hammel, D. E. Hinkel, O. A. Hurricane, O. S. Jones, M. M. Marinak, P. K. Patel, H. F. Robey, S. M. Sepke, and M. J. Edwards, Physics of Plasmas **23** (2016).

[6] G. A. Kyrala, S. Dixit, S. Glenzer, D. Kalantar, D. Bradley, N. Izumi, N. Meezan, O. L. Landen, D. Callahan, S. V. Weber, J. P. Holder, S. Glenn, M. J. Edwards, P. Bell, J. Kimbrough, J. Koch, R. Prasad, L. Suter, J. L. Kline, and J. Kilkenny, Review of Scientific Instruments **81** (2010).

[7] B. Fryxell, K. Olson, P. Ricker, F. X. Timmes, M. Zingale, D. Q. Lamb, P. MacNeice, R. Rosner, J. W. Truran, and H. Tufo, Astrophysical Journal ,Supplement **131**, 273 (2000).

[8] J. Glimm, M. J. Graham, J. W. Grove, X.-L. Li, T. M. Smith, D. Tan, F. Tangerman, and Q. Zhang, Comput. Math. Appl. **35**, 1 (1998).

[9] B. A. Hammel, R. Tommasini, D. S. Clark, J. Field, M. Stadermann, and C. Weber, Journal of Physics: Conference Series **717**, 012021 (2016).

[10] N. H. Magee, J. Abdallah, Jr., R. E. H. Clark, J. S. Cohen, L. A. Collins, G. Csanak, C. J. Fontes, A. Gauger, J. J. Keady, D. P. Kilcrease, and A. L. Merts, in *Astrophysical Applications of Powerful New Databases*, Astronomical Society of the Pacific Conference Series, Vol. 78, edited by S. J. Adelman and W. L. Wiese (1995) p. 51.

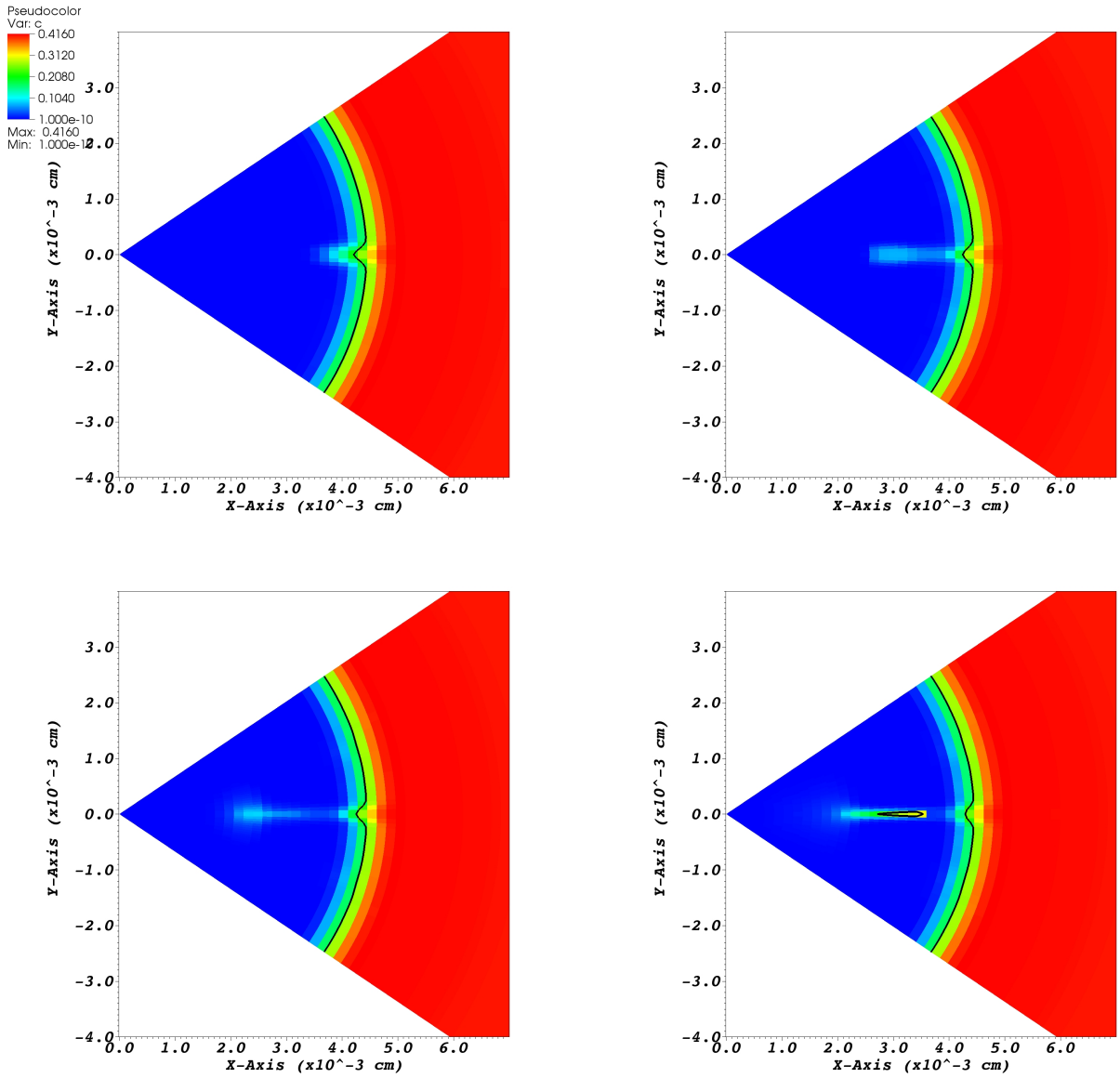

FIG. 4: Starting at top right and proeeding clockwise, the amplitudes are 5%, 10%, 16%, 25%.

[11] V. Rana, H. Lim, J. Melvin, B. Cheng, and D. H. Sharp, Phys. Rev. E (2016), lANL preprint LA-UR-12-21555; submitted.
[12] S. X. Hu, L. A. Collins, T. R. Boehly, J. D. Kress, V. N. Goncharov, and S. Skupsky, Phys. Rev. E **89**, 043105 (2014).
[13] S. X. H. .), L. A. Collins, V. N. Goncharov, J. D. Kress, R. L. McCrory, and S. Skupsky, Physics of Plasmas (2016).
[14] J. Daligault, Phys. Rev. E , 047401 (2012).
[15] J. Daligault, Phys. Rev. Lett. , 225004 (2012).
[16] J. Daligault, Phys. Rev. E **86**, 047401 (2012).
[17] J. Melvin, *Numerical Modeling of Hydrodynamic Instabilities and their Impact on Mix in Inertial Confinement Fusion*, Ph.d. thesis, Stony Brook University (2016).
[18] D. H. Sharp, Physica D **12**, 3 (1984).
[19] E. George and J. Glimm, Phys. Fluids **17**, 1 (2005), Stony Brook University Preprint SUNYSB-AMS-04-05.
[20] J. Glimm, D. H. Sharp, T. Kaman, and H. Lim, Phil. Trans. R. Soc. A **371**, 20120183 (2013), Los Alamos National Laboratory Preprint LA-UR 11-00423 and Stony Brook University Preprint SUNYSB-AMS-11-01.
[21] G. Dimonte, D. L. Youngs, A. Dimits, S. Weber, M. Marinak, S. Wunsch, C. Garsi, A. Robinson, M. Andrews,

TABLE IV: Comparison of effect of divot amplitude for FTI-TICF simulations of the RT deceleration phase.

Amplitude (%)	4 keV Minimum Radius (μm)	0.5% Carbon Concentration Minimum Radius (μm)	Diffusion Cliff Location (μm)
0	7.19	41.05	31.14
5	2.52	34.2	27.36
10	2.57	25.65	27.36
16	2.45	17.1	22.23
25	0	10.26	11.97

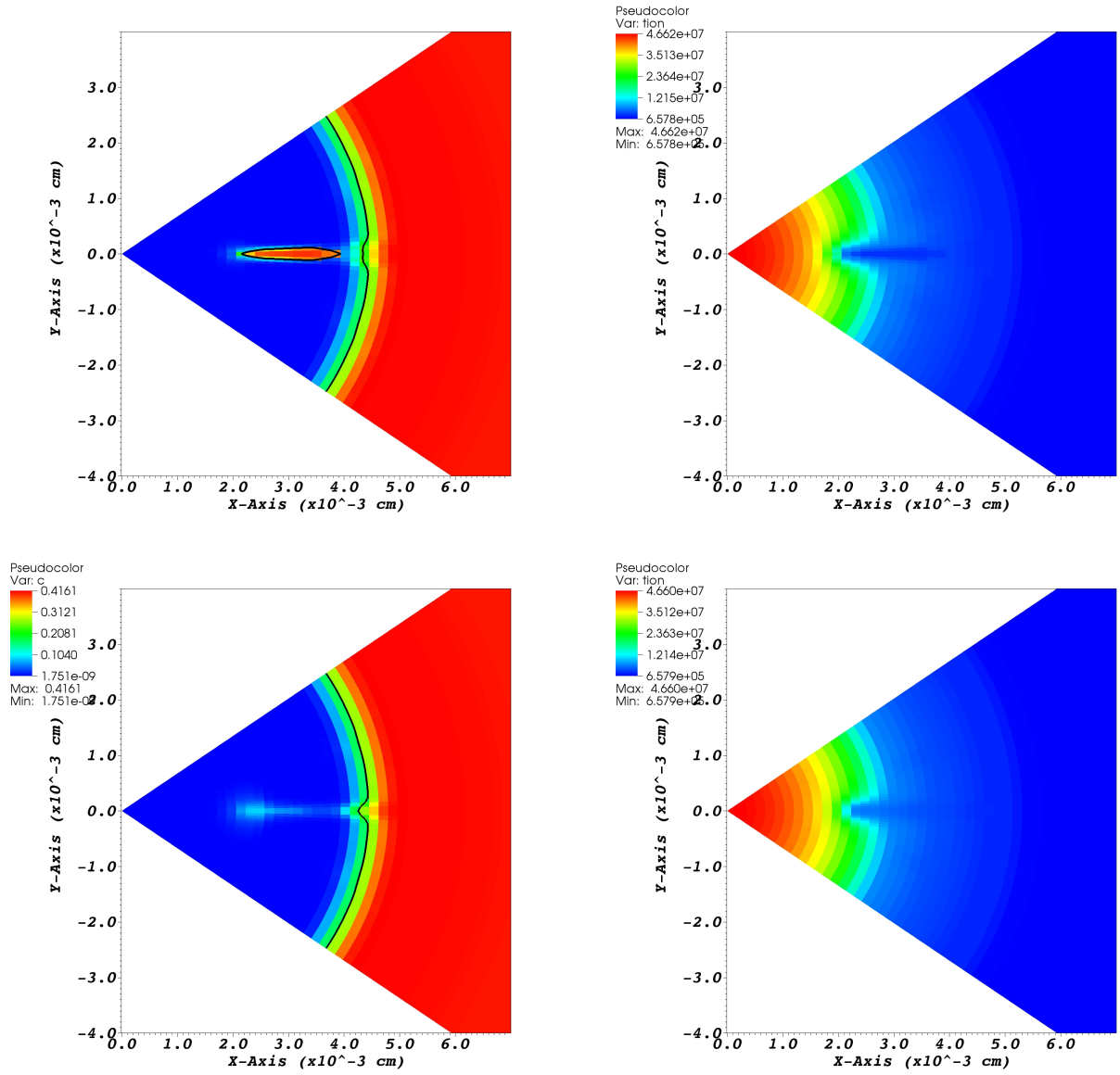

FIG. 5: The wide divot (top row) is compared to the narrow (base case) divot (bottom row). The left frames present the carbon density levels with a 50% carbon contour (black line) shown. Temperatures are shown on the right.

P. Ramaprabhu, A. C. Calder, B. Fryxell, J. Bielle, L. Dursi, P. MacNiece, K. Olson, P. Ricker, R. Rosner, F. Timmes, H. Tubo, Y.-N. Young, and M. Zingale, Phys. Fluids **16**, 1668 (2004).